SYNTHESIS AND MAGNETIC PROPERTIES OF LARGE-AREA FERROMAGNETIC NANOSTRUCTURE ARRAYS

WANG ZONGBIN

NATIONAL UNIVERSITY OF SINGAPORE

2014

SYNTHESIS AND MAGNETIC PROPERTIES OF LARGE-AREA FERROMAGNETIC NANOSTRUCTURE ARRAYS

WANG ZONGBIN

(M. Eng. MIT, 2009)

(B. Eng. NTU, 2007)

A THESIS SUBMITTED

FOR THE DEGREE OF DOCTOR OF PHILIOSOPHY

IN ADVANCED MATERIALS FOR MICRO- AND NANO- SYSTEMS (AMM&NS)

SINGAPORE-MIT ALLIANCE

NATIONAL UNIVERSITY OF SINGAPORE

2014

Declaration

I hereby declare that this thesis is my original work and it has been written by me in its entirety. I have duly acknowledged all the sources of information which have been used in the thesis.

This thesis has also not been submitted for any degree in any university previously.

_____

Wang Zongbin

23/01/2014

Acknowledgements

This project would not have been feasible without the guidance, support and constant encouragement of many individuals. Firstly, I would like to express my deepest gratitude to my thesis supervisors, Professor Choi Wee Kiong, Professor Carl V. Thompson and Associate Professor Liu Xiaogang for their dedicated guidance. I would like to thank Professor Caroline Ross and Prof. Adekunle Adeyeye for their invaluable advices and help.

Most of my research work was conducted in the NUS ECE Microelectronics Laboratory, CICFAR and Institute of Materials Research and Engineering. I would like to extend my greatest gratitude to Mr. Walter Lim, Mr. Koo Chee Keong, Mr. Tang Xiaosong, Mr. Wang Weide and Ms. Teo Siew Lang for all the kindest assistance during the course of my research. Help from Dr. Liu Xin Ming and Shimon is deeply appreciated.

During my stay in SMA, I had many insightful discussions with my fellow schoolmates and lab mates. I would like to thank them all for their great support. Dr. Yun Jia guided me at the start of my research in Microelectronics Lab, his help is greatly appreciated.

Lastly, I would like to dedicate my gratitude to my wife Xiaofang, my son Yunhao and my parents who have been supporting me throughout my studies.

Table of Contents

Summary

This thesis presents the author's research on the synthesis and magnetic properties of ordered array of various ferromagnetic nanostructures. A large-area high-throughput synthesis technique was developed using maskless interference lithography as the patterning method. The technique proved to be highly versatile on the final geometries achievable. The structures demonstrated include ferromagnetic nanodisk, nanoparticle, cylindrical nanoshell, perforated nanocup, imperforated nanocup and concentrically layered NiFe/Au/NiFe nanoshell. The dimension of these structure was well controlled with sub-10 nm shell width demonstrated, which was difficult for conventional planar patterning methods. The period achieved was 250nm.

Magnetic properties of these novel ferromagnetic nanostructures were investigated experimentally with Vibrating Sample Magnetometry and Maneto-optical Kerr Effect measurements. Numerical micromagnetic simulations with the Object Oriented MicroMagnetic Framework (OOMMF) codes were performed to correlated with and explain the measured results.

Dipolar magnetostatic coupling can be significant to influence the overall switching process in an array with a short period. This was especially true in nanostructure arrays with larger in-plane stray field, like in nanodisk array.

The magnetization reversal processes of these nanomagnets were determined by their shapes and dimensions. The spin configuration of domain walls was also strongly affected. The switching paths of NiFe nanoshells were

strong dependent on their shell widths. With larger shell width, the nanoshell exhibited Onion-Vortex-Reverse Onion switching path similar to that observed typically for thin film nanorings despite its higher aspect ratio. With a thin shell width of 8nm, we observed an absence of Vortex state during the switching, both in experiment and simulation. Presence of partially and fully covered base in perforated and imperforated nanocup, respectively, gave the two nanostructure different switching paths.

In concentric layered NiFe/Au/NiFe nanoshells, interlayer magnetic couplings through the Au spacer were critical to determine the overall magnetization reversal process. Different magnetic coupling mechanisms were surveyed with micromagnetic simulations.

List of Figures

Chapter 1 Introduction

1.1 Background

There has been tremendous research interest devoted to nanostructures due to their novel properties compared to bulk material. Various top-down and bottom-up synthesis methods have been developed for a variety of fascinating nanostructures in the past decades. Understanding of material and structure properties at nanoscale has greatly advanced. Among them are a range of ferromagnetic nanostructures including nanodisk, nanoring, nanotube and layered heterostructures. Interesting magnetic properties emerge in these structures due to the geometry confinement on the magnetization. These structures are of great importance both for the fundamental study of magnetism and for their potential in various emerging applications such as bit patterned media memory, spin wave logic devices and sensors [1-4].

Ferromagnetic ring structures have attracted a lot of research interest in the past two decades. They usually go through a two-step Onion-Vortex-Reverse Onion magnetization reversal process [5]. At Onion and Reverse Onion state, the magnetization form two domains separated by head-to-head and tail-to-tail domain walls. At Vortex state, the magnetization forms a flux closure state with minimized stray field. Nanotubes, with longer aspect ratio,

have more complex magnetization configurations and reversal processes, with different domains formed along the tube axis under low external field [6, 7].

Magnetic heterostructures are important class of ferromagnetic nanostructures with interesting magnetic properties due to coupling of magnetization between the ferromagnetic layers. Layered thin films, superlattices and stacked nanostructures of magnetic materials have been widely explored. Magnetic coupling plays important role in determining the magnetization states and moment reversal process of these structures [8-10].

1.2 Motivation

Despite great advances in feature size and versatility, conventional synthesis methods for ferromagnetic nanostructure array have limitations either on the minimum feature size, the cost effectiveness, the uniformity in feature size and geometry, or on the long range order in the arrays. A large-area high-throughput synthesis method with good control over feature size and uniformity is in demand.

A wide variety of ferromagnetic nanostructures have been studied in literatures. Ferromagnetic nanorings and nanotubes have been attracting the research interest and studied extensively. They represent cylindrical geometry with either ultra-low or ultra-high height/diameter ratio. Nanoshells, the intermediate geometries between nanorings and nanotubes with height/diameter ratio in between, have not been investigated in detail in the past. Moreover, nanoshells have two interesting variation geometries. Nanocups can be perceived as nanoshells with a disk base. Perforated

nanocups can be perceived as nanoshells with thin film ring-shaped base. The geometry confinement in these nanostructures can lead to interesting magnetization states and reversal processes. However, synthesis and magnetic properties of these two nanostructure arrays have not been reported in literature.

There have been extensive studies on interlayer magnetic coupling in magnetic hetero structures such as pseudo-spin-valve nanorings. These studies focused on vertically stacked ring structures [11-19]. Laterally layered structures such as concentric layered nanoshells of ferromagnetic materials separated by a non-magnetic spacer, especially those with submicron dimension, have not been well studied [20].

1.3 Organization of chapters

Chapter 2 reviews the previous research in the field of patterned ferromagnetic nanostructures. The conventional synthesis methods are reviewed. Also, the theory of static micromagnetics related to the understanding of magnetism in ferromagnetic nanostructures is introduced. Different interlayer magnetic coupling mechanisms through a non-magnetic spacer layer are discussed.

Chapter 3 begins with a discussion on the experimental procedures for large-are ordered nanostructure array in the scope of this thesis, including interference lithography, pattern transfer and angular deposition techniques. Structural and magnetic property characterization techniques followed by micromagnetic simulation methods are introduced. Lastly, the synthesis

procedures and morphology characterization results for each nanostructure in this thesis are presented.

In Chapter 4, magnetization switching of NiFe nanodisk array is presented. These nanodisks exhibit single domain or vortex switching path depending on their dimension. The effect of dipolar magnetostatic coupling in the array is examined theoretically. Dewetting of NiFe nanodisks lead to array of NiFe nanoparticle arrays. The nanoparticle morphology is discussed correlated to solid state chemical and physical processes in the high temperature dewetting.

Chapter 5 discusses large-area synthesis of NiFe cylindrical nanoshell, perforated nanocup and nanocup arrays. The effects of shell width on the magnetization reversal processes of nanoshells and their spin configuration are examined by experiments and simulations. Following that, perforated nanocup with circular ring base and nanocup with fully covered base are examined in comparison with nanoshells.

In Chapter 6, magnetization reversal processes of concentric layered cylindrical NiFe/Au/NiFe nanoshell arrays with different layer thickness combinations are presented. The two NiFe layers can be exchange-decoupled by an Au spacer layer with sufficient thickness. The overall switching behavior of layered nanoshell is determined by various magnetic coupling mechanisms. Various coupling mechanisms are discussed through micromagnetic simulations.

Chapter 7 reviews and concludes the accomplishments of the work presented in this thesis and provides recommendations for future work.

1.4 References

1. Ross, C. A., *Patterned Magnetic Recording Media.* Ann. Rev. Mater. Res., 2001. **31**(1): p. 203.
2. Zutic, I. and Fuhrer, M., *Spintronics: A path to spin logic.* Nat. Phys., 2005. **1**(2): p. 85.
3. Liao, M. Y., et al., *Synthesis of magnetic hollow nanotubes based on the kirkendall effect for MR contrast agent and colorimetric hydrogen peroxide sensor.* J. Mater. Chem., 2011. **21**(22): p. 7974.
4. Zhu, J. G., Zheng, Y., and Prinz, G. A., *Ultrahigh density vertical magnetoresistive random access memory (invited).* J. Appl. Phys., 2000. **87**(9): p. 6668.
5. Vaz, C. A. F., et al., *Ferromagnetic nanorings.* J. Phys.: Condens. Matter, 2007. **19**(25): p. 255207.
6. Chang, C. R., Lee, C. M., and Yang, J. S., *Magnetization curling reversal for an infinite hollow cylinder.* Phys. Rev. B, 1994. **50**(9): p. 6461.
7. Li, D. D., et al., *Template-based Synthesis and Magnetic Properties of Cobalt Nanotube Arrays.* Adv. Mater., 2008. **20**(23): p. 4575.
8. Biragnet, F., et al., *Interactions between Domain Walls in Coupled Films.* Physica Status Solidi (B), 1966. **16**(2): p. 569.
9. Bruno, P., *Interlayer exchange coupling: a unified physical picture.* Journal of Magnetism and Magnetic Materials, 1993. **121**: p. 248.

10. Bruno, P. and Chappert, C., *Oscillatory coupling between ferromagnetic layers separated by a nonmagnetic metal spacer.* Phys. Rev. Lett., 1991. **67**(12): p. 1602.

11. Ross, C. A., et al., *Magnetism in multilayer thin film rings.* J. Phys. D-Appl. Phys., 2008. **41**(11): p. 6.

12. Castaño, F. J., Morecroft, D., and Ross, C. A., *Low-field giant magnetoresistance in layered magnetic rings.* Phys. Rev. B, 2006. **74**(22): p. 9.

13. Huang, L., Schofield, M. A., and Zhu, Y., *Direct observation of the controlled magnetization reversal processes in Py/Al/Py asymmetric ring stacks.* Appl. Phys. Lett., 2009. **95**(4): p. 3.

14. Liu, X. M., Jain, S., and Adeyeye, A. O., *Magnetic Properties of Perpendicularly Magnetized [Co/Pd]/Au/[Co/Pd] Pseudo-Spin-Valve Nano-Ring Structures.* IEEE Trans. Magn., 2011. **47**: p. 2628.

15. Castaño, F. J., et al., *Spin-Dependent Scattering in Multilayered Magnetic Rings.* Phys. Rev. Lett., 2005. **95**(13): p. 137201.

16. Hayward, T. J., et al., *Switching behavior of individual pseudo-spin-valve ring structures.* Phys. Rev. B, 2006. **74**(13): p. 134405.

17. Mascaro, M. D., et al., *360 °domain wall mediated reversal in rhombic Co/Cu/NiFe magnetic rings.* Appl. Phys. Lett., 2011. **98**(25): p. 252506.

18. Lee, J. H., et al., *Influence of thermal excitation on magnetization states and switching routes of magnetic multilayer rings.* J. Appl. Phys., 2009. **105**(7): p. 3.

19. Jain, S. and Adeyeye, A. O., *Low temperature investigations of switching processes in multilayer rings.* J. Appl. Phys., 2009. **106**(2): p. 4.

20. Jain, S. and Adeyeye, A. O., *Aligned Alternating Head-to-Head and Tail-to-Tail Domain Walls in Ferromagnetic Concentric Rings.* IEEE Trans. Magn., 2010. **46**(6): p. 1595.

Chapter 2 Literature Review

2.1 Introduction

In the past few decades, ferromagnetic nanostructures have attracted extensive research interest for fundamental studies of magnetism in confined geometries and a variety of emerging applications such as data storage, spin logic devices and magnetic sensors. The structures of interest explored in literatures include disks, particles, rings, tubes, and layered hetero structures. There have been great advances in the synthesis method and understanding of magnetism from these structures.

In this chapter, we firstly review the conventional synthesis techniques for ferromagnetic nanostructure arrays, especially for nanoring and nanotube arrays. The advantages and drawbacks of each patterning technique are analyzed. Following that, we present the theoretical background in micromagnetics relevant to the understanding of magnetization reversal processes of ferromagnetic nanostructures. Subsequently, magnetization reversal processes of ferromagnetic nanodisks, nanorings and nanotubes reported in literature are presented. Lastly, various magnetic coupling mechanisms between two ferromagnetic layers separated by a non-magnetic spacer layer in thin films and multilayer patterned structures are discussed.

2.2 Conventional synthesis methods for nanoring/nanotube arrays

Previous ferromagnetic nanoring and nanotube array fabrication reported has focused on planar patterning techniques including optical lithography, electron beam lithography [1], nanosphere lithography [2-4], anodic alumina templating [5] and block copolymer templating [6, 7]. Nanotube arrays are most commonly fabricated with electrochemical deposition, atomic layer deposition or shadowed evaporation over an anodized alumina template [8-11] or by ion milling of conformal ferromagnetic thin film deposited on resist pillars patterned by electron beam lithography [12].

2.1.1 Optical lithography

Optical lithography transfers the patterns from a mask to light sensitive photoresists. There are three exposure methods commonly used: contact printing, proximity printing and projection printing, as shown in Figure 2.1.

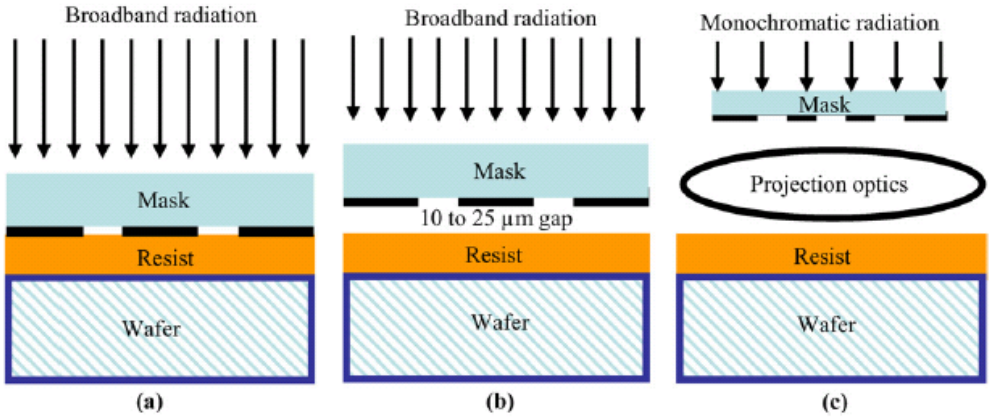

Figure 2.1 Schematic diagrams of photolithography exposure modes: contact (a), proximity (b) and projection printing (c) [13].

Projection printing has advanced tremendously in terms of resolution driven by demand for miniaturization in microelectronics industry.

Nonetheless, the equipment bears a high cost. In addition, each exposure only patterns a limited area because of shrinkage during projection. A “step and flash” method has to be employed to repeat the patterning process.

Contact printing and proximity printing methods requires lower equipment cost. However, the resolution is limited by feature size on the mask and diffraction effect during exposure. For the ring geometry, the exposure of inner circle further limits the scaling down of overall feature due to diffraction. Certain techniques can help to improve the resolution, such as implementation of extreme UV light source and phase shift masks. Nonetheless, the size of the ring, particularly the ring width, is quite limited [14]. Dry etching of ferromagnetic metal thin films is difficult. Nanorings are typically patterned by lift-off process. Figure 2.2 shows one example of nanoring array patterned by photolithography and lift-off process [15].

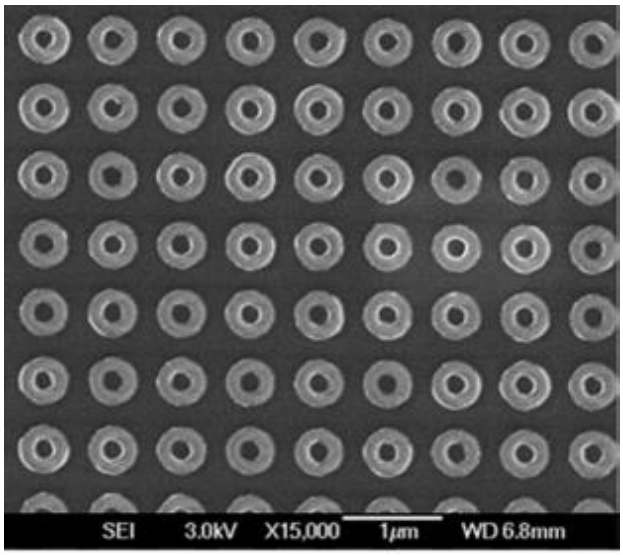

Figure 2.2 SEM image of NiFe nanoring Array patterned by photolithography [15].

2.1.2 Electron beam lithography

Electron beam lithography uses electron beam to write the pattern directly onto a resist sensitive to electron beam. It is a highly versatile patterning method to achieve various desired patterns. Sub-10nm feature can be achievable. Figure 2.3 shows an example of NiFe nanorings patterned using electron beam lithography and lift-off [1]. Flexible feature and size control were demonstrated by this method.

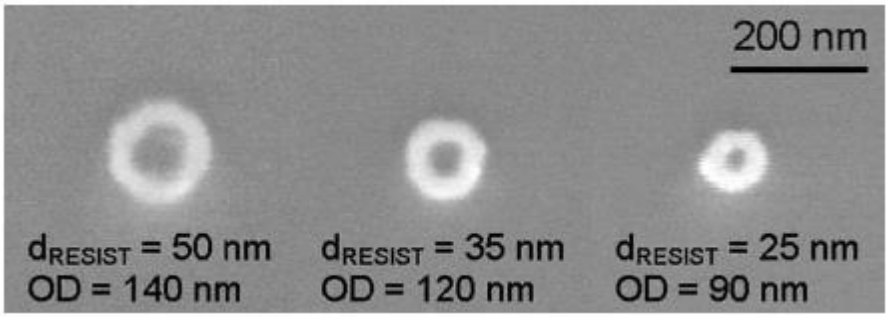

Figure 2.3 SEM image of 10nm-thick NiFe nanorings patterned by electron beam lithography (OD = outer diameter) [1].

Ferromagnetic nanotube array has also been demonstrated by using electron beam lithography as the patterning technique. Figure 2.4 depicts the synthesis method [12]. Array of resist pillars were patterned by electron beam lithography. A conformal NiFe thin film was then deposited on the resist pillars and substrate. Subsequently, an ion milling process removed the NiFe thin film on top of the resist pillars and on the substrate, leaving behind array of NiFe nanotubes wrapped on resist pillars.

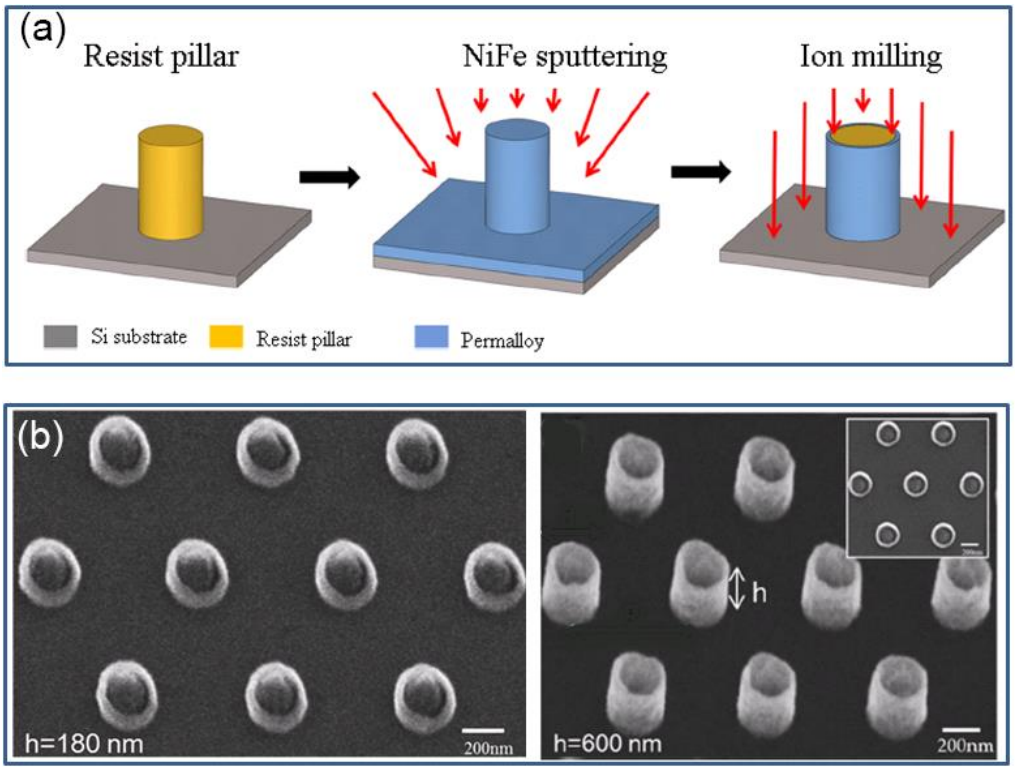

Figure 2.4 (a) Schematic of synthesis process and (b) SEM images of NiFe nanotube arrays patterned by electron beam lithography [12].

However, electron beam lithography suffers from high process cost due to its low throughput. As a serial patterning process in nature, electron beam lithography is a very slow process. It is not feasible for large-area patterning. In addition, it also suffers from proximity effect for high aspect ratio patterning.

2.1.3 Nanosphere lithography

Self-assembly of polymeric nanospheres can lead to an ordered monolayer array. Nanosphere lithography explores this ordered monolayer of nanospheres as material deposition or etch mask [16]. It is a parallel high-

throughput patterning technique. Figure 2.5 shows one example of nanorings fabricated by this method.

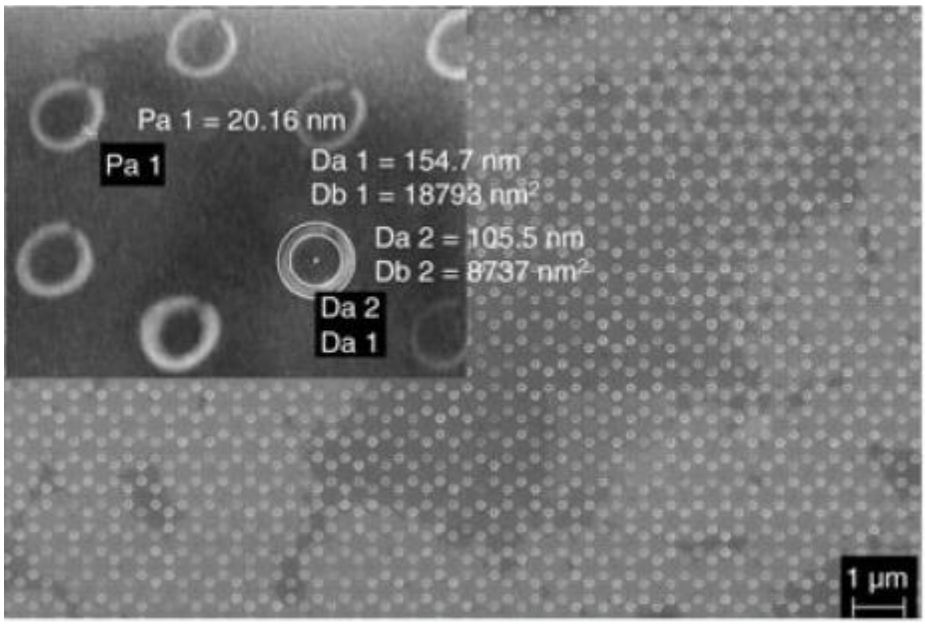

Figure 2.5 SEM image of Fe nanorings patterned by nanosphere lithography [4].

Nonetheless, there are a variety of defects present in the self-assembly process. These defects are ascribed to nanosphere polydispersity, point defect (vacancy), line defect (dislocation) and polycrystalline domain. As a result, long range order is usually deteriorated. This limits this patterning technique for patterning of large-area ordered arrays.

2.1.4 Anodic Aluminum Oxide (AAO) templating

Nanoporous anodic aluminum oxide forms array of ordered cylindrical pores when the process is controlled properly [17]. This AAO can act as a template in subsequent process to produce ordered array of nanostructures. Co

nanorings was demonstrated with electrodeposition of Co into the AAO template [5], as shown in Figure 2.6(a). Ferromagnetic nanotube arrays were fabricated by electrochemical deposition, atomic layer deposition or shadowed evaporation over an anodized alumina template [9-11].

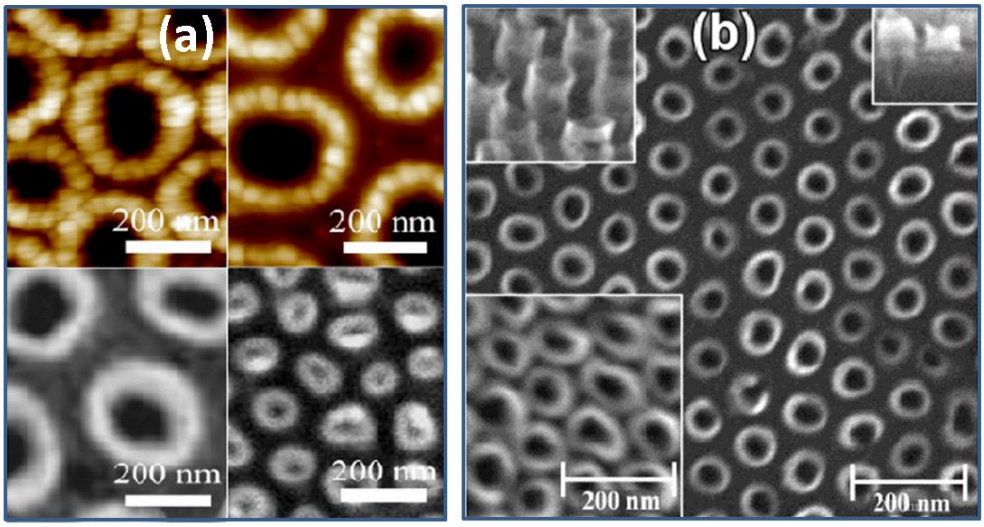

Figure 2.6 (a) Co nanoring and (b) Ni nanotubes patterned by AAO template [5].

Although this synthesis technique can demonstrate parallel patterning of nanorings and nanotubes with sub-100nm outer diameter, the array is not well ordered. The ordering of nanopores in AAO can be improved by imposing a topographical template [18]. However, it still has limitation on control of feature size and geometry uniformity.

2.1.5 Block copolymer lithography

Block copolymer can self assembles into bi-domain nanostructure during phase separation [19]. One of the phases can be selectively removed by an etching method. The remaining phase can serve as a mask for further patterning process. This method has been proved to be capable of synthesizing patterns with ultra-high density and sub-10nm features. Co nanorings with

outer diameter around 10nm has been demonstrated by ion-milling of Co deposited into array of nanopores patterned by block copolymer lithography technique, as shown in Figure 2.7 [6].

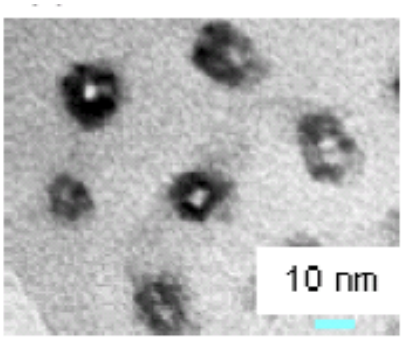

Figure 2.7 Co nanorings patterned by block copolymer lithography [6].

In spite of its success on achieving ultra-high density and sub-10nm feature size, block copolymer lithography has intrinsic limitation on long range order. As a self-assembly process method in nature, the long range order is not preserved similar to other self-assembly patterning techniques like nanosphere lithography and AAO templating.

In summary, conventional synthesis methods have been successfully employed to demonstrate ferromagnetic nanoring and nanotube arrays. However, these methods impose limitations either on the dimension, cost effectiveness or on the long-range order of arrays. With optical lithography, the feature size is quite limited unless using expensive projection printing lithography setup. Electron beam lithography, a serial process in nature, is extremely time-consuming for large area patterning. Self-assembly processes like block copolymer lithography, nanosphere lithography, anodized alumina

templating have the limitation on long range order. For potential application of nanomagnets like bit patterned media, precise patterning of features in well-ordered array is required.

2.3 Static micromagnetics

Static micromagnetics seeks to solve the spatial distribution of magnetization in the ferromagnetic structure at equilibrium state. The magnetization reversal process and moment configurations of any ferromagnetic structure are determined fundamentally by competition between the energy terms related to its material, structure, size and applied field. These energy terms include Zeeman energy, exchange energy, demagnetization energy, magnetocrystalline anisotropy energy and magnetoelastic anisotropy energy [20]. In a polycrystalline nanomagnet, effect of magnetocrystalline anisotropy energy is weak when compared to shape-induced anisotropy. Magnetoelastic anisotropy is also negligible when stress in the structure is small. This section only discusses Zeeman energy, exchange energy and demagnetization energy.

2.1.6 Zeeman energy

Zeeman energy arises from interaction between the external applied field and the moment of magnetic material. It is given by

$$E_{Zeeman} = -\mu_0 \int_V M \cdot H_{Ext} dV ,$$

where μ_0 is the permeability of free space, M is the localized magnetization vector and H_{ext} is the external applied field. Zeeman energy is minimized when the magnetization aligns in parallel with the applied field.

2.1.7 Exchange energy

Exchange energy is ascribed to exchange interaction of electron spins. The exchange interaction favors parallel or antiparallel alignment of moment. It is given by equation:

$$E_{Exchange} = A \int_V \left((\nabla m_x)^2 + \left(\nabla \mathrm{m_y}\right)^2 + (\nabla m_z)^2 \right) dV \,,$$

where A is the exchange constant, m_x, m_y, and m_z are component of magnetization. Exchange energy is minimized when the magnetization within the material is uniform.

2.1.8 Demagnetization energy

Demagnetization energy, also called self-magnetostatic energy, is the energy ascribed to dipole-dipole interactions of material within itself. It can be perceived as the energy associated to the interaction between the demagnetization field from a ferromagnetic structure and the magnetization itself. It is given by:

$$E_{Demag} = -\frac{\mu_0}{2} \int_V M \cdot H_d \, dV,$$

where μ_0 is the permeability of free space, M is the magnetization and H_d is the demagnetization field. The demagnetization field is evaluated by solving Maxwell equation with proper boundary conditions. Minimization of

demagnetization energy favors a magnetic moment configuration such that the magnetic charges and demagnetization field are minimized.

2.4 Ferromagnetic circular disks

Circular disks were among the first patterned ferromagnetic structures studied for their relatively simpler fabrication process. Cowburn *et al.* systematically investigated the effects of diameter and thickness on the switching path of supermalloy ($Ni_{80}Fe_{14}Mo_5$) circular nanodisks [21]. These circular nanodisks exhibit Vortex or single domain magnetization switching depending on the dimension. In the Vortex switching path as shown in Figure 2.8 a, a Vortex nucleated when the field was reduced to near zero. The Vortex core then migrated towards the edge of the disk and annihilated there under the reverse field. In the Single-Domain switching path as shown in Figure 2.8 b, the magnetization reversed by a coherent rotation of moment without formation of a Vortex. Nanodisks with larger diameter and higher thickness experienced a Vortex state in the magnetization process, while disks with smaller diameter and lower thickness went through the Single-Domain switching path, as shown in Figure 2.8(c).

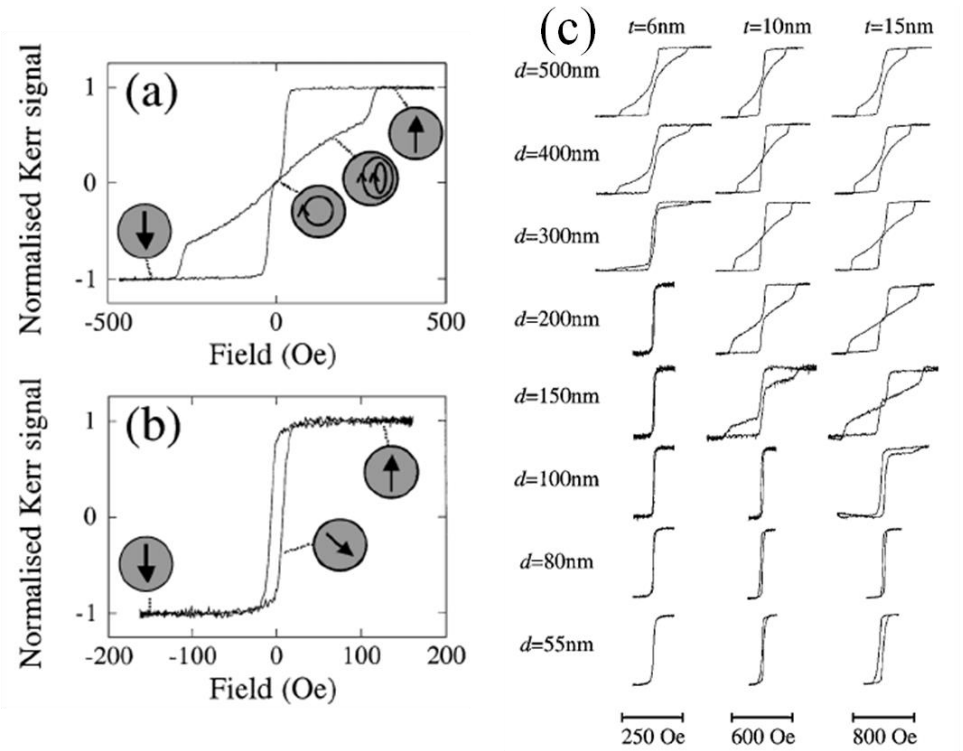

Figure 2.8 MOKE results showing Vortex (a) and Single-Domain (b) switching paths and for circular disks with various diameters and thicknesses (c) [21].

2.5 Ferromagnetic circular rings

The ferromagnetic rings studied in literature are generally thin-film rings in which the ring height or thickness is significantly smaller than ring width and diameter. These rings have in-plane magnetization anisotropy with two-step Onion-Vortex-Reverse Onion switching path in the magnetization reversal process, as shown in Figure 2.1 [22, 23].

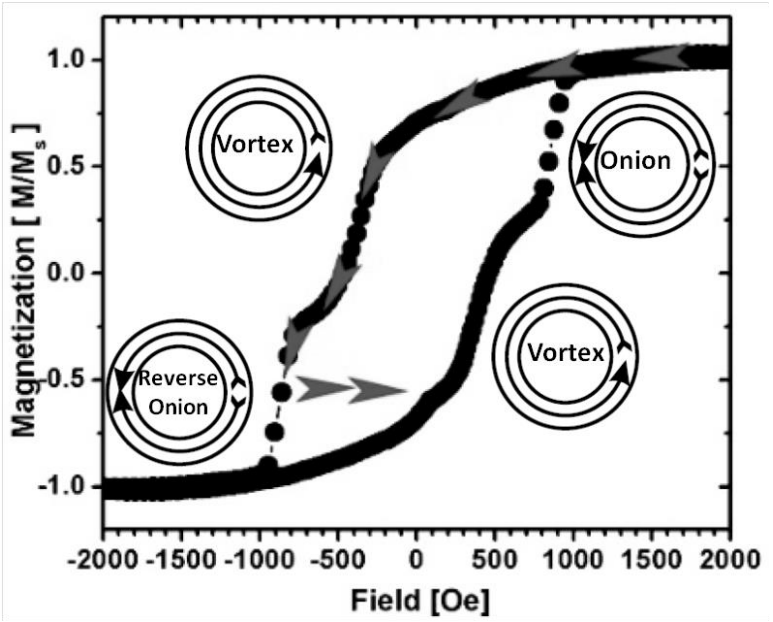

Figure 2.9 Hysteresis loop of Co ring array (outer diameter = 1200 nm, inner diameter = 900 nm, and thickness = 15 nm, polycrystalline Co) [22].

At Onion or Reverse Onion state, there are two domains separated by head-to-head and tail-to-tail domain walls formed at opposite ends of the diameter. At Vortex state, the magnetization forms a flux closure state. The Onion-Vortex transition happens as the two domain walls migrated to each other and annihilate. The Vortex-Reverse Onion transition happens by nucleation and growth of a reverse domain under the applied magnetic field [24].

The spin configuration of domain walls is important in determining the stray field around the nanomagnets. In rings with larger thickness and width, vortex domain wall is favored by minimization of magnetostatic energy. In rings with smaller thickness and width, transverse domain wall is preferred by minimization of exchange energy [25-27]. However, according to Laufenberg *et al.*, vortex domain wall is predominant in thin film rings with thickness

below 4nm. The structural defects in the ultra-thin film induce spatial modulation of magnetic properties and allow strongly twisted adjacent spins at reduced cost of energy [26].

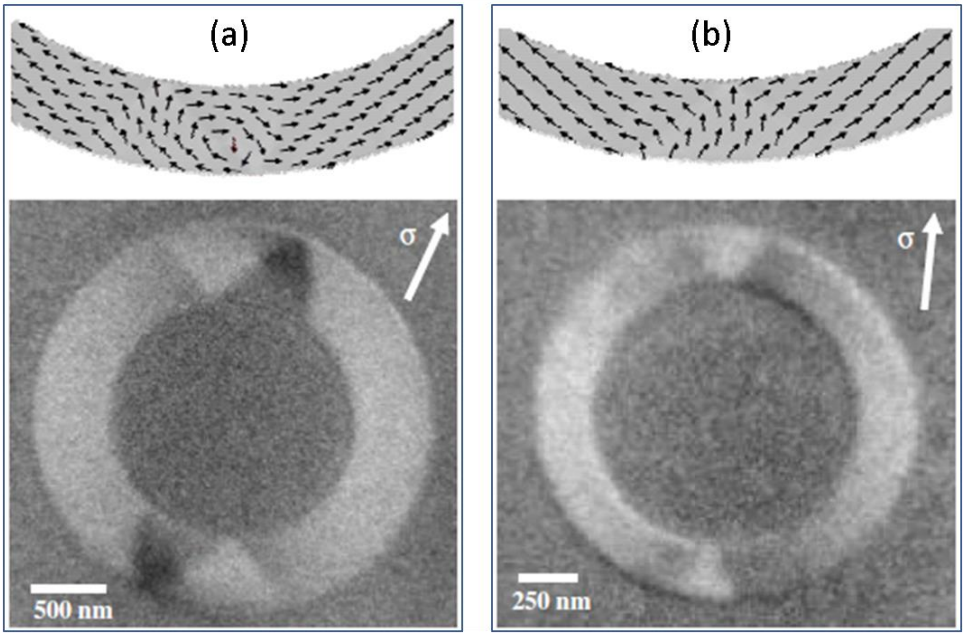

Figure 2.10 Schematic magnetization vector and photoemission electron microscopy images of vortex (a) and transverse (b) domain walls [25].

It is well known that in thin film rings the magnetic moments at domain wall rotate in plane with respect to the ring [27-29]. With transverse domain wall, the stray field has a higher in-plane component which could induce magnetostatic crosstalk between adjacent rings [30].

2.6 Magnetization reversal in ferromagnetic nanotubes

Nanotube can be regarded as a ring geometry which has a height much larger than its width. Long nanotubes with high aspect ratio tend to have easy axis along the tube, as shown in Figure 2.11 [11, 31, 32]. They exhibit

coherent or curling mode of magnetization switching path depending mainly on the diameter [31, 33]. In some studies, the long nanotubes exhibited diminished hysteresis both parallel and perpendicular to the tube axis. This was rather due to the nanotubes were closely spaced or even in contact with each other; hence the magnetizations were strongly coupled [34].

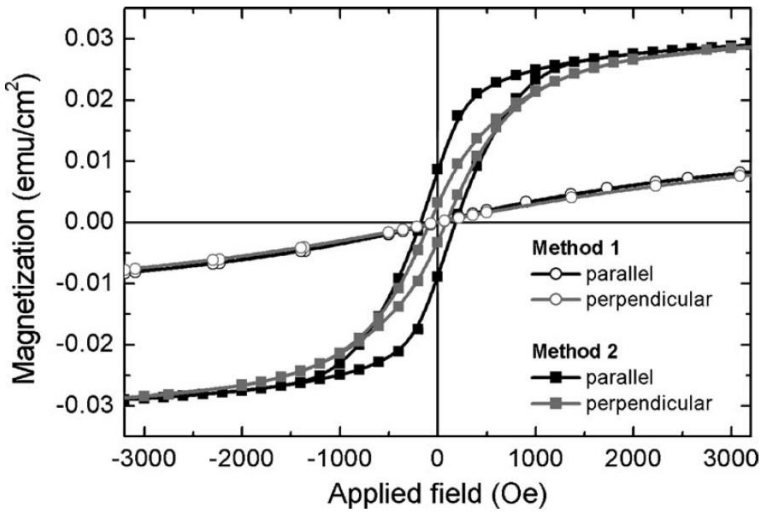

Figure 2.11 Hysteresis loops of Ni nanotube array (parallel and perpendicular relative to nanotube axis, length = 10 μm, diameter = 160nm, parallel and perpendicular relative to nanotube axis) [11].

For shorter nanotubes, the hysteresis perpendicular to tube axis increases. In a study of NiFe nanotubes reported with an outer diameter of 300nm, a width of 20nm and a height of 600nm, the hysteresis loop in-plane with substrate exhibits multi-step switching. Simulation shows the magnetic moments are incoherent along the tube axis. Magnetization divides into multi domains with vortex domain walls [12].

2.7 Magnetic coupling in layered thin films

Previous studies on layered thin films consisting of ferromagnetic layers separated by a non-magnetic spacer shows that the magnetizations can be coupled. Three of the common coupling mechanisms are indirect exchange coupling, direct pinhole coupling, Néel coupling and magnetostatic coupling due to stray field from domain walls.

2.1.9 Indirect exchange coupling

The interlayer indirect exchange coupling between ferromagnetic thin films through a non-magnetic spacer was studied extensively in the 1990s. The coupling was found to be oscillating periodically in sign and magnitude as a function of spacer thickness [35]. This coupling mechanism was only observed with very thin spacers under a few nanometers.

A variety of theoretical approaches were explored to explain this coupling behavior [36-42]. They shared the same underlying principle: a ferromagnetic layer in contact with the spacer induced a spin polarization to the conduction electrons in the spacer; this polarization interacted with the second ferromagnetic layer, thus giving rise to an effective exchange interaction between the ferromagnetic layers. The differences between these approaches were the methods to model the system and the approximations made in the modeling.

Among those attempts to theoretical explain the oscillating coupling behavior, one of the approaches was based on the Ruderman-Kittel-Kasuya-Yosida (RKKY) interaction. The RKKY interaction theory was proposed in

the 1950s to explain the oscillating coupling of magnetic impurities in a non-magnetic host material [43-45]. Bruno *et al.* adapted this theory and successful predicted the oscillation period for noble metal spacers [41, 42]. However, the coupling strength and phase cannot be modeled quantitatively.

2.1.10 Direct pinhole exchange coupling

As the spacer thickness decreases, significant amount of pinholes are present in the film as defects. At such defects site, the two ferromagnetic layers are in contact with each other. This forms a direct exchange coupling between the two layers [46]. The nature of such coupling is ferromagnetic. Historically, pinhole exchange coupling mechanism due to defects in the film used to be a frustrating problem for investigation of indirect interlayer exchange coupling mechanisms [47].

2.1.11 Domain wall stray field induced magnetostatic coupling

In thin films, magnetization forms domains to reduce demagnetization energy. Domains are separated by domain walls, where stray field arises. It was firstly proposed in the 1960s by Fuller and Biragnet *et al.* that the stray field at domain walls can lead to magnetostatic coupling between two ferromagnetic layers separated a nonmagnetic spacer layer [48, 49]. The coupling strength is affected by the type of domain wall, domain wall density, materials and spacer thickness.

Such magnetostatic coupling induced by domain walls were directly observed by Kuch *et al.* through photoelectron emission microscopy using x-ray magnetic circular dichroism as a magnetic contrast in a Co/Cu/Ni trilayer

stack [50]. With a 6nm Cu spacer, Lew *et al.* demonstrated trapping of the domain walls in the soft NiFe layer with the magnetostatic interaction by the stray fields from the domain-wall in the hard Co layer [51]. As a result, mirrored domain structures formed in the trilayer stack. It is also shown experimentally and theoretically that the in a $Co_{75}Pt_{12}Cr_{13}/Au_2O_3/Fe_{60}Ni_{40}$ layered thin film, the stray field at domain walls in the soft FeNi can be high enough to move the domain wall in the hard CoPtCr layer when the spacer is thin enough [52].

2.1.12 Néel coupling

Interfacial roughness is inevitable during sample preparation in layered ferromagnetic films or other structures. The roughness leads to the presence of magnetic poles at the interface due to the topographical waviness at boundary surfaces. It was proposed by Néel that these interfacial magnetic poles can lead to coupling between two ferromagnetic layers through the spacer by magnetostatic effect [53]. Assuming interface roughness followed a sinusoidal function, he derived the coupling energy to be

$$E_{néel} = -\frac{\pi p}{2\sqrt{2}} h_1 h_2 M_1 M_2 \cos(\alpha_1 - \alpha_2) e^{-pb\sqrt{2}},$$

where $p = 2\pi/L$, L is the wavelength of the roughness; h_1 and h_2 are amplitudes of roughness waves; M_1 and M_2 are the magnetization-intensity vector of the two ferromagnetic layers, $\alpha_1 - \alpha_2$ is the difference in the angles of M_1 and M_2, b is the thickness of spacer layer.

The Néel coupling favors parallel alignment of magnetization between the two ferromagnetic layers when the roughness of the two interfaces is correlated (the two interfaces have the same period and are in-phase). With a parallel alignment, the fringing field due to the topology between the two interfaces is lower compared to that in an antiparallel alignment configuration, as shown in Figure 2.12. Néel coupling is intrinsically a form of magnetostatic coupling. The coupling energy increases exponentially as the thickness of spacer layer decreases.

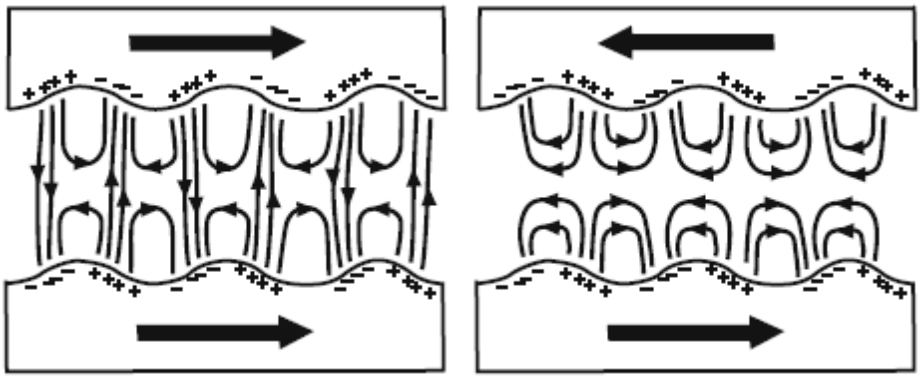

Figure 2.12 Fringing field with parallel and antiparallel magnetizations in two ferromagnetic layers with Néel coupling [47].

2.8 Magnetic coupling in layered magnetic nanostructures

Most studies on magnetic coupling in literatures focused on layered thin films. With thin film, it is easier to control the thickness and film morphology for the study of coupling mechanisms. In a layered magnetic nanostructure, the confined geometry induces shape anisotropy. Patterned structures such as strips, rhombic rings and circular rings have been studied to examine the coupling effect.

Mascaro *et al.* reported a simulation study of magnetic coupling in layered Co(5nm)/Cu(5nm)/NiFe(5nm) strips with a length of 2050nm and a

width of 200nm [54]. The simulation results showed strong magnetostatic coupling between the 360 ° domain wall in the Co layer and 180 ° domain wall in the NiFe layer. The stray field from 360 ° domain walls in the Co layer strongly influenced the magnetic behavior of the NiFe layer by promoting reverse domain nucleation in NiFe layer and providing a pinning potential which impeded domain wall propagation in NiFe layer.

In several studies on multilayer ellipsoidal, rhombic and circular rings, similar domain wall induced magnetostatic coupling was observed through simulation, magnetoresistance and MOKE measurements [55-59]. These rings were composed of layered stack of NiFe/Cu/Co with the thickness of Cu spacer in the range of 4 to 6 nm. The Co and NiFe layers were assumed to be exchange decoupled with a Cu spacer of such thickness. The stray field from the 360 ° domain walls in the hard Co layer strongly affected the magnetization reversal process of soft NiFe layer. Similar to layered magnetic stripes, the stray field can lead to promoted nucleation of reverse domain and pinning of domain walls in the NiFe layer. The magnetization reversal processes of NiFe ring can be qualitatively different compared to a single layer NiFe ring.

Jain *et al.* studied magnetization switching behaviors of concentric NiFe rings patterned by electron beam lithography. The rings had a height of 60 nm and ring widths of 200, 300 or 400 nm, concentrically patterned with a spacing of 80nm in between [60]. Strong magnetostatic coupling was observed between the domain walls of neighboring rings due to stray field from domain walls. The remanent magnetization in the outer rings had a tendency to form

antiparallel chirality with respect to their neighbors to reduce the total demagnetization energy.

In summary, previous studies on magnetic coupling in layered magnetic nanostructures focused mainly on vertically stacked layered structures. There is limited study in laterally engineered ferromagnetic structures. Other coupling mechanisms such as exchange coupling and Néel coupling are expected to emerge as the spacer gets thinner. The landscape of magnetic coupling can be quite different. With reduced dimensions, magnetostatic coupling at the edges of structures would also play a more important role in determining the overall magnetization states. Their effects have not fully examined yet and more work is demanded to investigate these coupling mechanisms in lateral layered nanostructures.

2.9 References

1. Heyderman, L. J., et al., *Fabrication of nanoscale magnetic ring structures and devices.* Microelectron. Eng., 2004. **73–74**(0): p. 780.
2. Zhu, F. Q., et al., *Ultrahigh-Density Arrays of Ferromagnetic Nanorings on Macroscopic Areas.* Adv. Mater., 2004. **16**(23-24): p. 2155.
3. Bayati, M., et al., *An Approach to Fabrication of Metal Nanoring Arrays.* Langmuir, 2010. **26**(5): p. 3549.
4. Kosiorek, A., et al., *Fabrication of Nanoscale Rings, Dots, and Rods by Combining Shadow Nanosphere Lithography and Annealed Polystyrene Nanosphere Masks.* Small, 2005. **1**(4): p. 439.

5. Li, Y. L., et al., *Large area Co nanoring arrays fabricated on silicon substrate by anodic aluminum oxide template-assisted electrodeposition.* Appl. Phys. Lett., 2012. **100**(18): p. 183101.

6. Singh, D. K., et al., *Arrays of ultrasmall metal rings.* Nanotechnology, 2008. **19**(24): p. 245305.

7. Singh, D. K., Krotkov, R., and Tuominen, M. T., *Magnetic transitions in ultra-small nanoscopic magnetic rings: Theory and experiments.* Phys. Rev. B, 2009. **79**(18): p. 184409.

8. Hulteen, J. C. and Martin, C. R., *A general template-based method for the preparation of nanomaterials.* J. Mater. Chem., 1997. **7**(7): p. 1075.

9. Hobbs, K. L., et al., *Fabrication of Nanoring Arrays by Sputter Redeposition Using Porous Alumina Templates.* Nano Lett., 2003. **4**(1): p. 167.

10. Dickey, M. D., et al., *Fabrication of Arrays of Metal and Metal Oxide Nanotubes by Shadow Evaporation.* ACS Nano, 2008. **2**(4): p. 800.

11. Daub, M., et al., *Ferromagnetic nanotubes by atomic layer deposition in anodic alumina membranes.* J. Appl. Phys., 2007. **101**(9): p. 09J111.

12. Huang, Y. C., et al., *Fabrication and magnetic properties of 100-nm-scaled permalloy nanotube arrays.* J. Vac. Sci. Technol. B, 2012. **30**(6): p. 06FF07.

13. Adeyeye, A. O. and Singh, N., *Large area patterned magnetic nanostructures.* J. Phys. D: Appl. Phys., 2008. **41**(15): p. 153001.

14. Luo, Y. and Misra, V., *Fabrication of large area nano-rings for MRAM application.* Microelectronic Engineering, 2008. **85**(7): p. 1555.

15. Adeyeye, A. O. and Singh, N., *Large area patterned magnetic nanostructures.* J. Phys. D: App.Phys., 2008. **41**(15): p. 153001.

16. Haynes, C. L. and Van Duyne, R. P., *Nanosphere Lithography: A Versatile Nanofabrication Tool for Studies of Size-Dependent Nanoparticle Optics.* J. Phys. Chem. B., 2001. **105**(24): p. 5599.

17. Md Jani, A. M., Losic, D., and Voelcker, N. H., *Nanoporous anodic aluminium oxide: Advances in surface engineering and emerging applications.* Progre. in Mat. Sci., 2013. **58**(5): p. 636.

18. Krishnan, R. and Thompson, C. V., *Monodomain High-Aspect-Ratio 2D and 3D Ordered Porous Alumina Structures with Independently Controlled Pore Spacing and Diameter.* Adv. Mater., 2007. **19**(7): p. 988.

19. Park, M., et al., *Block Copolymer Lithography: Periodic Arrays of ~1011 Holes in 1 Square Centimeter.* Science, 1997. **276**(5317): p. 1401.

20. Miltat, J. E. and Donahue, M. J., *Numerical Micromagnetics: Finite Difference Methods*, in *Handbook of Magnetism and Advanced Magnetic Materials*. 2007, John Wiley & Sons, Ltd.

21. Cowburn, R. P., et al., *Single-Domain Circular Nanomagnets.* Phys. Rev. Lett., 1999. **83**(5): p. 1042.

22. Kläui, M., et al., *Direct observation of spin configurations and classification of switching processes in mesoscopic ferromagnetic rings.* Phys. Rev. B, 2003. **68**(13): p. 134426.

23. Rothman, J., et al., *Observation of a Bi-Domain State and Nucleation Free Switching in Mesoscopic Ring Magnets.* Phys. Rev. Lett., 2001. **86**(6): p. 1098.

24. Getzlaff, M., *Fundamentals of Magnetism*. 2008: Springer.

25. Vaz, C. A. F., et al., *Ferromagnetic nanorings.* J. Phys.: Condens. Matter, 2007. **19**(25): p. 255207.

26. Laufenberg, M., et al., *Observation of thermally activated domain wall transformations.* Appl. Phys. Lett., 2006. **88**(5): p. 052507.

27. Klaui, M., et al., *Head-to-head domain-wall phase diagram in mesoscopic ring magnets.* Appl. Phys. Lett., 2004. **85**(23): p. 5637.

28. Shimon, G., Adeyeye, A. O., and Ross, C. A., *Comparative study of magnetization reversal process between rectangular and circular thin film rings.* J. Appl. Phys., 2012. **111**(1): p. 013909.

29. Li, S. P., et al., *Flux Closure Structures in Cobalt Rings.* Phys. Rev. Lett., 2001. **86**(6): p. 1102.

30. Nam, C., Mascaro, M. D., and Ross, C. A., *Magnetostatic control of vortex chirality in Co thin film rings.* Appl. Phys. Lett., 2010. **97**(1): p. 012505.

31. Li, D. D., et al., *Template-based Synthesis and Magnetic Properties of Cobalt Nanotube Arrays.* Adv. Mater., 2008. **20**(23): p. 4575.

32. Wang, Z. K., et al., *Spin Waves in Nickel Nanorings of Large Aspect Ratio.* Phys. Rev. Lett., 2005. **94**(13): p. 137208.

33. Chang, C. R., Lee, C. M., and Yang, J. S., *Magnetization curling reversal for an infinite hollow cylinder.* Phys. Rev. B, 1994. **50**(9): p. 6461.

34. Han, X. F., et al., *Structural and Magnetic Properties of Various Ferromagnetic Nanotubes.* Adv. Mater., 2009. **21**(45): p. 4619.

35. Parkin, S. S. P., More, N., and Roche, K. P., *Oscillations in exchange coupling and magnetoresistance in metallic superlattice structures: Co/Ru, Co/Cr, and Fe/Cr.* Phys. Rev. Lett., 1990. **64**(19): p. 2304.

36. Krompiewski, S., Krey, U., and Pirnay, J., *Exchange coupling and magnetization in bcc-(001) Fe/Cu multilayers by a tight-binding LMTO-ASA method.* J. Magn. Magn. Mater., 1993. **121**(1-3): p. 238.

37. Edwards, D. M., et al., *Oscillations of the exchange in magnetic multilayers as an analog of Haas-van Alphen effect.* Phys. Rev. Lett., 1991. **67**(4): p. 493.

38. Slonczewski, J. C., *Mechanism of interlayer exchange in magnetic multilayers.* J. Magn. Magn. Mater., 1993. **126**(1-3): p. 374.

39. Slonczewski, J. C., *Fluctuation mechanism for biquadratic exchange coupling in magnetic multilayers.* Phys. Rev. Lett., 1991. **67**(22): p. 3172.

40. Wang, Y., Levy, P. M., and Fry, J. L., *Interlayer magnetic coupling in Fe/Cr multilayered structures.* Phys. Rev. Lett., 1990. **65**(21): p. 2732.

41. Bruno, P. and Chappert, C., *Oscillatory coupling between ferromagnetic layers separated by a nonmagnetic metal spacer.* Phys. Rev. Lett., 1991. **67**(12): p. 1602.

42. Bruno, P. and Chappert, C. *Interlayer exchange coupling: RKKY theory and beyond*. in *NATO ARW*. 1992. Cargese, Corsica, France.

43. Ruderman, M. A. and C. Kittel, Phys. Rev., 1954. **96**.

44. T. Kasuya, Prog. Theor. Phys., 1956. **16**.

45. K. Yosida, Phys. Rev., 1957. **106**: p. 893.

46. Rijks, T. G. S. M., et al., *Interplay between exchange biasing and interlayer exchange coupling in Ni80Fe20/Cu/Ni80Fe20/Fe50Mn50 layered systems.* J. Appl. Phys., 1994. **76**(2): p. 1092.

47. Stiles, M. D., Bland, J. A. C., and Heinrich, B., *Interlayer Exchange Coupling*, in *Ultrathin Magnetic Structures III*. 2005, Springer Berlin Heidelberg. p. 99.

48. Biragnet, F., et al., *Interactions between Domain Walls in Coupled Films.* Phys. Sta. Soli. (B), 1966. **16**(2): p. 569.

49. Fuller, H. W. and Sullivan, D. L., *Magnetostatic Interactions between Thin Magnetic Films.* J. Appl. Phys., 1962. **33**(3): p. 1063.

50. Kuch, W., et al., *Layer-resolved imaging of magnetic interlayer coupling by domain-wall stray fields.* Phys. Rev. B, 2003. **67**(21): p. 214403.

51. Lew, W. S., et al., *Mirror Domain Structures Induced by Interlayer Magnetic Wall Coupling.* Phys. Rev. Lett., 2003. **90**(21): p. 217201.

52. Thomas, L., Samant, M. G., and Parkin, S. P., *Domain-Wall Induced Coupling between Ferromagnetic Layers.* Phys. Rev. Lett., 2000. **84**(8): p. 1816.

53. Néel, L., Comptes. Rendus, 1962. **255**: p. 1676.

54. Mascaro, M. D., Nam, C., and Ross, C. A., *Interactions between 180° and 360° domain walls in magnetic multilayer stripes.* Appl. Phys. Lett., 2010. **96**(16): p. 162501.

55. Castaño, F. J., et al., *Spin-Dependent Scattering in Multilayered Magnetic Rings.* Phys. Rev. Lett., 2005. **95**(13): p. 137201.

56. Hayward, T. J., et al., *Switching behavior of individual pseudo-spin-valve ring structures.* Phys. Rev. B, 2006. **74**(13): p. 134405.

57. Mascaro, M. D., et al., *360 °domain wall mediated reversal in rhombic Co/Cu/NiFe magnetic rings.* Appl. Phys. Lett., 2011. **98**(25): p. 252506.

58. Lee, J. H., et al., *Influence of thermal excitation on magnetization states and switching routes of magnetic multilayer rings.* J. Appl. Phys., 2009. **105**(7): p. 3.

59. Jain, S. and Adeyeye, A. O., *Low temperature investigations of switching processes in multilayer rings.* J. Appl. Phys., 2009. **106**(2): p. 4.

60. Jain, S. and Adeyeye, A. O., *Aligned Alternating Head-to-Head and Tail-to-Tail Domain Walls in Ferromagnetic Concentric Rings.* IEEE Trans. Magn., 2010. **46**(6): p. 1595.

Chapter 3 Experimental Techniques

3.1 Introduction

In this chapter, the experimental techniques used to synthesize and characterize the ferromagnetic nanostructures in this work are discussed in detail. The ferromagnetic nanostructures studied in this work include highly ordered array of $Ni_{80}Fe_{20}$ Permalloy (NiFe) nanodisks, nanoparticles, cylindrical nanoshells, perforated nanocup, nanocups and concentric layered NiFe-Au-NiFe nanoshells. The fabrication processes include thermal oxidation, interference lithography, reactive ion etching (RIE), electron beam evaporation, lift off and high temperature dewetting. The topologies and structures were characterized using scanning electron microscopy (SEM), transmission electron microscopy (TEM) and energy dispersive X-ray spectroscopy (EDX). Details on magnetic characterization techniques and micromagnetic simulations are also presented.

3.2 General process flows for fabrication of nanostructures

Figure 3.1 shows the fabrication process for nanodisk and nanoparticle arrays. A developer-soluble anti-reflective coating (ARC) layer and negative photoresist were spin-coated on a silicon wafer already coated with SiO_2. An array of holes was patterned using the interference lithography method with

the Lloyd's mirror setup. The residual layer of ARC was then cleaned using an O_2 plasma. NiFe was then deposited in an electron beam evaporator. A lift off process resulted in ordered array of nanodisks. Array of nanoparticles were realized through a high temperature dewetting process with the sample heated up to 600 – 850 ℃ in reductive forming gas.

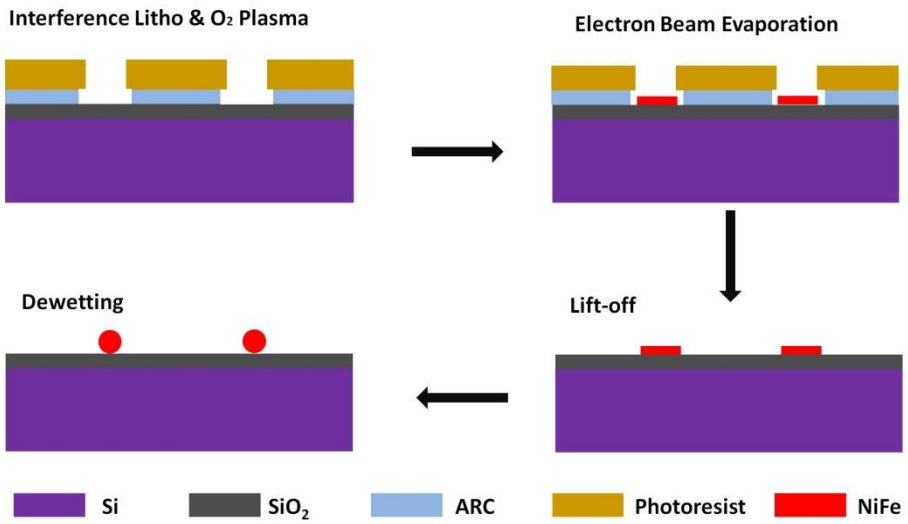

Figure 3.1 Schematics of fabrication process for nanodisk and nanoparticle array.

Figure 3.2 depicts the fabrication process for ordered arrays of cylindrical nanoshells. Arrays of holes were patterned in the resist stack using interference lithography. The pattern was then transferred into the silicon substrate using RIE. Subsequently, NiFe was deposited on the sidewall of the holes through an angular deposition process [1] in an electron beam evaporator. The tilting angle was in the range of 32-38°. The final lift-off process led to arrays of NiFe cylindrical nanoshells. Depending on the template geometry and tilt angle during NiFe deposition, the final structures

could also be perforated nanocups or unperforated nanocups. Concentric layered nanoshells could also be achieved with sequential deposition of NiFe, Au and NiFe.

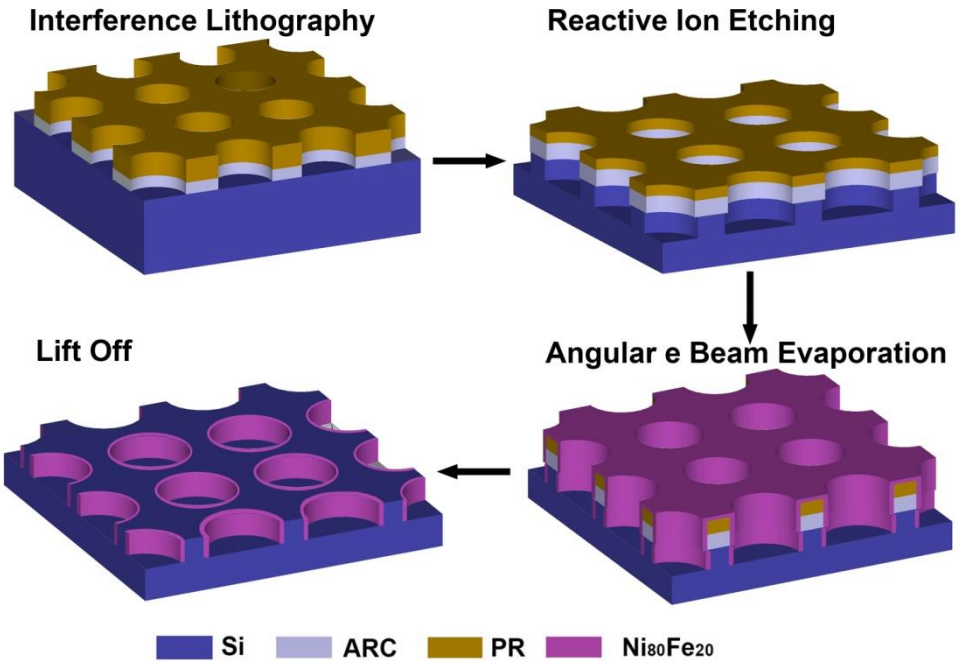

Figure 3.2 Schematics of fabrication process for cylindrical nanoshells.

3.2.1 Wafer Cleaning

Two-inch p-type <100> silicon wafers with resistivity of 4 – 8 Ωcm^{-1} were used as substrates in this work. The wafers were cleaned using standard Radio Corporation of America (RCA) cleaning method. The exact procedure is outlined below.

RCA I solution was prepared by mixing hydrogen peroxide, ammonium hydroxide and de-ionized (DI) water in the ratio of 1:1:5 by volume. The solution was heated to 80–90 ℃, and wafers were immersed inside for 15 minutes. This would clean the organic contaminants, groups I and II metals as

well as some other metals like Cu, Ni and Zn etc. The wafers were then rinsed in DI water in nitrogen (N_2) bubbler for another 10~15 min [2].

RCA II solution was prepared by mixing hydrochloric acid, hydrogen peroxide DI water in the ratio of 1:1:6 by volume. The RCA II solution was then heated to 80–90 ℃ and the wafers were immersed in the heated solution for 15 min. This step removes alkali ions and other cations like Fe^{3+}, Al^{3+}, and Mg^{2+} which form insoluble hydroxides in basic solutions of RCA I [2]. The wafers were then rinsed with DI water with in N_2 bubbler for 10~15 min.

During RCA I and II cleaning, the surface layer of silicon gets oxidized due to exposure to hydrogen peroxide. In addition, a thin layer of native oxide grows on the wafer surface even at room temperature. To remove this layer of oxide prior to subsequent processing, the wafers were immersed in 10% hydrofluoric acid (HF) for around 30 sec. Then, the wafers were immersed in DI water with a nitrogen bubbler for 20 minutes to remove the residual HF acid. The wafers were then blown dry with a nitrogen gun.

3.2.2 Thermal oxidation

An oxide layer was grown on the silicon wafer as a diffusion barrier between the substrate and the materials. This was only for samples in the dewetting study. Dry oxidation was used for its better control and uniformity of thickness as well as higher quality compared to wet oxidation. A layer of SiO_2 with a thickness of 50nm was grown while the samples were heated at 1000 ℃ in a Tystar oxidation furnace. The oxide thickness was verified with an ellipsometry measurement.

3.2.3 Spin coating of anti-reflection coating and photoresist

A developer soluble anti-reflection coating (ARC) WiDE-8C from Brewer Science was spin-coated onto the wafers at 3000 rpm. The samples were then annealed on a hot plate firstly at 100 ℃ for 30 seconds. This would drive away residual solvent and release the stress in the film. Subsequently, the samples were baked at 168 ℃ for 1 minute to crosslink the polymer giving appropriate solubility and optical properties to reduce reflection during lithography exposure. After annealing, the thickness of ARC was measured to be around 70nm in SEM.

Following that, a layer of TSMR-i032 negative photoresist was spin-coated on top of the ARC layer at 6000 rpm. The film was then annealed on a hot plate at 90 ℃ for 90 seconds. The thickness of photoresist was measured to be around 260nm.

3.2.4 Reactive Ion Etching

An Oxford PlasmaLab 80 reactive ion etcher was used for pattern transfer from the photoresist stack into the silicon substrate. The RIE chamber was first cleaned with oxygen plasma to eliminate contaminants. Certain contaminants, especially dielectric thin films on the chamber, have great impact on the DC bias voltage at given RF power, hence greatly affects the etching results.

After lithography, there was still a thin residual layer of ARC at bottom of the holes. First, the residual ARC was cleaned with O_2 as the processing gas. The hole-array pattern was then transferred into Si by the plasma with a mixed

processing gas of SF_6, CHF_3 and O_2. The RF power, processing pressure and composition of processing gas determines the final etching profile in silicon. The parameters were optimized and more details are discussed in following chapters.

3.2.5 Electron beam evaporation

An electron beam evaporation system was used to deposit NiFe and Au. The material to be evaporated was loaded into a Molybdenum crucible in the form of pellets or wires. The chamber was evacuated to a base pressure of 3×10^{-7} Torr with a turbo pump and ion pump. The electron beam was generated by applying a high voltage on the heated filament. The generated electron beam was then accelerated by the high voltage bias and focused to the crucible with a magnetic field. Kinetic energy of the electrons was converted into thermal energy as the beam bombarded the surface of the material to be deposited. With a beam current high enough, a liquid melt formed and material started to evaporate. Flux reaching the substrate resulted in deposition on the sample surface.

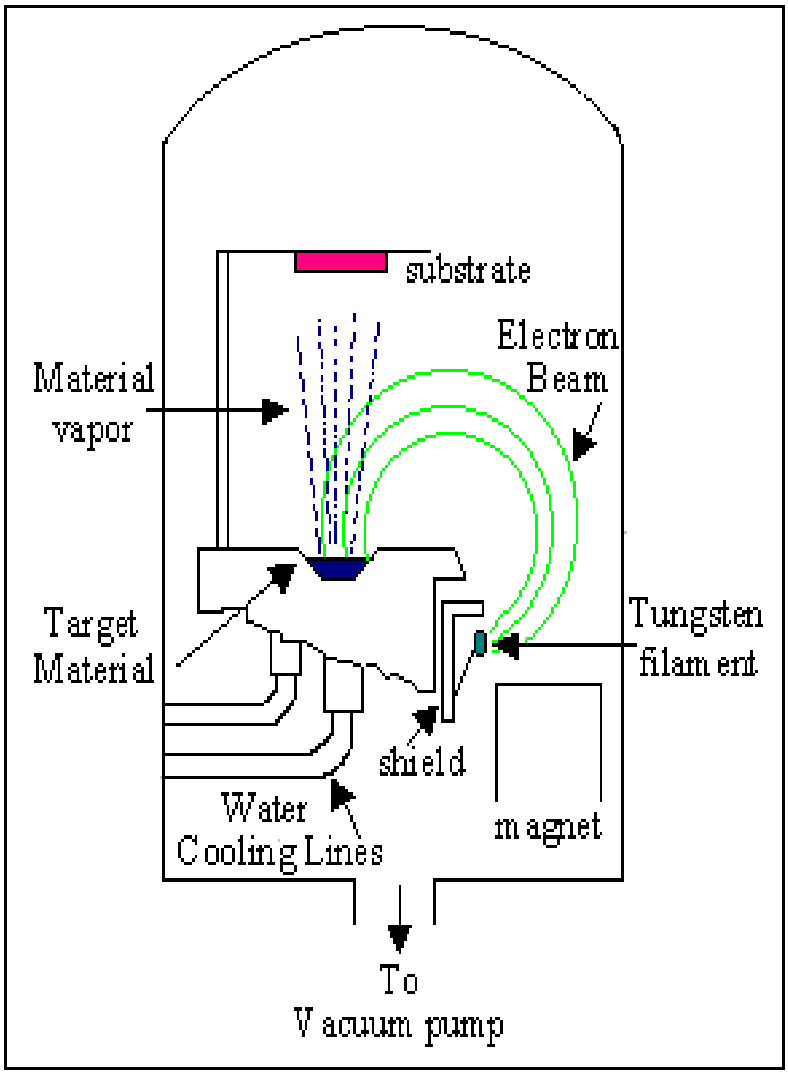

Figure 3.3 Schematics of an electron beam evaporator.

The electron beam evaporator used in this work was equipped with a custom made rotational stage that could be tilted at controlled angles, as shown in Figure 3.4. The flux comes at an angle with respect to the normal of the sample during evaporation such that the sidewall and base of the holes could be coated. The rotation of the substrate holder was driven by a rotary motor through a series of worm gears and shafts.

Figure 3.4 Custom made substrate holder with controllable tilting angle.

3.2.6 Lift Off

After deposition, lift off was done by immersing the sample in NMD-03 developer solution in an ultrasonic bath. The ARC got dissolved in the developer and lift off the photoresist and metal deposited on the ARC photoresist stack. Only the metal deposited inside the holes were left to form the nanostructure desired. The sample was then washed with acetone in ultrasonic bath and then blown dry with nitrogen gun.

3.2.7 Dewetting

At high temperatures, metallic thin film tends to agglomerate or dewet into particles favored by reduction in surface and interfacial energies [3]. Dewetting of NiFe in this work was carried out in a horizontal three-zone

furnace, as shown in Figure 3.5. The samples were placed on a quartz substrate carrier and then loaded to the middle zone of the furnace. The tube was first flushed with nitrogen for 30mins to reduce the residual oxygen concentration induced during sample loading. Following that, forming gas (90% nitrogen, 10% hydrogen) was directed through the tube at 1100 to 2200 SCCM. This would establish a reductive ambient and prevent oxidation of metals. Dewetting was carried out with sample heated up to 600 – 850 ℃ for 1 to 3 hours in forming gas, and then cooled down in the tube.

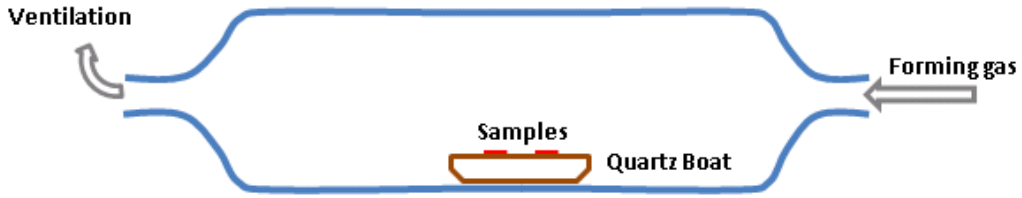

Figure 3.5 Schematics of horizontal tube furnace.

3.3 Lloyd's mirror interference lithography

Interference lithography is a mask-free and parallel patterning technique by the interference of two coherent laser beams. This can be achieved either using a Mach-Zehnder interferometer with a beam splitter and additional optics, or with a Lloyd's mirror setup [4]. Compared with the Mach-Zehnder system, Lloyd's mirror is easier to set up, and more flexible when changing the interference angle as it does not require re-aligning the optics. For this work, a Lloyd's mirror setup was used with a 325 nm continuous wave helium-cadmium (He-Cd) laser as the light source

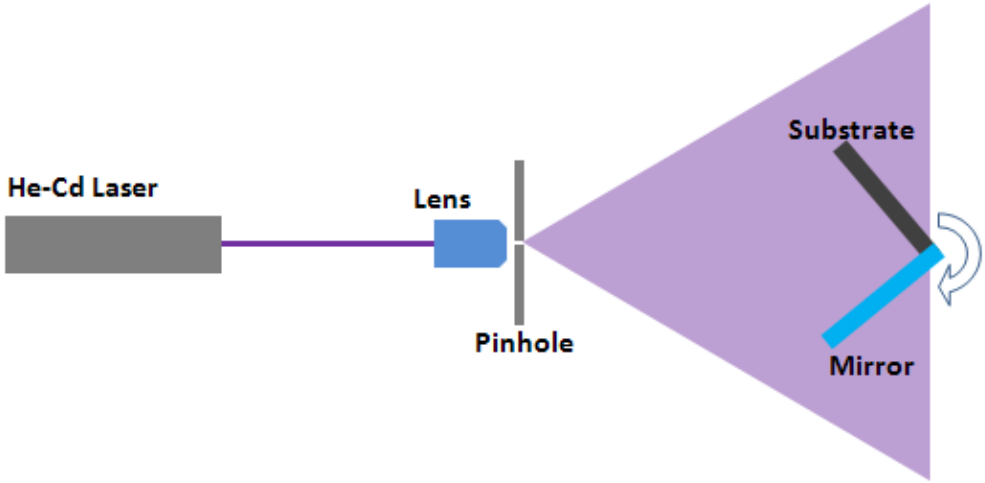

Figure 3.6 Schematics of Lloyd's Mirror Interferometer.

Figure 3.6 shows the schematic setup of our Lloyd's mirror interferometer. The laser beam was first focused by a lens and directed through to a spatial filter pinhole with a diameter of 10 μm to remove noise from the beam. This would lead to a cleaner Gaussian profile in the beam. After the spatial filter, the beam was expanded over a length of approximately 0.8 meter. As the Gaussian beam expands, the intensity would drop and radius of wave front would increase. Although lower intensity means longer exposure time, beam expansion at this scale is still beneficial as the increase in wave front can give larger area at the beam center with reasonably uniform intensity. A larger area of the beam can be approximated as plane wave.

An aluminum mirror (99% UV reflectance) was used for its higher UV reflectivity and more constant reflectivity over a broad range of angles compared to other mirrors. The stage rotation axis was aligned to cross the optical axis. The light from the original beam would interfere with the light reflected from the mirror to form a standing wave pattern. This would generate an array of lines with alternating intensity maxima and minima. The period

equal to $\lambda/2\sin\theta$, where λ is the wavelength of the light, and θ is the half the angle between the two beams. Array of holes were patterned in the TSMR-i032 negative photoresist by exposing the sample twice, with sample rotated 90 ° before the second exposure. The diameter and period of holes were determined by the exposure dose and interference angle.

Development of the exposed photoresist was carried out with NMD-03 developer. The exposed sample was immersed into the developer for typically 60 sec. Development time depends on the dissolve rate of ARC layer. The sample was then rinsed with DI water and then dried with nitrogen gun.

3.4 NiFe Nanodisks and Dewetted Nanoparticles

The experimental procedures to synthesize ordered array of nanodisk and nanoparticle are depicted in Figure 3.7. Firstly, the silicon wafer was cleaned with RCA cleaning method and native oxide was stripped in diluted HF solution. A layer of SiO_2 with a thickness of 50nm was grown on the wafer with dry oxidation method. This oxide served as a diffusion barrier in the latter high temperature dewetting process. Array of holes were patterned in a developer-soluble antireflection coating (ARC) and negative photoresist stack with Lloyd's mirror interference lithography. The residual ARC and resist (if any) were cleaned in O_2 plasma. Subsequently, NiFe was deposited in an electron beam evaporator. A lift-off process would lead to ordered diperiodic array of nanodisks. Nanoparticle array was achieved by dewetting of these nanodisks under high temperature annealing in forming gas (N_2, 90% + H_2, 10%).

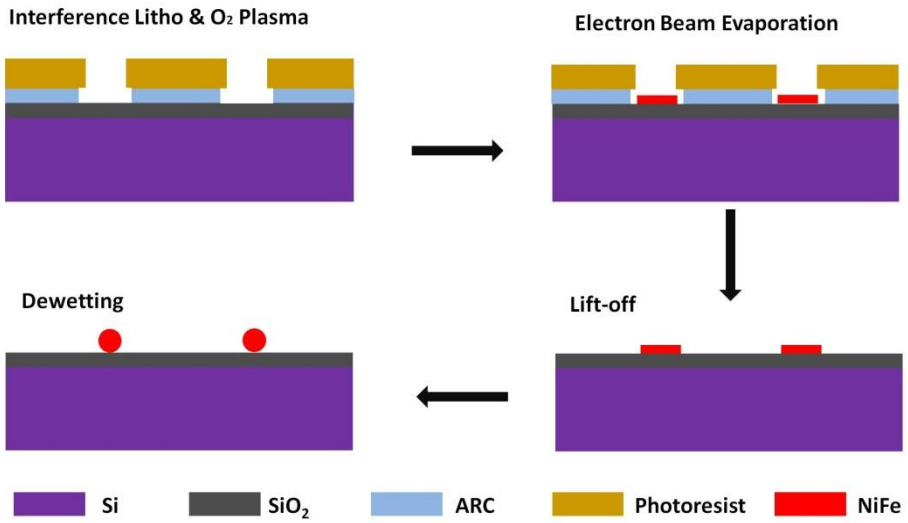

Figure 3.7 Schematics of the synthesis process for nanodisk and nanoparticle arrays.

It was important to get an appropriate undercut structure as shown in Figure 4.2 to ensure an easier lift-off process.

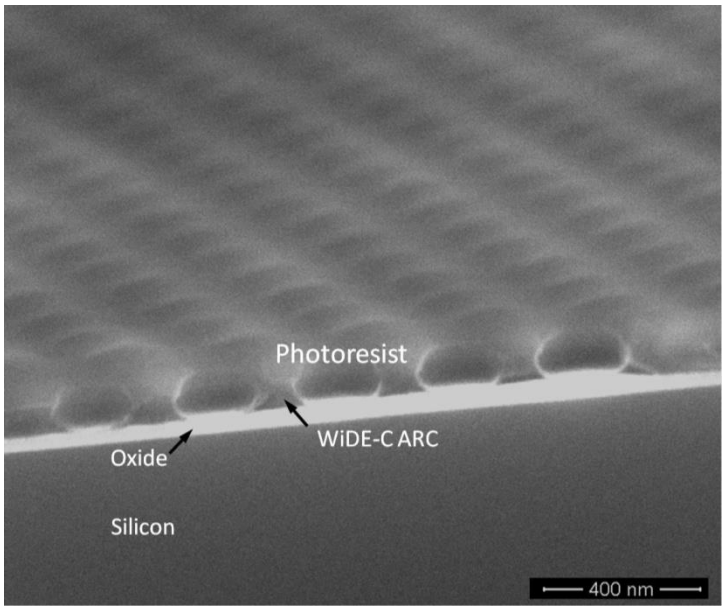

Figure 3.8 SEM cross-sectional view of sample after lithography with appropriate undercut.

The two factors to achieve appropriate undercut profile in the resist-ARC stack were: solubility of developer-soluble ARC and development time.

The solubility of WiDE-C ARC in developer was sensitive to thermal history in the annealing process. If the baking time was insufficient or the baking temperature was too low, the dissolution rate would be too high. The whole resist-ARC stack got rinsed off from the substrate very easily. On the other hand, excessive baking would make the ARC difficult to dissolve in the NMD-3 developer, hence leaving a thick ARC layer after development, as shown in Figure 3.9. Even though the ARC can be etched in O_2 plasma, the lift-off would still be difficult because the ARC was insoluble.

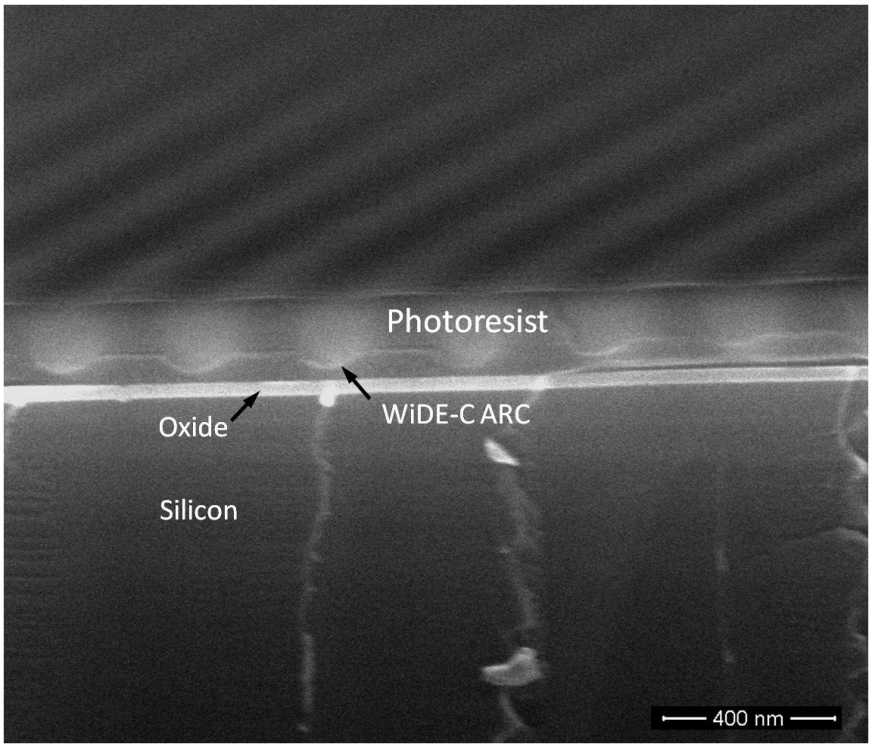

Figure 3.9 SEM cross-sectional view of sample after lithography with excessive WiDE-C ARC.

Besides proper solubility of ARC required, development time also need to be well controlled. Over development would leave too much undercut in the ARC. This would deteriorate the structural integrity of resist-ARC stack. The photoresist could be rinsed off due to insufficient adhesion. Under development would lead to excessive ARC left over. It could be removed with

O_2 plasma, as shown in Figure 3.10. However, the photoresist would also get etched excessively while etching the thick ARC layer due to poor selectivity. The sidewall of holes was vertical without any undercut or overhang to assist the lift-off process.

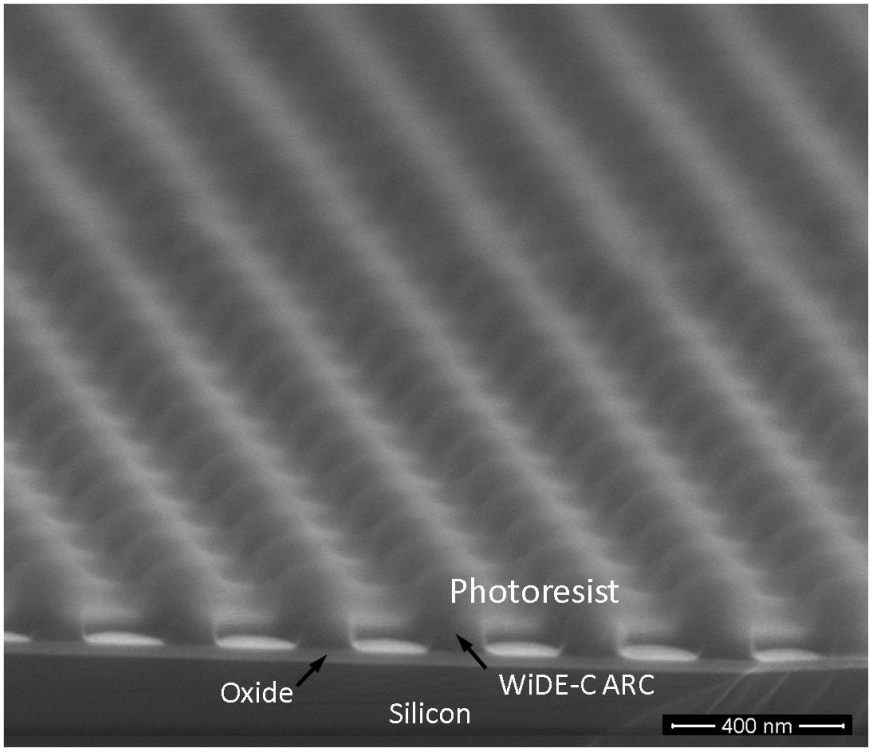

Figure 3.10 SEM cross-sectional view of sample after etching away excessive WiDE-C ARC.

The lift-off was done with the sample immersed in NMD-3 developer in an ultrasonic bath. The debris was cleaned by rinsing the sample with acetone. Figure 3.11 shows one of the NiFe nanodisk arrays achieved. The array was highly ordered with a period of 250nm. With our Lloyd's mirror setup, sample size of around $0.8cm^2$ could be patterned, which contained 1.28 billion nanodisks. This can be further scaled up with an interferometer setup or by

increasing the distance between the sample and pinhole as discussed in Chapter 3.

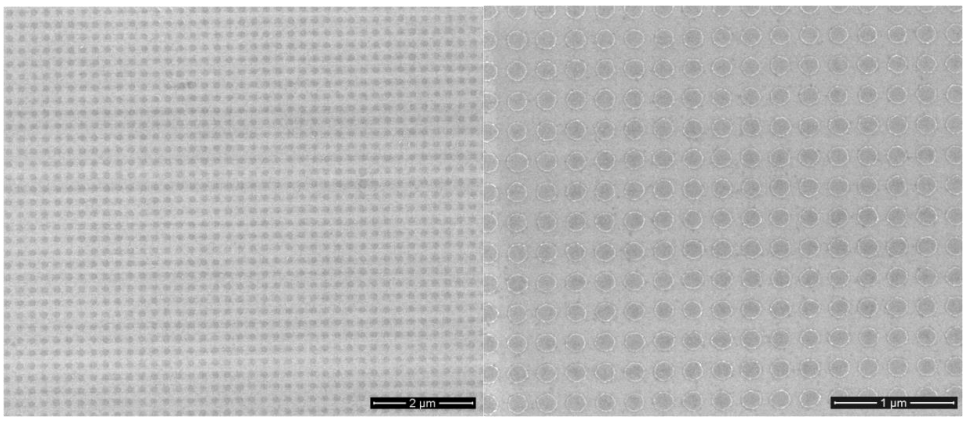

Figure 3.11 SEM of NiFe nanodisk array (Diameter = 150nm, Period = 250nm).

The nanodisks had a thickness of 15nm. The average diameter was 163.6nm with a standard deviation of 5.2nm. The histogram of nanodisk diameter distribution is shown in Figure 3.12.

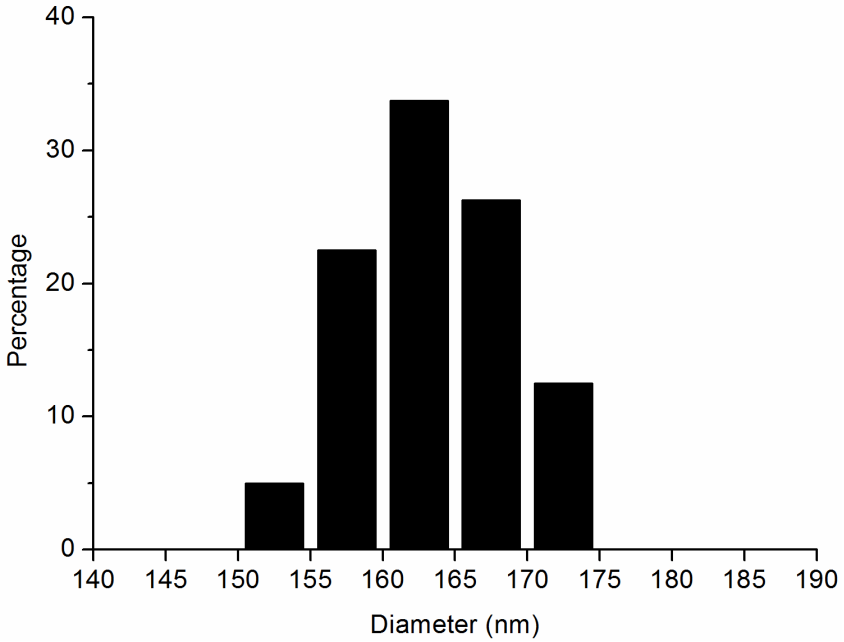

Figure 3.12 Histogram of nanodisk diameter distribution.

Figure 3.13 shows the scanning electron micrographs of NiFe nanoparticle array after dewetting at different conditions. Before dewetting, the nanodisk array had a period of 320nm, a diameter around 180nm and a thickness of 15nm. When annealed at 500℃ or 600℃ for 30 minutes, separated nanoparticles were observed from dewetting of each nanodisk. There was one bigger nanoparticle present at the centre surrounded by smaller nanoparticles from dewetting of individual nanodisk. Annealing at 800℃ for 3 hours reduced the volume of surrounding nanoparticles, but still did not lead to single nanoparticle from one disk after dewetting. In comparison, dewetting of Ni and NiPt (Pt, 10wt%) nanodisk with similar dimension led to one nanoparticle per nanodisk [5]. It was also observed that the surrounding smaller nanoparticles possessed more faceting than the centre nanoparticles.

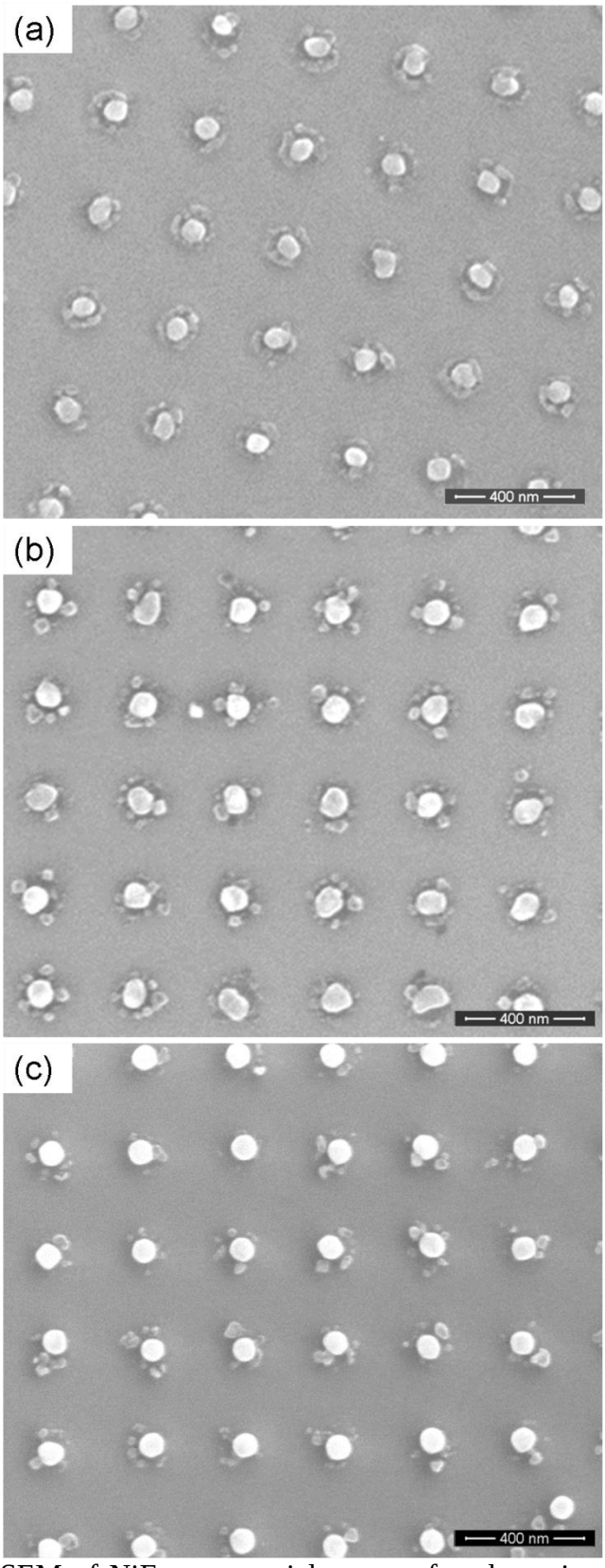

Figure 3.13 SEM of NiFe nanoparticle array after dewetting: (a) 500 ℃, 30 minutes; (b) 600 ℃, 30 minutes; (c) 850 ℃, 3 hours.

3.5 NiFe cylindrical nanoshell, nanocup and perforated nanocup

The fabrication process of large scale ordered $Ni_{80}Fe_{20}$ nanoshell array is depicted in Figure 3.14. The right column shows the SEM micrographs after each step. A developer-soluble anti-reflective coating (ARC) WiDE-C and negative photoresist TSMR-iN032 were spin-coated on silicon wafer. Note that baking of WiDE-C ARC has a small process window and has to be carefully controlled. Also a prolonged baking at high temperature would lead to over aging of ARC and make it less soluble in the NMD-03 developer. Consequently, the final lift off would be very difficult or even fail completely. On the other hand, insufficient baking would make the ARC too soluble; the pattern can be completely rinsed off very quickly after interference lithography during the development process. A 30-second bake on hotplate at 100 ℃ was carried out to remove the residual solvent; following that a 1-min bake at 168 ℃ would cure the ARC, giving appropriate solubility in developer NMD-03. However, towards the end of shelf life, the ARC aged by itself. We found that process re-optimization was necessary and shorter baking time or lower temperature was required.

Diperiodic arrays of holes were patterned in the resist stack using interference lithography with Lloyd's mirror and a 325 nm helium–cadmium continuous wave laser, as described in Chapter 3. In interference lithography, the exposure dose and interference angle determine the diameter of holes and period of array. The ARC layer effectively reduced standing wave and swing wave and improved the line width. The exposed sample was then developed in

NMD-03 developer. In the development process, the ARC layer also dissolved. Depending on the dissolution rate of ARC, the development time was fine tuned. Under development leaved an excessive residual layer of ARC and photoresist; while over development resulted in a large undercut in the ARC, deteriorating the mechanical stability of pattern.

The pattern in the photoresist-ARC stack was then transferred to the silicon substrate using an Oxford PlasmaLab 80 reactive ion etching (RIE) system with mixed SF_6, CHF_3 and O_2 processing gases. Subsequently, $Ni_{80}Fe_{20}$ was deposited on the sidewall of the holes by an angular deposition process[1] in an electron beam evaporator. The evaporator is equipped with an in-house customized stage as discussed in Chapter 3. The rotating substrate was tilted at an angle with respect to the flux during evaporation. At proper angle determined by the diameter of holes and thickness of photoresist-ARC stack, the evaporation flux is properly shadowed so that there was only deposition on the side wall.

The final lift-off process was done by immersing the sample in NMD-03 developer in an ultrasonic bath. The developer was alkaline in nature, and hence corrosion and oxidization of $Ni_{80}Fe_{20}$ in the solution can be minimized. The developer would dissolve the ARC layer and lift off the metal on top, leading to large scale ordered array of $Ni_{80}Fe_{20}$ nanoshells.

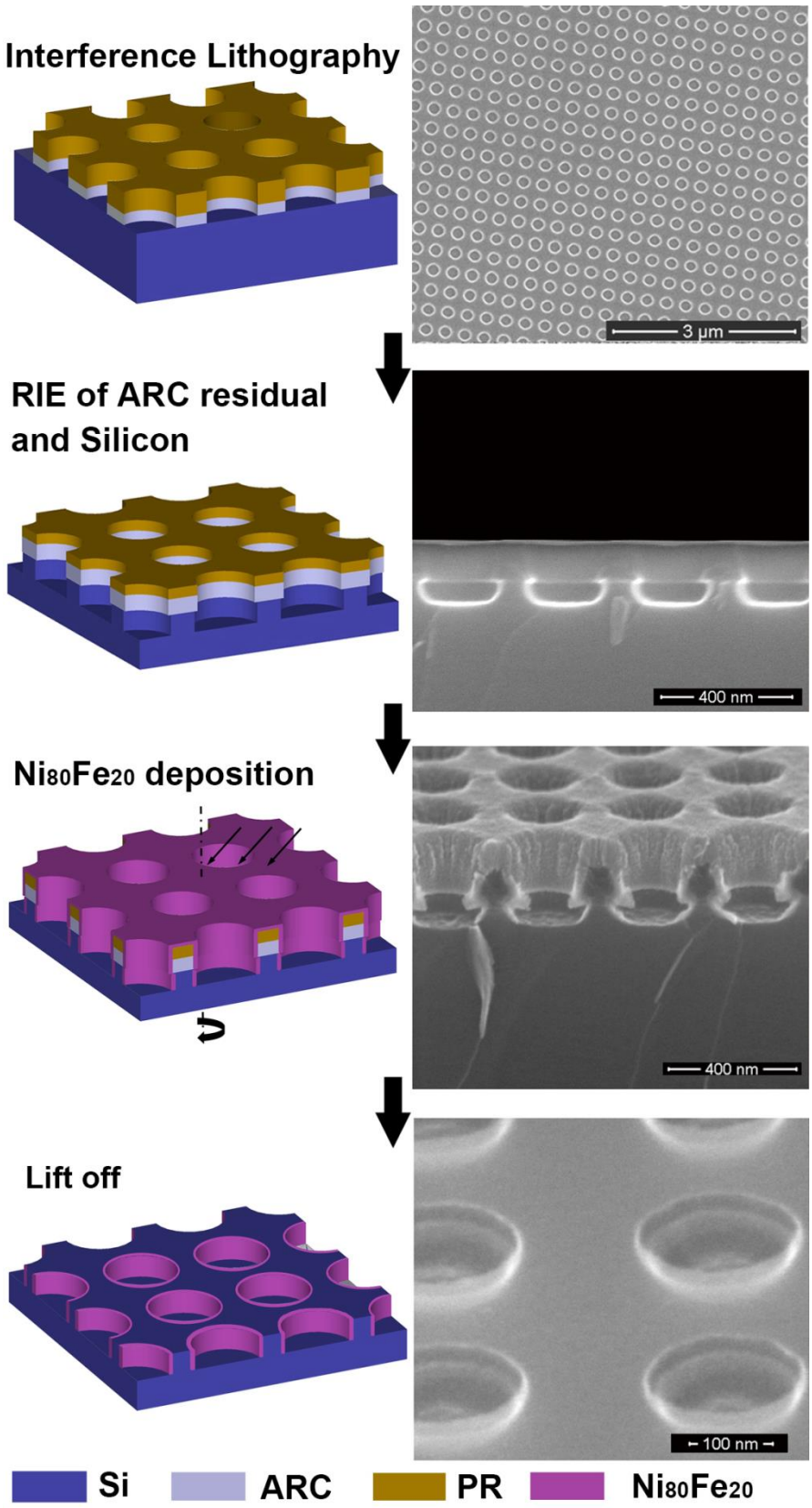

Figure 3.14 Schematic of nanoshell array fabrication process and SEM micrographs after each process step.

The small under-cut profile present at the sidewall after etching is important to realize successful lift off process (Figure 3.14). However, too much side etching leads to an undesired excessive undercut etching profile, as shown in Figure 3.15. As a result, over-shadowing would occur during e beam evaporation.

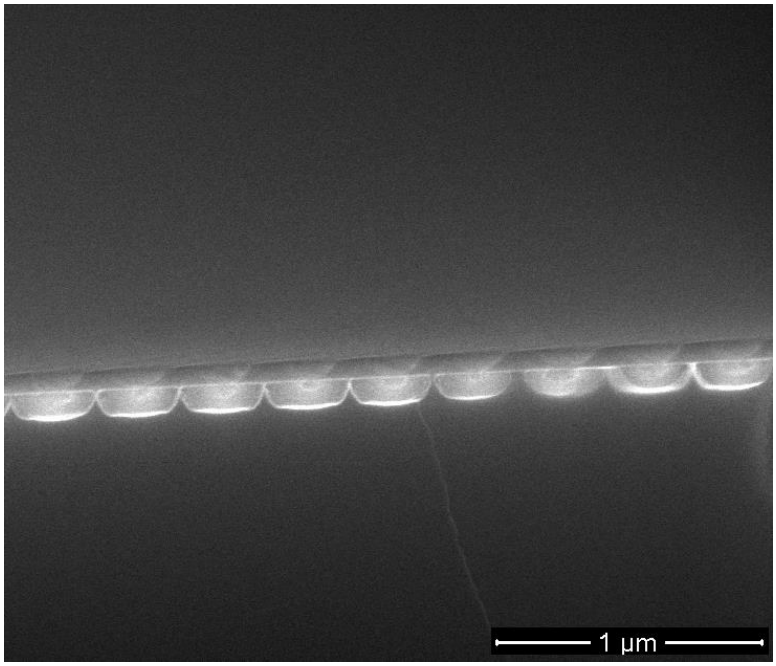

Figure 3.15 Excessive undercut in silicon after reactive ion etching.

Etching is optimized with a two-step process. Firstly, the WiDE C anti-reflection coating residual was removed by oxygen plasma with an O_2 flow rate at 40 SCCM, a pressure of 40 mTorr and a RF power of 200 W. The etching time varied from 6 to 10 seconds depending on the thickness of residual layer. Etching of silicon was performed with a mixture processing gas of SF_6, CHF_3 and O_2 with flow rates of 40, 4 and 17 SCCM, respectively. The plasma was ignited at a pressure of 60 mTorr and a RF power of 160 W. Etching time was typically around 14 seconds. The addition of CHF_3 formed a

thin layer of Carbon-Fluorine polymer which protects the sidewall. The directional O_2 plasma removed the polymer at the bottom so that etching of could proceed into silicon.

If CHF_3 ratio was too high or O_2 ratio was too low, the polymer at bottom of etching front would not be effectively removed. The etching rate slowed down and etching profile became a bowl-shape, as shown in Figure 3.16. Lift off of $Ni_{80}Fe_{20}$ film deposited on this pattern was difficult because the thin film cover conformally, leaving no contact between the ARC and developer.

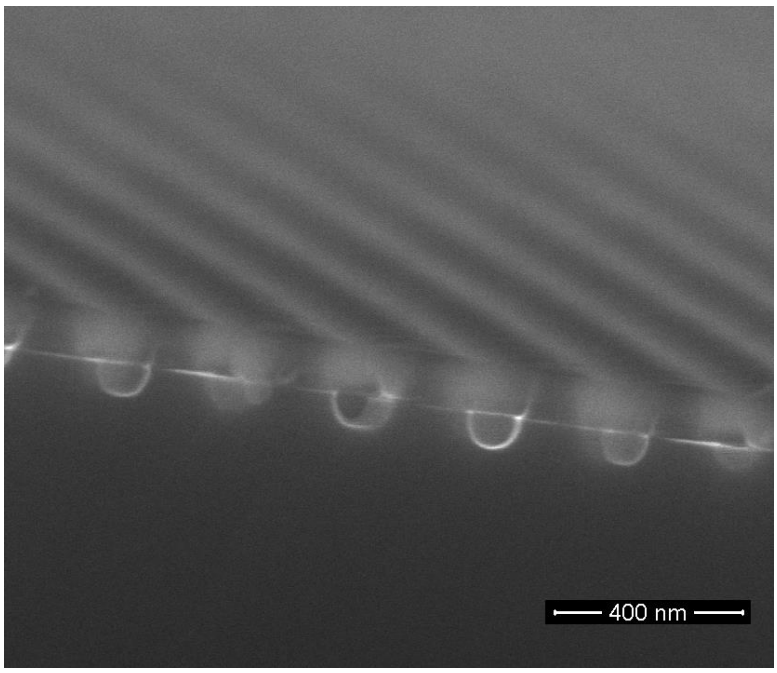

Figure 3.16 SEM cross-sectional view of typical bowl-shaped etching profile if CHF_3 : O_2 ratio was too high.

Figure 3.17 shows the ordered array of nanoshell after lift-off. This method is highly versatile in the fabrication of nanostructures of the dimension and geometry used in this work. The period of the arrays varies from 250nm to 400nm, and the diameter of nanoshell ranges from 180nm to 300nm. The

shell width ranges from 25nm down to sub-10nm, and the height ranges from 30 to 50nm. These nanomagnets are difficult to achieve by conventional planar patterning techniques.

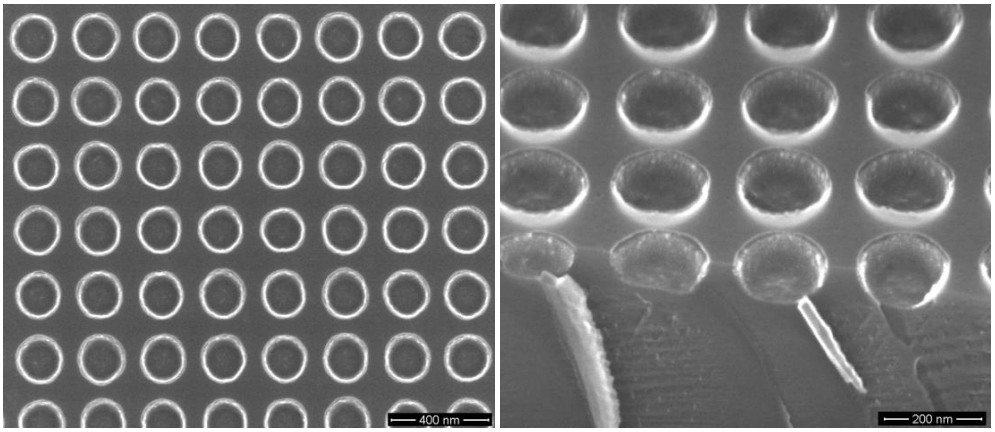

Figure 3.17 Top view and 45 ° tilted view SEM micrographs of nanoshell fabricated for this work.

When tilted at appropriate angle during deposition, the $Ni_{80}Fe_{20}$ flux is deposted on the sidewall as well as part of the bottom of the holes in the silicon substrate to form a circular thin-film ring shaped base. Perforated nanocups form after lift off, as shown in Figure 3.18 (a). Tilted at higher angle, the depostion flux would fully cover the bottom and form a fully covered disk-base. This leads to nanocup arrays after lift off, as shown in Figure 3.18 (b).

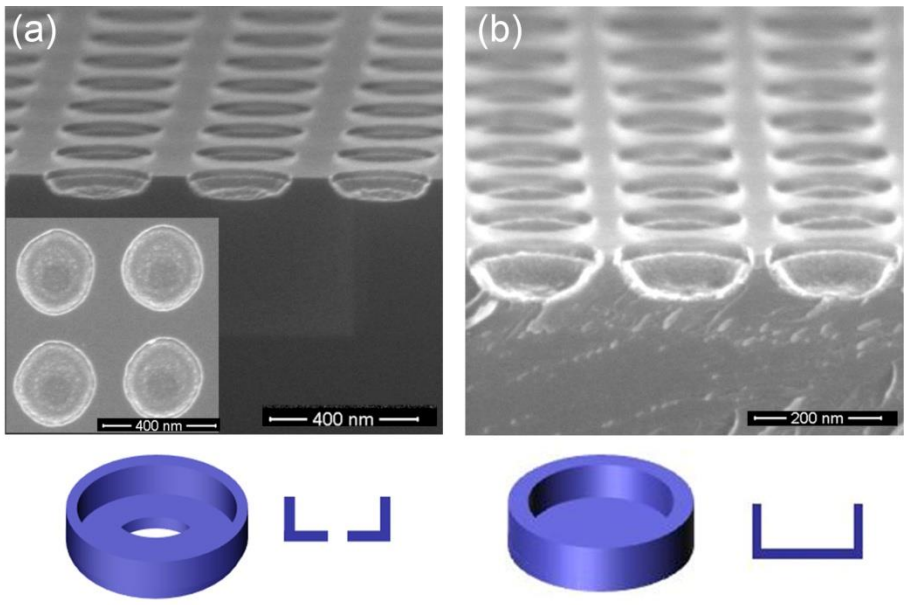

Figure 3.18 SEM micrographs and schematics of (a) perforated nanocups and (b) nanocups.

The magnetization reversal processes were characterized by Lakeshore 7400 Vibrating Sample Magnetometer. Simulations of M-H loops were carried out using the open source code from the Object Oriented MicroMagnetic Framework (OOMMF).

We also tried to measure the M-H loop using the Magneto-Optical Kerr Effect (MOKE) Spectroscopy. However, the signal was very weak as the MOKE signal depends on Kerr rotation in reflected polarized laser from the surface. Unlike thin-film rings, nanoshell arrays have much smaller area ratio of ferromagnetic materials on the sample surface, especially for nanoshells of smaller shell width. Most reflection comes from the silicon substrate, which produces no Kerr effect. Moreover, the periodicity of arrays produces a diffraction effect that further reduces the intensity of the signal.

3.6 Layered NiFe/Au/NiFe Nanoshell Arrays

The synthesis of concentric layered nanoshell array was very similar to that of single-layer nanoshell array. Figure 3.19 illustrates the fabrication process. The same interference lithography, pattern transfer and lift off techniques were employed. In the deposition step, instead of one layer of NiFe, layers of NiFe, Au and NiFe were deposited sequentially with an increase in tilt angle after previous layer. The lift-off process led to array of concentric layered NiFe/Au/NiFe nanoshells. 5nm of Au was deposited by electron beam evaporation as cap layer to prevent oxidation of NiFe.

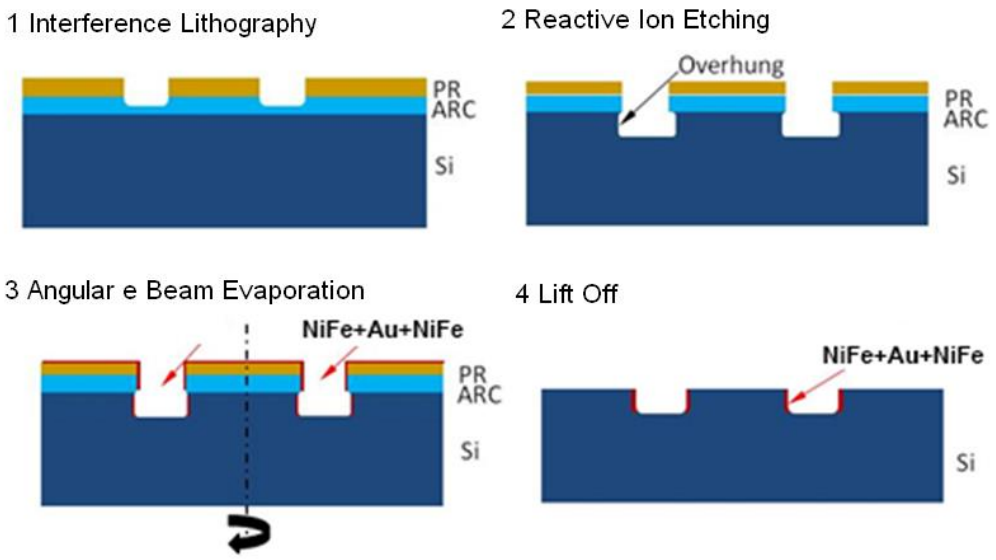

Figure 3.19 Schematic synthesis process of concentric NiFe/Au/NiFe layered nanoshell array.

Large-scale ordered array of concentric layered nanoshells was achieved through this fabrication method, as shown by the scanning electron micrographs in Figure 3.20. Patterned by interference lithography, the diperiodic array was highly ordered with a period of 325 nm. The nanoshells had an average diameter of 200 nm.

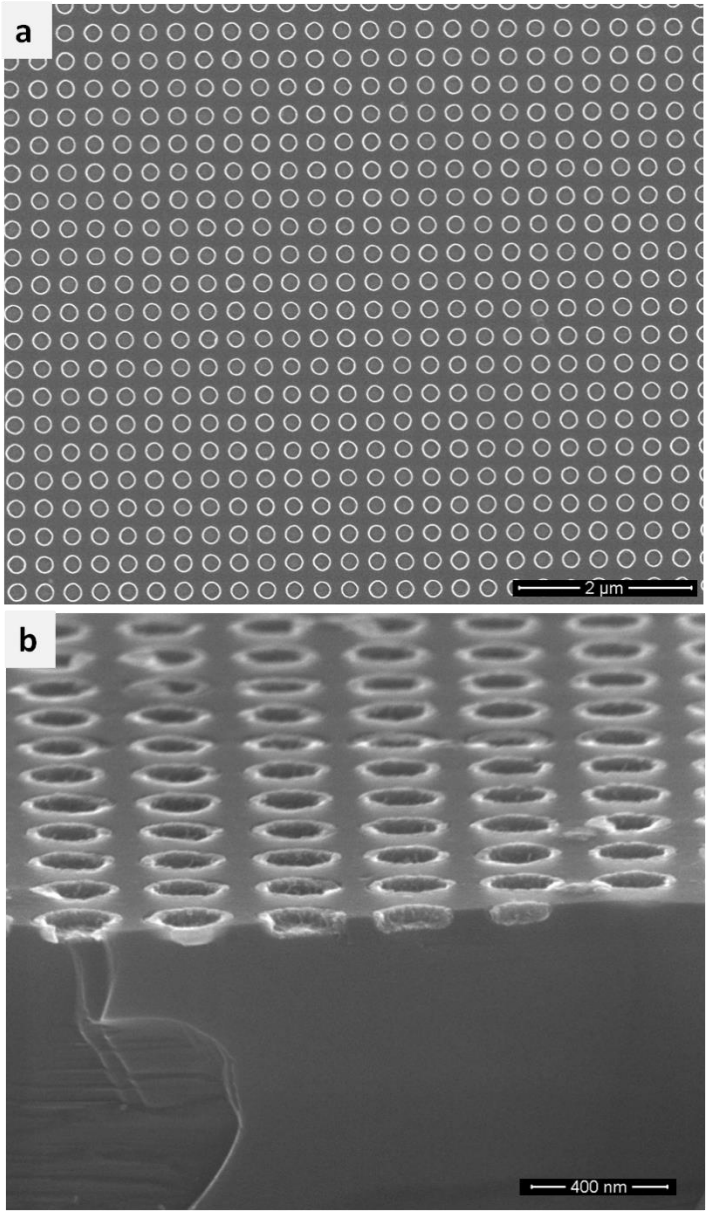

Figure 3.20 Top view (a) and tilted view (b) scanning electron micrographs of concentric layered NiFe/Au/NiFe nanoshell array.

TEM imaging and energy dispersive X-ray spectroscopy (EDX) were carried out to verify the concentric layer structure. The sample was firstly mechanically grinded to a thickness of 40 μm. Subsequently, it was mounted on to a copper ring with epoxy and ion-milled with Ar^+ ion beam in a Gatan precision ion polishing system until the center of the sample was penetrated. The region immediately adjacent to the hole was thin enough to be electron transparent. Bright field imaging and EDX were performed on this region.

Regions with higher atomic number would scatter more electron beam and appeared darker in bright field imaging, giving rise to the mass contrast. Figure 3.21 shows the transmission electron micrograph of a layered nanoshell. Distinct layered structure was observed. The thickness measured agrees with value estimated from reading of crystal microbalance in the evaporator.

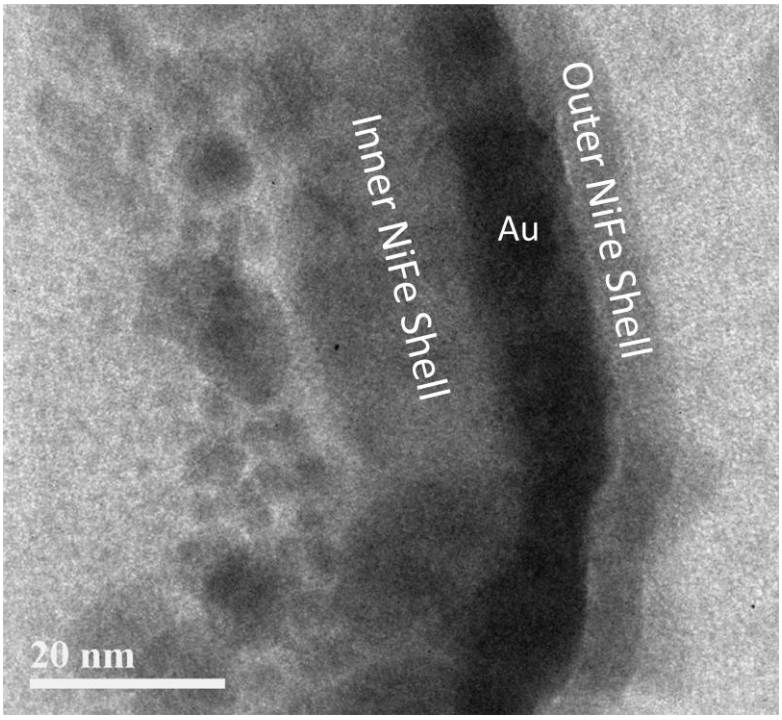

Figure 3.21 Bright field transmission electron micrograph of concentric layered NiFe/Au/NiFe nanoshells.

The NiFe/Au/NiFe layered structure was also examined using EDX, as shown in Figure 3.22. Line scan across the layered structure shows two peaks for Ni and Fe seprated by a Au peak.

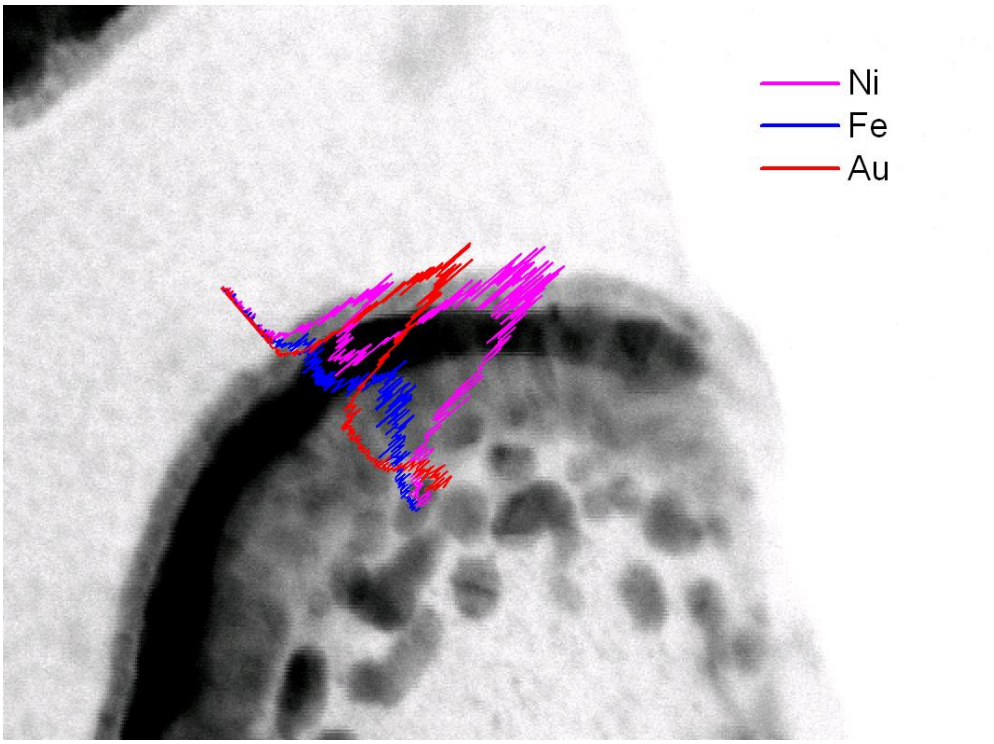

Figure 3.22 EDX line scan across NiFe/Au/NiFe layered shell.

3.7 Characterization techniques

3.7.1 Structure and morphology characterization

The topographies and dimensions of these nanostructures were characterized with Scanning Electron Microscope (SEM) and Transmission Electron Microscope (TEM). A FEI NOVA NanoSEM 230 field emission SEM was used in this work. The imaging was carried out with an electron accelerating voltage of 10-15 kV. Secondary electrons were collected for imaging by a "Through–The-Lens" electron detector in immersion mode. A JEOL-JEM 3010 TEM was used to study the layered NiFe/Au/NiFe nanoshell structure. Bright field imaging was carried out with beam energy of 200keV. The TEM was equipped with an Oxford INCA Energy EDX detector. EDX

mapping and line scan was done with this detector while the TEM was switched to scanning transmission electron microscopy (STEM) mode.

3.7.2 Magnetic characterization

The magnetization reversal processes were characterized using a LakeShore 7404 Vibrating Sample Magnetometer (VSM) and Magneto-Optical Kerr Effect (MOKE) Magnetometry.

Figure 3.23 shows the setup of a Vibrating Sample Magnetometer (VSM). The sample was placed in a uniform magnetic field generated by two electromagnets. The sample holder was vibrated as the field was swept through the designated field range. Stray field from the ferromagnetic nanostructures was detected by the detector coils as induced voltage, which was directly proportional to the sample's magnetic moment. To minimize the effect of noise, ten data points were measured at each field step and an average value was taken.

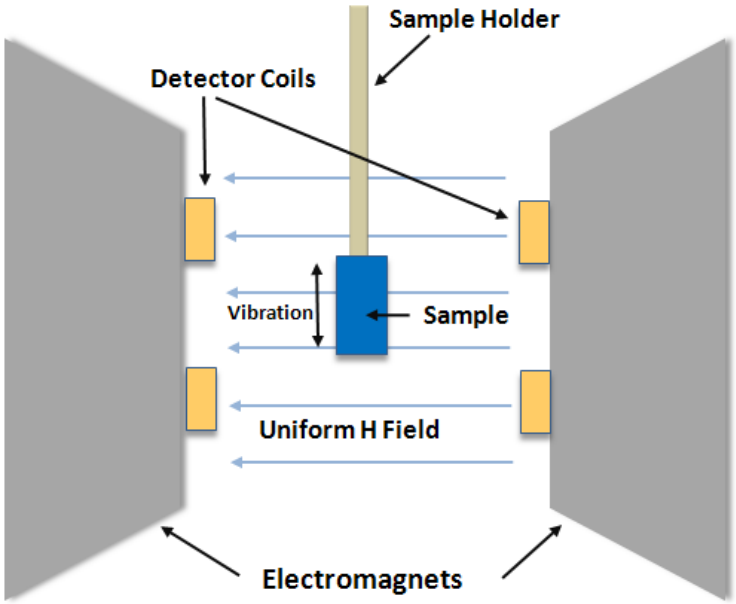

Figure 3.23 Schematics of Vibrating Sample Magnetometer (VSM).

Figure 3.24 shows the schematics of Magneto-Optical Kerr Effect (MOKE) Magnetometer [6]. The sample was loaded in a magnetic field generated by electromagnets and the field was measured using a Gauss probe. A beam of polarized laser with wavelength of 650nm was directed onto the sample surface. Due to stray field on the nanostructure surface, the reflected beam was elliptically polarized. The degree of ellipticity was directly affected by the magnetization state of ferromagnetic structures and measured with an analyzer.

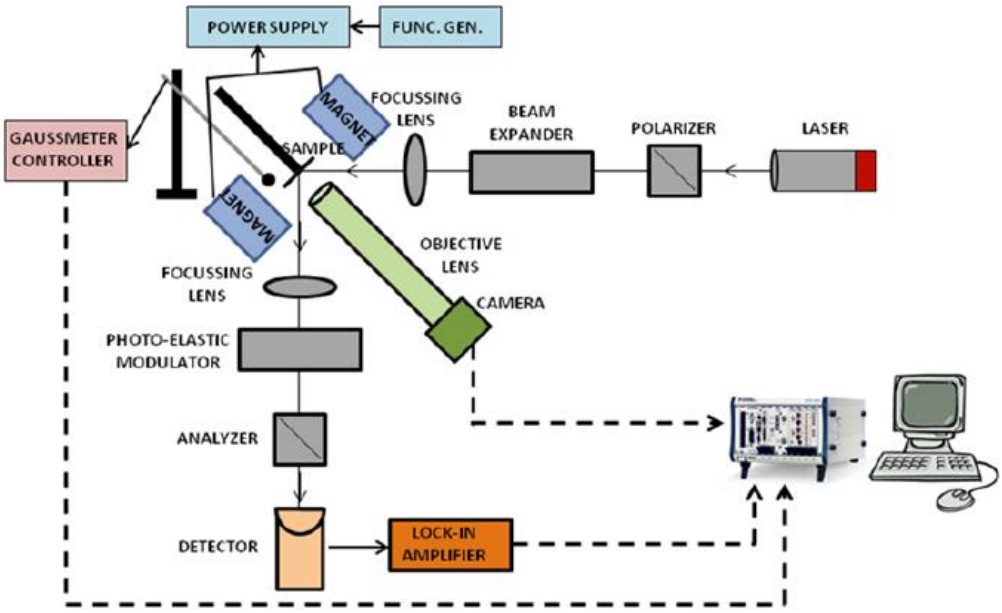

Figure 3.24 Schematic of Magneto-Optical Ker Effect (MOKE) magnetometer [6].

3.8 Micromagnetic simulation

Micromagnetic simulations were performed using the Object Oriented MicroMagnetic Framework (OOMMF) codes from NIST [7]. To simplify the calculation, the nanostructures were assumed to have walls of uniform thickness. Individual nanostructure was simulated instead of arrays to avoid excessively long simulation time. The dimensions used in the simulations

were extracted from SEM micrographs of the nanostructures. The following parameters were used for: NiFe saturation magnetization = 860 emu/cm^3, NiFe exchange constant A = 1.3×10^{-6} erg/cm, and the Gilbert damping parameter was set at 0.5 for rapid convergence. The magnetocrystalline anisotropy was treated as negligible when compared with the shape-induced anisotropy of the nanostructures. The cell size used was $2\times2\times2$ nm^3.

3.9 References

1. Singh, D. K., et al., *Arrays of ultrasmall metal rings.* Nanotechnology, 2008. **19**(24): p. 245305.
2. Plummer, J. D., Deal, M. D., and Griffin, P. B., *Silicon VLSI Technology, Fundamentals, Practice and Modeling*. 2000: Prentice Hall.
3. Jiran, E. and Thompson, C., *Capillary instabilities in thin films.* J. Electron. Mater., 1990. **19**(11): p. 1153.
4. Walsh, M., *On the design of lithographic interferometers and their applications*. 2004, MIT.
5. Wang, Z., Large-area ordered nanoparticle array by templated dewetting, Unpublished work,, 2012.
6. S. Jain, Unpublished work: Developing an Integrated Focused Magneto-Optical Kerr Effect (MOKE) Magnetometer Using NI PXI Hardware and LabVIEW.

7. Donahue, M. J. and Porter, D. G., OOMMF User's Guide, Version 1.0, Interagency Report NISTIR 6376, National Institute of Standards and Technology, Gaithersburg, Sept 2009.

Chapter 4 Large-Area Ferromagnetic Nanodisk and Nanoparticle Arrays

4.1 Introduction

Nanodisk is a relatively simple ferromagnetic nanostructure in geometry. It has been extensively studied in literature for its ease of fabrication [1-3]. Large-area ordered arrays of ferromagnetic nanodisks patterned by interference lithography were reported [4]. In this chapter, we present the magnetic properties of NiFe nanodisk array with a period of 250nm and examine the effect of magnetostatic coupling in the array.

Ordered arrays of Co and CoPt nanoparticles have been demonstrated by solid state dewetting method with topological templates [5, 6]. These nanoparticles were embedded inside array of inverted pyramids in silicon substrate. In this chapter, we also present synthesis and magnetic properties of NiPt and NiFe nanoparticle arrays on top of flat substrate surface prepared by dewetting of nanodisks.

4.2 Magnetization Reversal of Nanodisk Array

Figure 4.1 shows the M-H loop of nanodisk array with a period of 250nm. The nanodisks had an average diameter of 163.6nm and a thickness of 15nm.

Single step switching was observed with a coercivity of 36.5 Oe and remanence of 0.83.

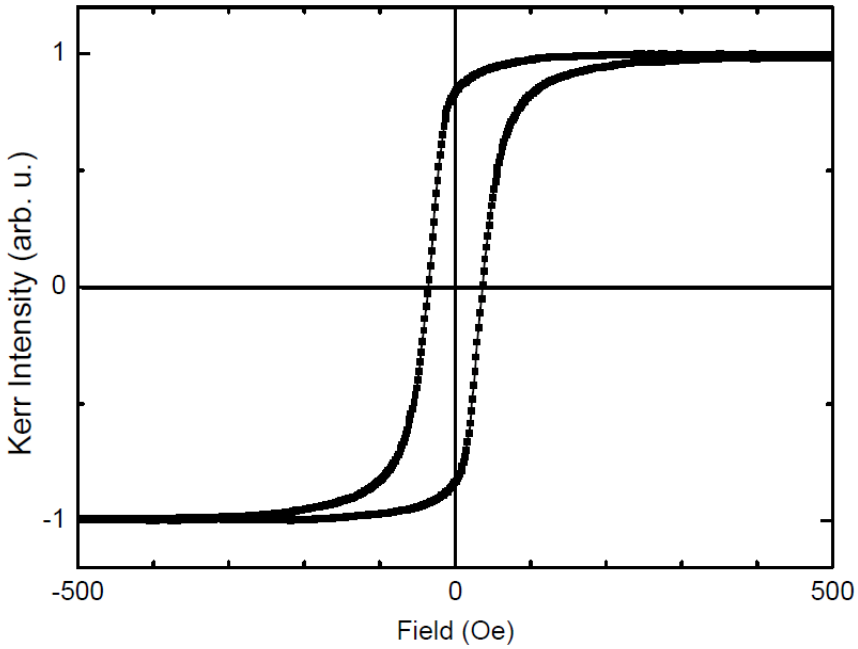

Figure 4.1 In-plane M-H loop of nanodisk array measured by MOKE.

Micromagnetic simulation was performed for single nanodisk with a diameter of 160nm and a thickness of 15nm. The applied field was in plane with the nanodisk. The simulated M-H loop (Figure 4.11 a) showed a two-step switching different from experiment. Figure 4.2(b) shows the magnetization reversal process. When relaxed from high external field along $-x$ direction, the magnetization in the nanodisk retained the single domain state (State i). As the field reversed to $+x$ direction and increased further, the magnetization formed a Vortex (State ii). Next, the Vortex core migrated to the edge and annihilated as the magnetization switched to reverse single domain with moment along $+x$ direction (State iii).

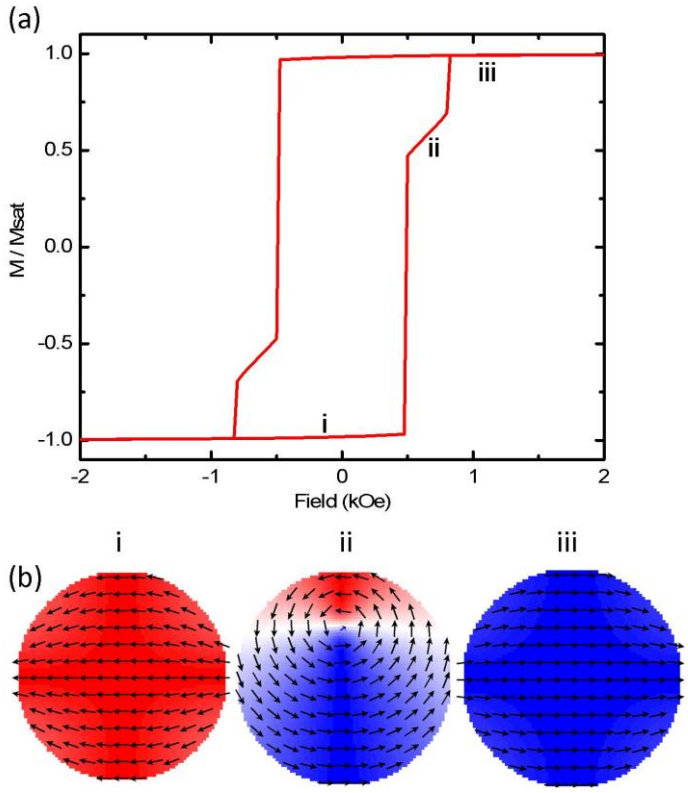

Figure 4.2 Simulated in-plane M-H loop (a) and spin states (b) along the magnetization reversal process for a nanodisk with diameter of 160nm and thickness of 15nm. Cell size used was $2\times2\times5nm^3$.

In previous studies on magnetization switching of ferromagnetic nanodisks, it was reported that the magnetization reversal path was highly dependent on their dimensions [1, 3, 4, 7-11]. With reduced diameter and thickness, the magnetization switched from single domain to reverse single domain without formation of vortex. With larger diameter and thickness, formation of Vortex was observed in hysteresis loop measurement and verified using MFM and Lorentz Microscopy. However, Vortex state was still present in a study reported for supermalloy ($Ni_{80}Fe_{14}Mo_5$) nanodisk array with diameter of 150nm and thickness of 15nm [3]. This discrepancy was likely because the array in their study had a larger period. While for our sample with

higher pattern density, the magnetostatic interaction between neighboring nanodisks can promote direct switching from single domain state to reverse single domain state.

Assuming the nanodisk as a dipole with moment of $V \cdot M_s$, the stray field along the dipole can be calculated with the following equation

$$H_{dipole} = 2\left(\frac{m}{r^3}\right) cos\theta$$

where H_{dipole} is the field from the dipole, m is the moment of the dipole, r is the distance from the center of the disk and θ is the angle with respect to the dipole. At 250nm away, the stray field is

$$H_{dipole} = 2\left(\frac{\pi(80\times10^{-7}cm)^2\times15\times10^{-7}cm\times860emu/cm^3}{(250\times10^{-7}cm)^3}\right) cos0°$$

$$\approx 33.20\ Oe$$

Such field is significant compared to the coercivity of 36.5 Oe measured experimentally. It can lead to correlated magnetization reversal of nanodisks in the array.

OOMMF simulation was performed for a 3×3 nanodisk array with a period of 250nm. Figure 4.3 shows the simulated hysteresis loop and corresponding magnetization states. The simulation results showed that 8 of the 9 nanodisks exhibited one-step single domain to reverse single domain switching path at a low switching field of 25Oe. There was one nanodisk which went through the Vortex state (State ii).

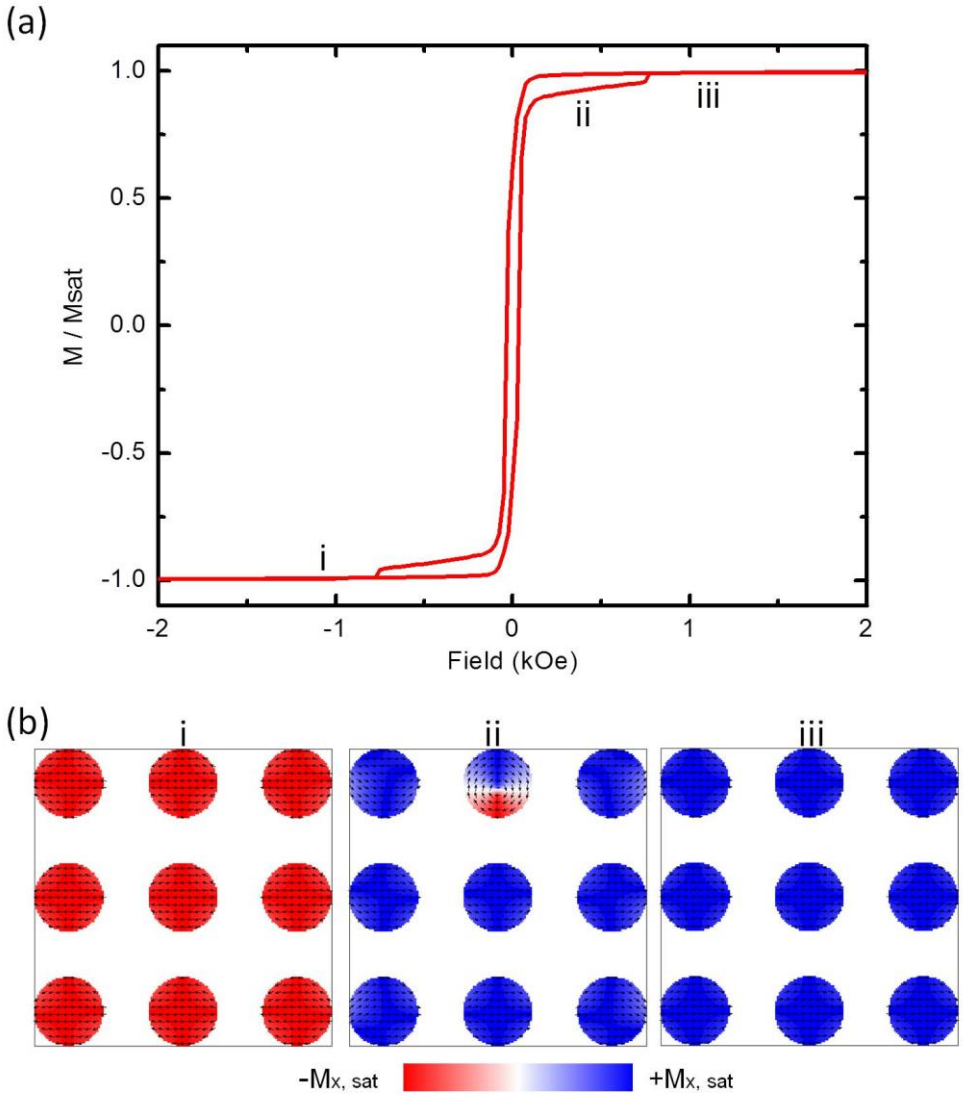

Figure 4.3 Simulated in-plane M-H loop (a) and spin states (b) along the magnetization reversal process for 3×3 nanodisk array with diameter of 160nm, thickness of 15nm and period of 250nm. Cell size used was $2\times2nm^2$ (2D).

Figure 4.4 shows the component of demagnetization and stray field along *x* axis. There was strong stray field of around 800Oe between the neighboring nanodisks. The simulation results suggested that there was magnetostatic coupling between the nanodisks. While simulation of single

nanodisk yielded a switching path with stable Vortex state, the dipolar magnetostatic coupling may lead to correlated switching of the array.

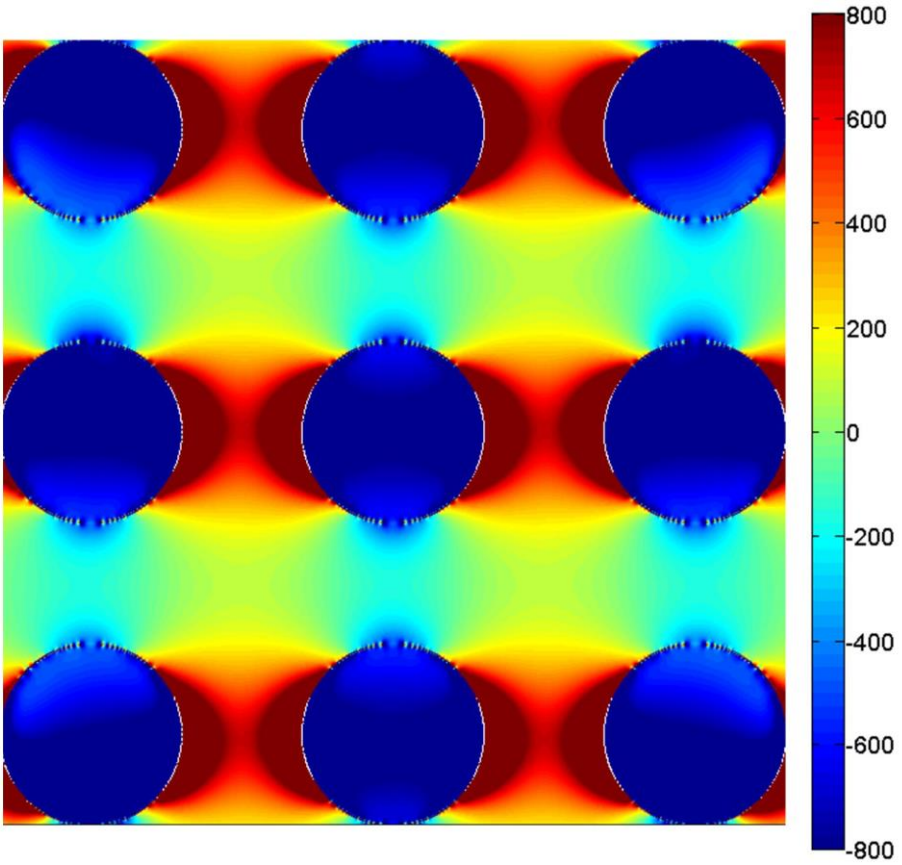

Figure 4.4 Demagnetization and stray field (component along *x* axis) in NiFe nanodisk array at state i with an applied field of +625Oe.

4.3 Magnetization reversal of nanoparticle arrays

4.3.1 NiPt Nanoparticle Array

Figure 4.5 shows the hysteresis loop of a NiPt (Pt 3.2%, atomic) nanoparticle array with an average diameter of 182.3nm and an array period of 330nm. Both in-plane and out-of-plane hysteresis loops had diminished hysteresis with magnetization showing a near linear response with applied

field between saturations. This is similar to some ferromagnetic nanoparticle arrays reported in literature [5, 12, 13].

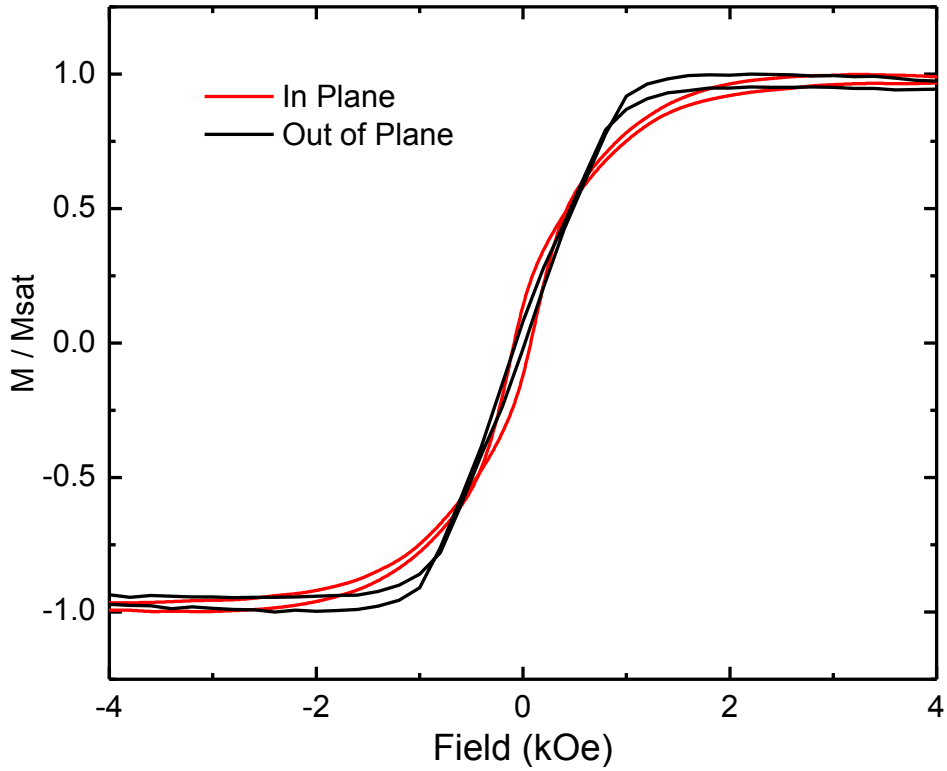

Figure 4.5 Hysteresis loop of NiPt (Pt 3.2%) nanoparticle array measured by VSM (average diameter = 182.3nm and period = 330nm).

4.3.2 NiFe nanoparticle cluster array

Figure 4.6 b shows the EDX spectrum of the center bigger nanoparticle (region A) and one of surrounding smaller nanoparticle (region B), as indicated in Figure 4.6 a. The spectrum is zoomed in to 5 to 10 keV with Kα lines of Ni and Fe in the range. This is to avoid the overshadowing of signal from high L line peak of silicon substrate. It was observed that the center

bigger nanoparticle (Region A) consisted of mainly Ni. In comparison, region B showed only a Fe Kα peak.

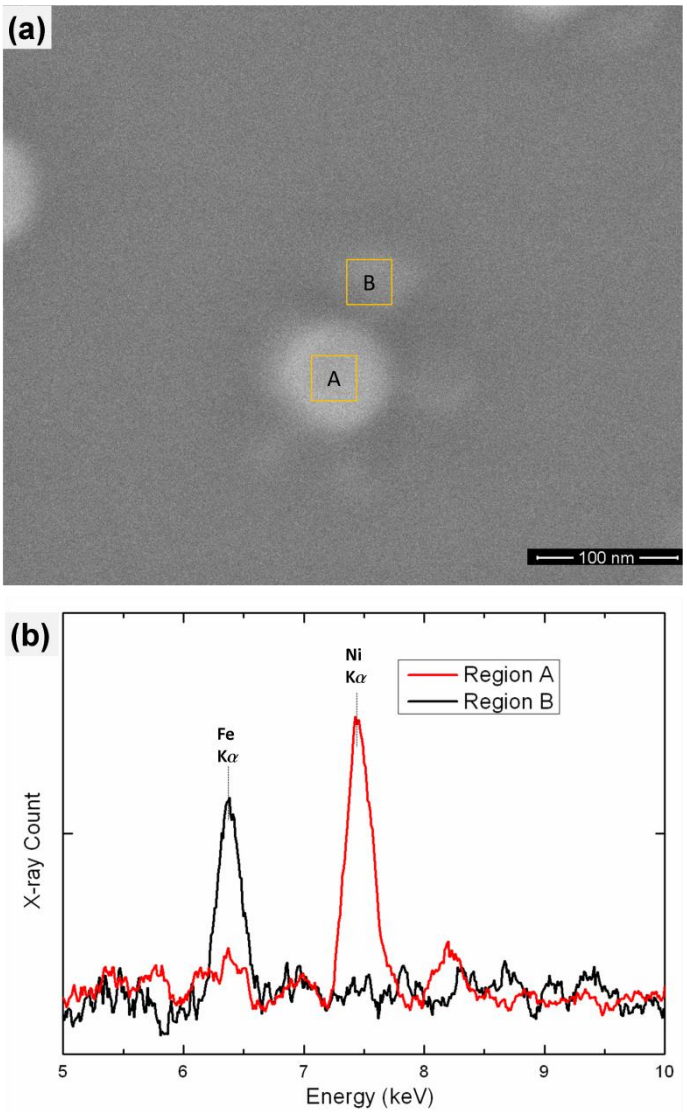

Figure 4.6 (a) SEM of dewetted nanoparticles and (b) EDX spectrum showing Kα peaks of Ni and Fe at sites A and B as indicated in (a).

From the EDX spectrum, it can be concluded that dewetting of single NiFe nanodisk led to a center Ni rich nanoparticle surrounded by smaller nanoparticles rich in consisted of Fe element. X-ray diffraction was performed

to investigate the exact chemical composition. However, the signal was too weak due to limited amount of material on the sample.

The dewetting was carried out in forming gas (N_2, 90% + H_2, 10%) with a high purity of 99.995%. However, in the annealing process, the forming gas was used to flash the furnace tube and there was a continuous supply of impurity. Hence, the small amount of oxygen or water vapor in the forming gas cannot be ignored. In addition, when loading the sample, ambient air was introduced into the furnace. Although the furnace tube was flushed with forming gas, residual of air was likely to be another source of oxygen. Moreover, the surface of NiFe nanodisk may oxidize while exposed to air.

Figure 4.7 shows the Ellingham diagram redrawn showing only iron oxides and water [14]. The reactions relevant to Fe and iron oxides are listed below.

Reaction (1) $\frac{3}{2}Fe + O_2 = \frac{1}{2}Fe_3O_4$

Reaction (2) $2Fe + O_2 = 2FeO$

Reaction (3) $4Fe_3O_4 + O_2 = 6Fe_2O_3$

Reaction (4) $6FeO + O_2 = 2Fe_3O_4$

Below 710 ℃, the H_2O line (red) is below Reaction (3) but above Reactions (1), (2) and (4). H_2 in the forming gas can reduce Fe_2O_3 to Fe_3O_4, but cannot reduce Fe_3O_4 further to FeO or Fe. Formation of Fe_3O_4 is thermodynamically favoured. Above 710 ℃, the line for Reaction (4) is above the H_2O line. Fe_3O_4 can be reduced to FeO by H_2. However, the H_2O line still lies above reaction (2), which means H_2 cannot reduce FeO to elemental Fe.

These iron oxides have high melting temperature. They do not dewet easily like metals such as Au, Ni, Co [5, 15-17].

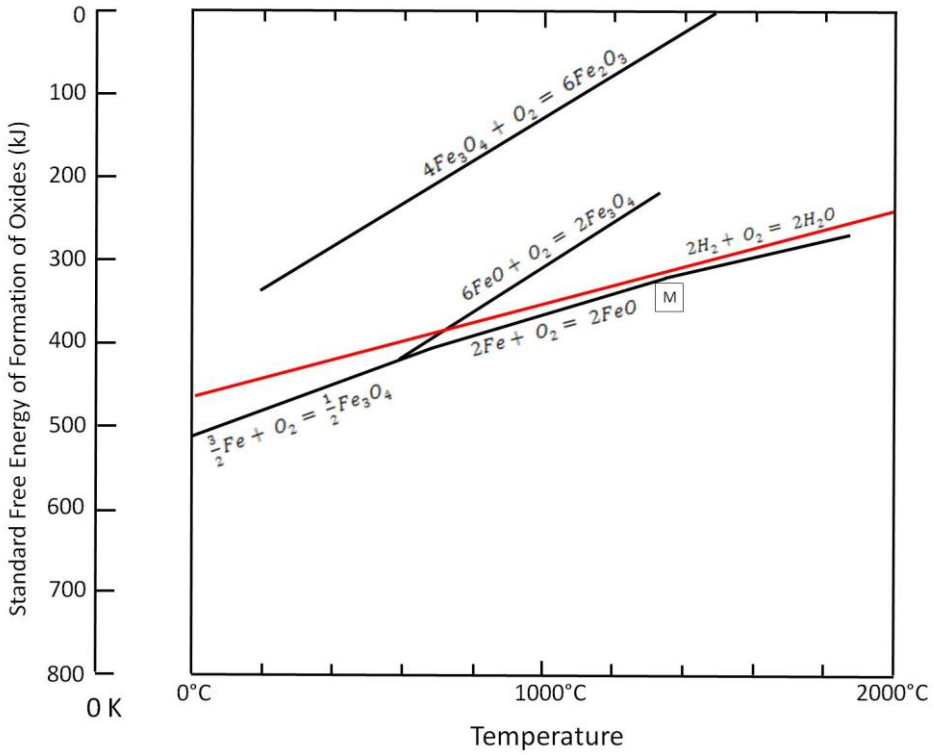

Figure 4.7 Ellingham diagram of selected metals[14].

The in-plane and out-of-plane M-H loops were measured with VSM. Figure 4.8 shows the measured M-H loop for NiFe nanoparticle array dewetted at 800 ℃ for 3 hours. Both in-plane and out-of-plane M-H loops had diminished hysteresis with magnetization showing a near linear response with applied field between saturations. This is similar to the NiPt nanoparticle presented earlier in this chapter.

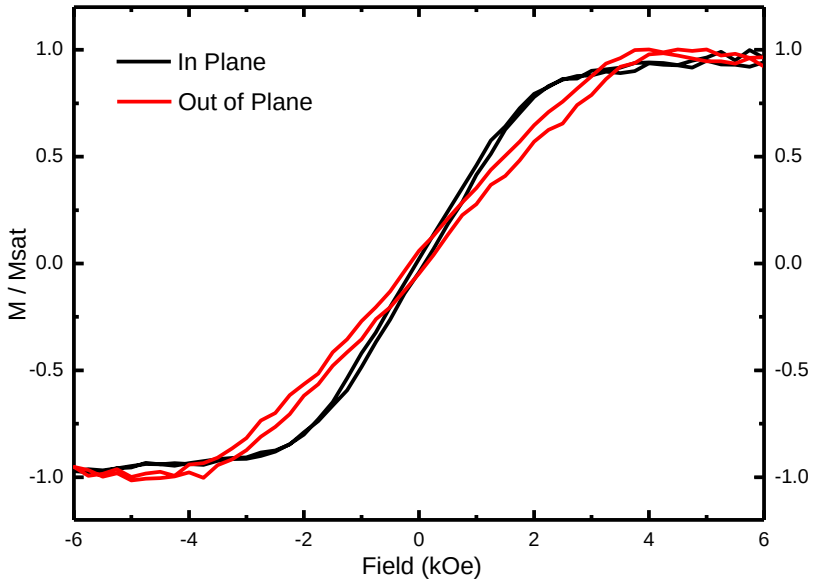

Figure 4.8 Hysteresis loop of NiFe nanoparticle array measured by VSM.

4.4 Conclusion

To conclude, we have demonstrated a large-scale synthesis method for ordered array of nanodisks and nanoparticles with period down to 250nm. With diameter around 160nm, thickness of 15nm and period of 250nm, the nanodisk array exhibited a single domain switching through rotation of moments. The discrepancy with literature was ascribed to increased magnetostatic coupling effect in our array with a shorter period [3, 11]. Dewetting of NiFe nanodisk led to split nanoparticle cluster consisting of a Ni-rich nanoparticle surrounded by multiple smaller iron oxide nanoparticles due to oxidation of Fe.

4.5 References

1. Shinjo, T., et al., *Magnetic Vortex Core Observation in Circular Dots of Permalloy.* Science, 2000. **289**(5481): p. 930.

2. Lebib, A., et al., *Size and thickness dependencies of magnetization reversal in Co dot arrays.* J. Appl. Phys., 2001. **89**(7): p. 3892.

3. Cowburn, R. P., et al., *Single-Domain Circular Nanomagnets.* Phys. Rev. Lett., 1999. **83**(5): p. 1042.

4. Fernandez, A., et al., *Magnetic force microscopy of single-domain cobalt dots patterned using interference lithography.* IEEE Trans. Magn., 1996. **32**(5): p. 4472.

5. Oh, Y.-J., et al., *Cobalt Nanoparticle Arrays made by Templated Solid-State Dewetting.* Small, 2009. **5**(7): p. 860.

6. Thompson, C. V., *Solid-State Dewetting of Thin Films.* Ann. Rev. Mater. Res., 2012. **42**(1): p. 399.

7. Guslienko, K. Y., et al., *Field evolution of magnetic vortex state in ferromagnetic disks.* App. Phys. Lett., 2001. **78**(24): p. 3848.

8. Schneider, M., Hoffmann, H., and Zweck, J., *Lorentz microscopy of circular ferromagnetic permalloy nanodisks.* App. Phys. Lett., 2000. **77**(18): p. 2909.

9. Panchumarthy, R., et al., *Magnetic State Estimator to Characterize the Magnetic States of Nano-Magnetic Disks.* IEEE Trans. Magn., 2013. **49**(7): p. 3545.

10. Raabe, J., et al., *Magnetization pattern of ferromagnetic nanodisks.* J. Appl. Phys., 2000. **88**(7): p. 4437.

11. Rahm, M., et al., *Vortex nucleation in submicrometer ferromagnetic disks.* App. Phys. Lett., 2003. **82**(23): p. 4110.

12. Tiberto, P., et al., *Morphology and magnetic properties of island-like Co and Ni films obtained by de-wetting.* J. Nanopar. Res., 2011. **13**(1): p. 245.

13. Singamaneni, S., et al., *Magnetic nanoparticles: recent advances in synthesis, self-assembly and applications.* J. Mater. Chem., 2011. **21**(42): p. 16819.

14. Mitchell, B. S., *An Introduction to Materials Engineering and Science for Chemical and Materials Engineers*. 2004.

15. Giermann, A. L. and Thompson, C. V., *Solid-state dewetting for ordered arrays of crystallographically oriented metal particles.* App. Phys. Lett., 2005. **86**(12): p. 121903.

16. Kim, D., Giermann, A. L., and Thompson, C. V., *Solid-state dewetting of patterned thin films.* App. Phys. Lett., 2009. **95**(25): p. 251903.

17. Ye, J. and Thompson, C. V., *Templated Solid-State Dewetting to Controllably Produce Complex Patterns.* Adv. Mater., 2011. **23**(13): p. 1567.

Chapter 5 Cylindrical NiFe Nanoshell and Nanocup Arrays

5.1 Introduction

Nanoshell structure has intermediate height to width aspect ratio. It is analogous to a transitional geometry between thin-film ring and nanotube. Although ferromagnetic thin-film ring and nanotube have been extensively studied, magnetism in ferromagnetic nanoshell structure has not been fully investigated. Nanocup and perforated nanocup represent a nanoshell structure with fully covered disk-shape base or partially covered ring-shape base. Ferromagnetic nanocup and perforated nanocup have not been reported in literature to the author's knowledge. In this chapter, the effects of dimension and geometry of $Ni_{80}Fe_{20}$ (NiFe) nanoshell, nanocup and perforated nanocup structure on their magnetization switching process are discussed through experiments and micromagnetic simulations. Also, we present our study on the domain wall spin configuration and stray field of these nanomagnets.

5.2 Magnetization reversal of NiFe nanoshell array

5.2.1 Effect of shell width

Figure 5.1 shows the measured and simulated in-plane M-H loops for nanoshells with shell width (w) of 8 nm (Figure 5.1 a and b), 18 nm (Figure

5.1 c and d) and 25 nm (Figure 5.1 e and f). It can be seen that there is a good qualitative agreement between experiments and simulations on the effect of shell width on magnetization switching of nanoshells.

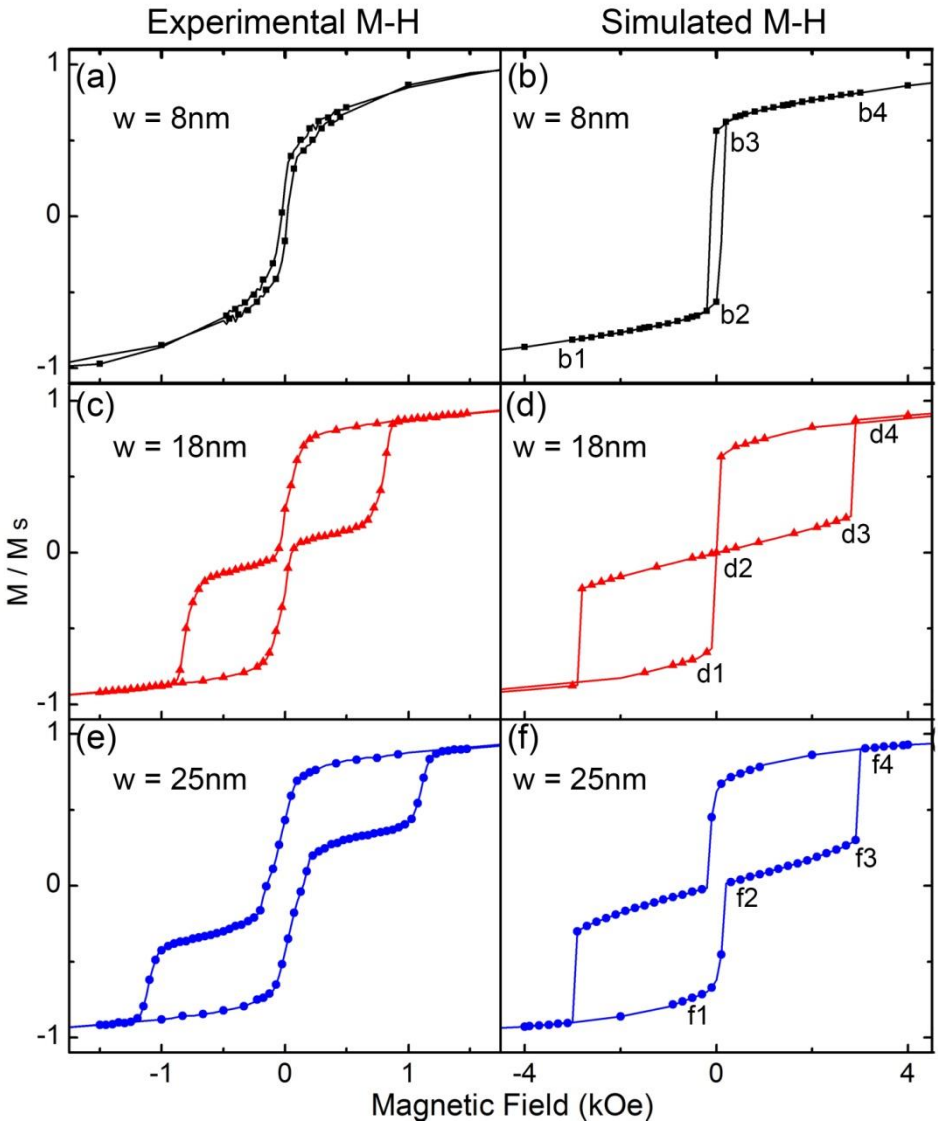

Figure 5.1 Experimental M-H loops (a, c, e) and simulated M-H loops (b, d, f) of nanoshell with w equals to (a, b) 8 nm, (c, d) 18 nm, and (e, f) 25nm.

Figure 5.2 a, b and c are the simulated magnetic configurations for nanoshells with shell width of 8nm, 18nm and 25nm at the corresponding fields shown in Figure 5.1 b, d and f. These nanoshells had an average

diameter of 196 nm with a standard deviation of 5.7 nm. The height was approximately 40 nm and the period was 250 nm.

Two-step switching was observed for thicker nanoshells with shell widths of 18 nm and 25 nm. Figure 5.2 b and c show the magnetization reversal process which corresponded to the Onion-Vortex-Reverse Onion switching path similar to those of thin-film ferromagnetic nanorings [1], although the height/width ratio of the nanoshells is much higher compared to nanorings. In the Onion-Vortex transition (d1-d2 and f1-f2), simulations showed that the head-head and tail-tail domain walls depinned, moved towards each other and annihilated to form a flux closure Vortex state. The Vortex state was stable over a range of magnetic field (d2-d3 and f2-f3). As field increases further, the Vortex to Reverse Onion transition occurred (d3-d4 and f3-f4) when a reverse domain nucleated and reversed the magnetization in half of the shell to form the Reverse Onion state.

In comparison, the nanoshell array with a shell width of 8nm showed a single-step switching process at b2-b3 corresponding to the Onion-Reverse Onion transition with a much narrower hysteresis loop. No Vortex state stability range was observed in the experiment or simulation.

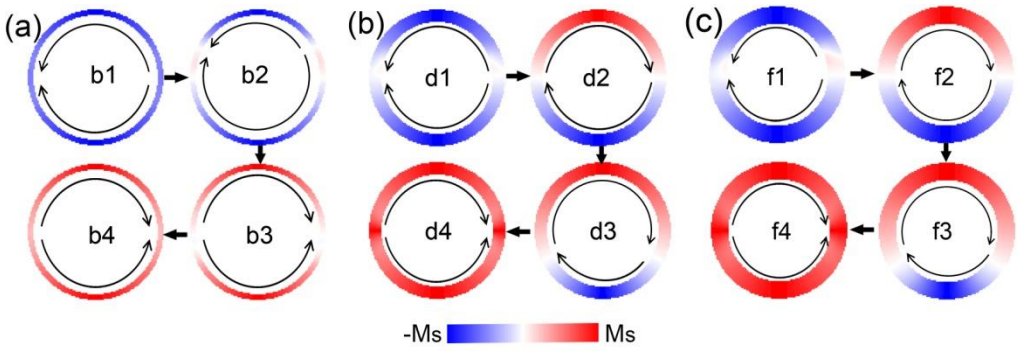

Figure 5.2 Simulated magnetic configurations during magnetization reversal process for nanoshells with w equals to (a) 8 nm, (c) 18 nm, and (e) 25nm at field designated in Figure 5.1. The color code in (c f i) represents the horizontal component of the magnetization. Cell size used was 2×2×4nm3.

Similar single-step switching has been reported in a theoretical study for Fe nanoshells [2]. Torres-Heredia *et. al.* simulated hysteresis loops of Fe "nanorings" with an outer diameter of 80, with varying height/thickness from 20 to 200 nm and an internal diameter from 0 to 72 nm. As the height/width ratio increased, they also observed disappearance of Vortex state in the simulation. Experimental studies of nanotubes of cobalt and nickel also showed a single-step switching in the direction perpendicular to the nanotube [3-5].

The competition of exchange, demagnetization and Zeeman energies associated with the ferromagnetic structure under an external magnetic field determines its magnetization reversal process. Figure 5.3 shows the simulated M-H loop for nanoshell with shell width of 8nm and 25nm. For nanoshells with a shell width of 25 nm, the exchange and demagnetization energies dropped at remanence. Energy valleys appeared as the Vortex state formed. For nanoshells with shell width of 8 nm, there were no such energy valleys and the Vortex state was absent.

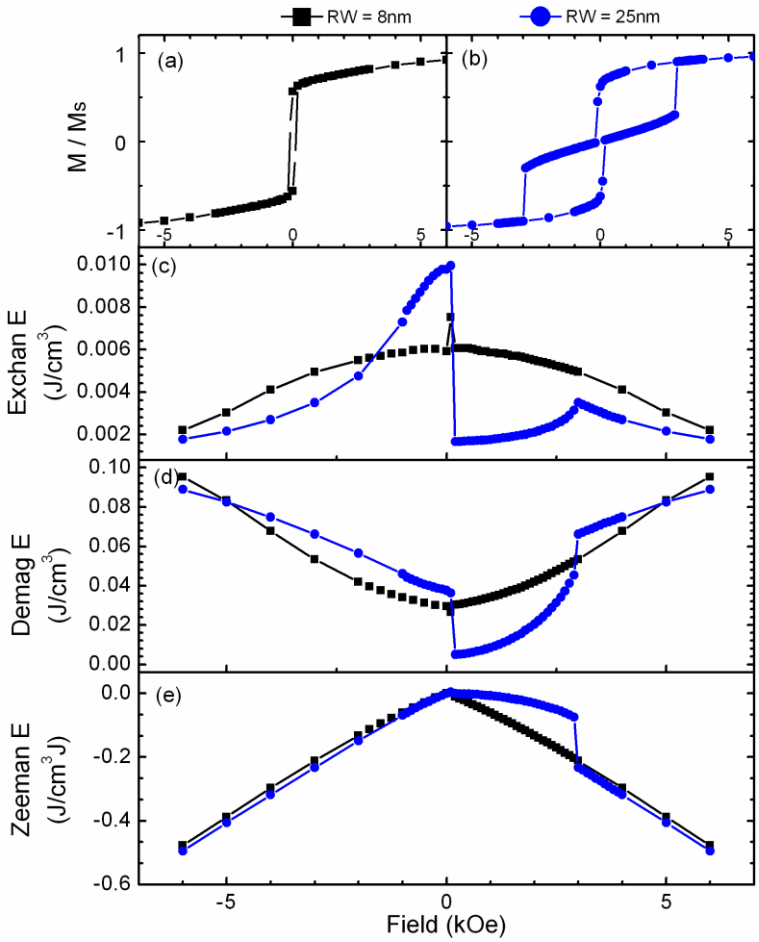

Figure 5.3 Simulated in-plane hysteresis loops ((a) and (b)), exchange energy (c), demagnetization energy (d) and Zeeman energy (e) for a nanoshell with w = 8nm (black square) and 25 nm (blue circle), a diameter of 200 nm and a height of 40 nm.

5.2.2 Spin configurations at domain walls

The magnetic configuration of the domain walls in nanoshells, and the nearest-neighbor magnetostatic interactions, are important in understanding the switching behavior of the arrays. Domain wall phase diagrams for nanorings in the onion state with varying height and width have been plotted for NiFe [6] and Co [7]. Transverse domain walls with in-plane moment rotation are expected in nanorings with smaller height and width. However, the nanoshells have height/width ratio > 1. Therefore, due to shape anisotropy,

it is likely that the transverse component of the transverse domain wall will be oriented along the out-of-plane *h* direction, not radially along *w*.

Figure 5.4 b and c show the *y*-*z* plane views of the simulated domain wall in a nanoshell with shell width of 8 nm at cross sections indicated in Figure 5.4 a, confirming that the moments in the center of the transverse domain wall point out of plane. The cylindrical nanoshell can be viewed as a rolled-up thin film strip containing two transverse domain walls [8]. A similar domain wall structure was reported in a Monte Carlo simulation for nanorings with ring *d* = 70 nm, *w* = 7 nm and *h* = 10 nm [9].

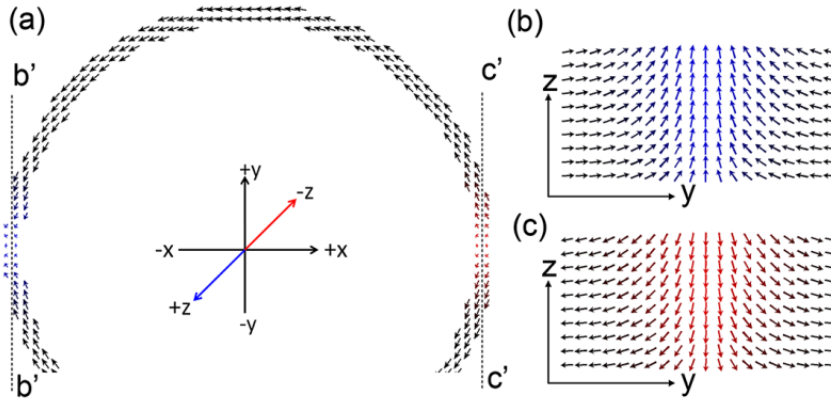

Figure 5.4 Spin configuration of a nanoshell with shell width of 8 nm, *d* of 200 nm and *h* of 40 nm (a) top view, (b) y-z plane view at cross section b'-b', (c) y-z plane view at cross section c'-c'.

5.2.3 Stray field near domain wall in nanoshells

This domain wall configuration yielded a lower in-plane stray field but a higher out-of-plane stray field as shown in Figure 5.5 a and b. For nanoshells with shell width of 18 nm and 25 nm, the moments in the center of transverse domain wall still pointed in the *h* direction. However, the component in the *x*-*y* plane increased.

Figure 5.5 b shows the in-plane magnitude $(H_x^2+H_y^2)^{0.5}$ of the simulated stray field around a domain wall in a NiFe ring with d = 200 nm, w = 8 nm, and h = 40 nm. The stray field 50 nm away from the domain wall in the $-x$ direction was calculated as 164 Oe. Such a field is significant compared to the switching field. It would lead to stabilization of parallel O-states and correlated reversal of the nanoshell arrays.

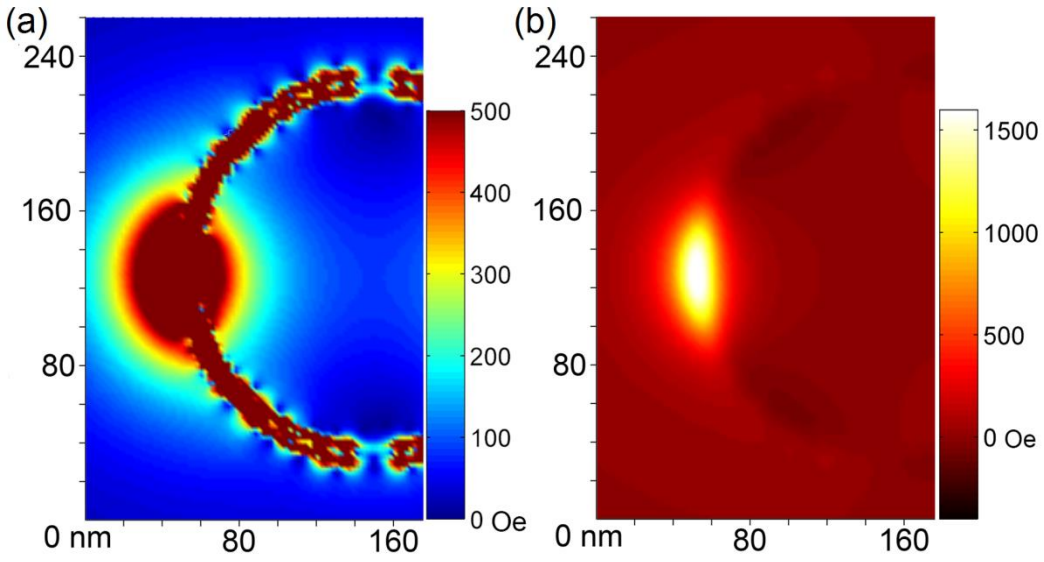

Figure 5.5 (a) Calculated in-plane root mean square magnitude in the x-y plane of the stray field around a domain wall at half of the shell height. (b) Calculated out-of-plane stray field around a domain wall at a height of 10 nm above the shell.

5.2.4 Effect of structural asymmetry

The effect of structural asymmetry was also investigated using micromagnetic simulations. Figure 5.6 shows M-H loops of a nanoshell with a diameter of 200 nm, and height of 40 nm but inhomogeneous shell width varying from 6 nm to 10 nm. The asymmetric nanoshell exhibited two-step switching via the Onion-Vortex-Reverse Onion states, with field applied either along x direction or y direction, as shown in Figure 5.6. In comparison,

symmetric nanoshell of the same size exhibited the Onion-Reverse Onion switching as observed both in experiments and simulations. The narrower region of the shell acted as a domain wall pinning site in the O-state, breaking the symmetry between the two walls. Domain wall pinning due to structural asymmetry or defects facilitates the formation of a V-state with a specific chirality [10-12].

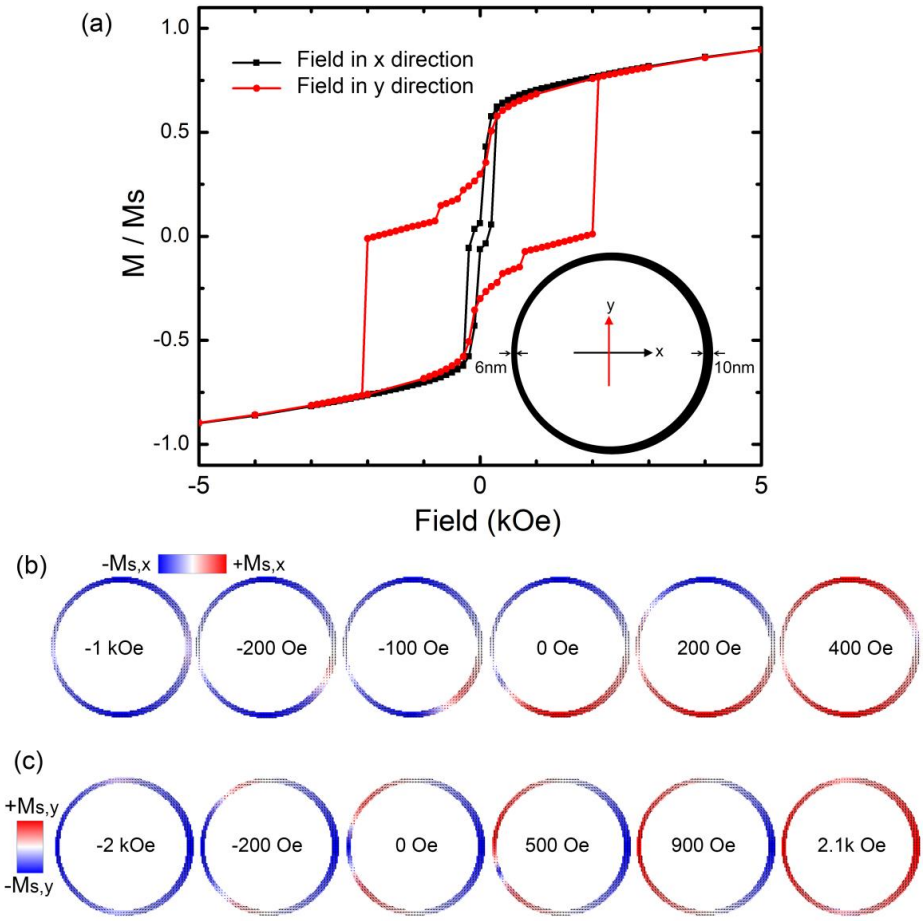

Figure 5.6 (a) Simulated in-plane hysteresis loops for a nanoshell with asymmetric width as shown in the inset for field applied in x direction (black) and y direction (red); the diameter and height of nanoshell is 200 nm and 40 nm, respectively. (b) Evolution of magnetization states with field applied in x direction, along symmetry axis. (c) Evolution of magnetization states with field applied in y direction.

5.2.5 Magnetization reversal of nanoshell at low temperature

Figure 5.7 shows the M-H loops of nanoshell arrays with 18nm shell width measured at 100k, 200k and room temperature by VSM. As the low temperature VSM measurement required smaller sample size because of geometry constraint induced by the cooling chamber, the measurement was subjected to a relatively higher noise/signal ratio. Nonetheless, we observed temperature dependence of switching field. When cooled down to 200k, the switching field from Vortex state to Onion stage did not change much compared with that measured at room temperature. However, when cooled down to 100k, it was observed that the Vortex-Onion switching field increased significantly. This could be explained by reduction in thermal excitations at lower temperature. Nucleation of reverse domain, depinning and propagation of domain walls are essential processes during the Vortex-Onion switching in a ferromagnetic nanorings or nanoshell. These processes are subjected to energy barriers. At lower temperature, there was less thermal excitation to overcome energy barriers. With lower thermal excitations, a higher field would be required to form reverse domain and commence the switching, as observed in the experiment. Moreover, domain walls were often pinned at local defects. With lower excitations at low temperature, a higher field is also required to overcome these energy barriers resulting in a longer switching process, or decreased slope in the M-H loop. Similar observations have been reported in Co nanorings with sub-micron diameter [13, 14].

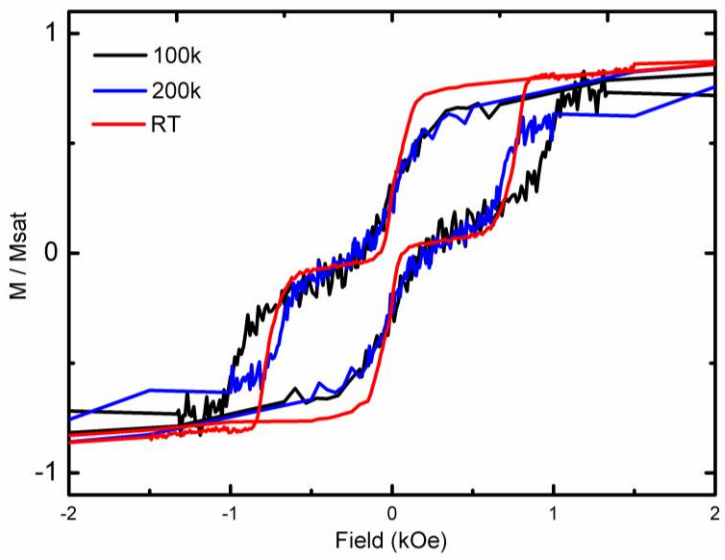

Figure 5.7 M-H loops of nanoshell array with of width of 18nm measured at 100K, 200K and room temperature.

5.3 Magnetization reversal of $Ni_{80}Fe_{20}$ perforated nanocup and nanocup arrays

The perforated nanocup exhibited a four-step switching process, as shown in Figure 5.8 a and b. The structure can be considered as having two regions: a top cylindrical shell and a bottom thin film ring. Figure 5.8 e-i show the magnetization evolution of the top and bottom regions. The reversal started with an overall Onion-state when relaxed from in-plane saturation as shown in Figure 5.8 e. At remanence, the two domain walls depinned but did not annihilate to form a vortex state. Instead, the two domain walls formed a 360 ° domain wall in the shell region, while a transverse domain wall was formed in the ring region as shown in Figure 5.8 f. The junction between the bottom ring and top shell regions acted as a barrier for magnetization rotation. Hence domain wall annihilation was inhibited. As the field increased, Vortex state formed in both ring and bottom regions (Figure 5.8 g). At 800 Oe (Figure 5.8

h), the shell region retained a V-state but two domains formed in the ring region, and a small part of the ring at the edge had its magnetization anti-parallel to the applied field due to exchange coupling with the shell region. The two domains in the ring were separated by a VW. When the field was increased further in the $+x$ direction, Reverse Onion state formed throughout the structure, as shown in Figure 5.8 i.

In contrast, the nanocup structure showed a two-step switching, as shown in Figure 5.8 c and d. The structure can be considered as two regions: a top cylindrical shell and a bottom thin film circular disk. After relaxation from in-plane saturation, the shell region was in an Onion state, while in the disk region the moments aligned along the $-x$ direction except the edge part (Figure 5.8 j). At -100 Oe, the shell switched into a V-state, while a vortex also nucleated in the disk, as depicted in Figure 5.8 k. As the field increased along the $+x$ direction, the two domain walls in the shell depinned and moved toward each other. At the same time, the vortex core in the disk migrated toward one side of the disk and more of the moment of the disk aligned with the external field, as shown in Figure 5.8 l and m. Finally, the two domain walls in the top shell region annihilated each other, while the vortex in the bottom disk annihilated at the edge as shown in Figure 5.8 n.

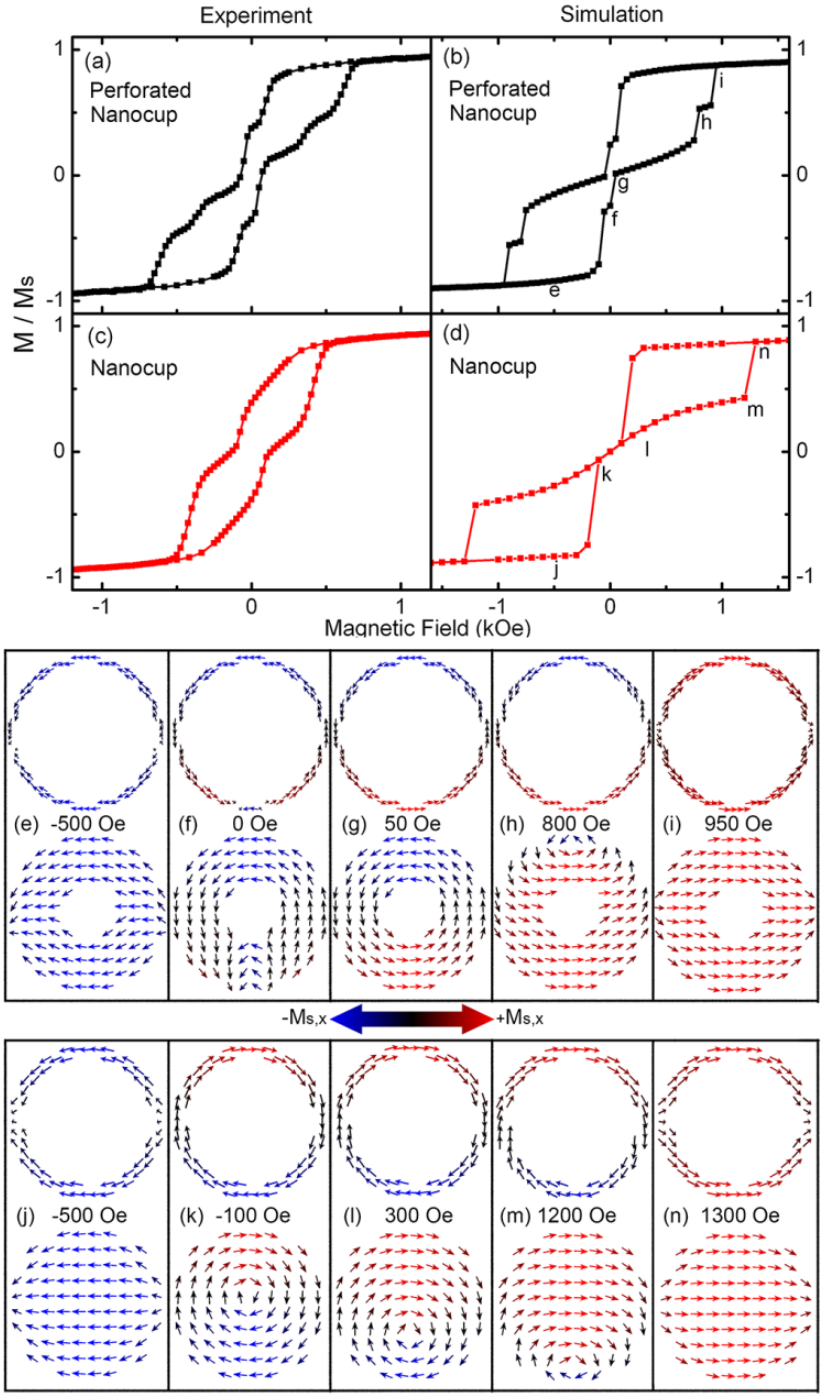

Figure 5.8 Experimental M-H loops and simulated M-H loops for the perforated nanocup (a) (b) and the nanocup (c) (d). (e)-(i) and (j)-(n) show the simulated magnetization states of the top and bottom regions for a perforated nanocup and for a nanocup, respectively, at the designated fields. The color code in (e-n) represents the horizontal component of the magnetization.

5.4 Conclusion

In conclusion, we have demonstrated a permalloy nanoshell/nanocup array fabrication method patterned using interference lithography and angular deposition. The maskless and parallel nature of this nanofabrication process enables high-throughput low-cost large-scale nanostructure array fabrication. The process is highly versatile to control the shape and dimension of nanomagnets with nanoshell, perforated nanocup and nanocup arrays demonstrated.

Varying shell width down to sub 10 nm was achieved and we show that with fixed diameter and height, the shell width has determining effect on its magnetization reversal process. Ultrathin shell width and high height/width ratio lead to an out-of-plane domain wall spin configuration at Onion state and minimized crosstalk between neighboring nanorings. $Ni_{80}Fe_{20}$ nanocup array exhibit a 2-step Onion-Vortex-Reverse Onion switching, while the perforated nanocup array shows a 4-step switching process with two additional intermediate states.

5.5 References

1. Zhu, J. G., Zheng, Y., and Prinz, G. A., *Ultrahigh density vertical magnetoresistive random access memory (invited).* J. Appl. Phys., 2000. **87**(9): p. 6668.
2. Torres-Heredia, J. J., López-Urías, F., and Muñoz-Sandoval, E., *Micromagnetic simulation of iron nanorings.* J. Magn. Magn. Mater., 2005. **294**(2): p. e1.

3. Li, D. D., et al., *Template-based Synthesis and Magnetic Properties of Cobalt Nanotube Arrays.* Adv. Mater., 2008. **20**(23): p. 4575.

4. Han, X. F., et al., *Structural and Magnetic Properties of Various Ferromagnetic Nanotubes.* Adv. Mater., 2009. **21**(45): p. 4619.

5. Daub, M., et al., *Ferromagnetic nanotubes by atomic layer deposition in anodic alumina membranes.* J. Appl. Phys., 2007. **101**(9): p. 09J111.

6. Laufenberg, M., et al., *Observation of thermally activated domain wall transformations.* Appl. Phys. Lett., 2006. **88**(5): p. 052507.

7. Klaui, M., et al., *Head-to-head domain-wall phase diagram in mesoscopic ring magnets.* Appl. Phys. Lett., 2004. **85**(23): p. 5637.

8. McMichael, R. D. and Donahue, M. J., *Head to head domain wall structures in thin magnetic strips.* IEEE Trans. Magn., 1997. **33**(5): p. 4167.

9. Zhang, W. and Haas, S., *Phase diagram of magnetization reversal processes in nanorings.* Phys. Rev. B, 2010. **81**(6): p. 064433.

10. Zhu, F. Q., et al., *Magnetic Bistability and Controllable Reversal of Asymmetric Ferromagnetic Nanorings.* Phys. Rev. Lett., 2006. **96**(2): p. 027205.

11. Wang, X. H., Peng, W. K., and Lew, W. S., *Flux-closure chirality control and domain wall trapping in asymmetric magnetic ring.* J. Appl. Phys., 2009. **106**(4): p. 043905.

12. Giesen, F., et al., *Vortex circulation control in large arrays of asymmetric magnetic rings.* Phys. Rev. B, 2007. **75**(18): p. 184428.

13. Tripathy, D., et al., *Controlling the magnetization reversal in exchange-biased Co/CoO elongated nanorings.* Nanotechnology, 2009. **20**(1): p. 015304.

14. Kläui, M., et al., *Switching processes and switching reproducibility in ferromagnetic ring structures.* Appl. Phys. Lett., 2004. **84**(6): p. 951.

Chapter 6 Concentrically Layered Cylindrical NiFe/Au/NiFe Nanoshells

6.1 Introduction

Understanding of interlayer magnetic coupling is important in the design of novel spin transport systems. Although there have been several studies on interlayer magnetic coupling in pseudo-spin-valve nanorings reported, these studies focused on vertically stacked ring structures [1-9]. Laterally layered structures, especially those with submicron dimension, have not been well studied [10]. In this chapter, we present the magnetic properties of a novel concentrically layered NiFe/Au/NiFe nanoshell structure with various shell width configurations. Interlayer magnetic coupling are investigated through micromagnetic simulations and experiments.

In layered thin films consisting of ferromagnetic layers separated by atomic layers of non-magnetic spacers, indirect exchange coupling [11] is dominant in determining the overall magnetization of the stacked films. Direct exchange coupling[12] can also happen if pinholes are present. As the spacer gets thicker than a few nanometers, indirect and direct exchange coupling effect decrease quickly; magnetostatic coupling due to stray field from domain

walls [12-14] and Néel coupling [15] due to interfacial roughness become stronger.

In previous studies on vertically stacked ellipsoidal, rhombic and circular rings, the coupling mechanism studied focused on domain wall induced magnetostatic coupling [5-8, 16]. These ring structures were vertically stacked NiFe/Cu/Co rings with the thickness of Cu spacer in the range of 4 to 6 nm. The Co and NiFe layers were assumed to be exchange decoupled with a Cu spacer of such thickness. The stray field from the domain walls in the hard Co layer strongly affected the magnetization reversal process of soft NiFe layer. The magnetization reversal processes of NiFe ring can be qualitatively different compared to a single layer NiFe ring.

Nonetheless, magnetic coupling in laterally layered structures, especially those with submicron dimensions, have not been well studied [10]. In Chapter 5, we reported magnetic properties of large-area NiFe nanoshells arrays [17]. The nanoshells exhibited an Onion (*O*) – Vortex (*V*) - Reverse Onion (*RO*) switching path for thicker shell width (*w*), while an *O-RO* switching without going through Vortex was favored with a shell *w* of 8nm. In this Chapter, we investigate the effect of interlayer magnetic coupling on the magnetization switching of a novel concentrically layered NiFe/Au/NiFe nanoshell structure with different shell width configurations.

Interlayer coupling through non-magnetic spacer is critical in determining the overall magnetic properties in layered ferromagnetic structures. The

possible magnetic coupling mechanisms in the NiFe/Au/NiFe layered nanoshell include magnetostatic coupling at domain walls and edges of nanoshells, interfacial roughness induced Néel coupling and pinhole induced direct exchange coupling. With thickness of spacer above 3nm, the indirect Ruderman-Kittel-Kasuya-Yosida (RKKY) exchange coupling is expected to be weak [18]. The RKKY coupling effect varies in sign and amplitude as a function of spacer thickness. The coupling strength can be attenuated by the thickness fluctuation due to roughness of the Au spacer attenuates. In the layered NiFe/Au/NiFe nanoshell with Au spacer of 3nm and above investigated here, the RKKY coupling is assumed to be negligible compared to the other coupling mechanisms.

6.2 Experimental hysteresis loops

Figure 6.1 shows the hysteresis loops of layered nanoshell arrays with Au spacer thickness of 3nm, 12nm and 16nm measured using VSM. The outer and inner NiFe shell widths were 8nm and 16nm, respectively. The height was around 45nm. The purple line is the first order derivative of half hysteresis loop as the field was swept from negative to positive. The dotted line shows hysteresis loop of single-layer NiFe nanoshell array with a shell width of 25nm.

The layered nanoshell arrays with Au spacer of 12nm and 16nm had a three-step switching. In comparison, the layered nanoshell array with a 3nm

spacer exhibited a two-step switching path similar to single-layer NiFe nanoshell array with a shell width of 25nm. The hysteresis loop followed closely with that of single-layer NiFe nanoshell. This suggested the moment in the outer and inner NiFe nanoshells was strongly coupled though the 3nm Au spacer. With thickness of 3nm, the Au spacer may not be a continuous film and pinholes were present. Direct exchange coupling can occur at such defect sites [12].

Compared to the 25nm single-layer NiFe nanoshell, the NiFe(8nm)/Au(3nm)/NiFe(16nm) layered nanoshell experienced a longer *V-RO* switching manifested by a decreased slope in the M-H loop and higher field to complete the switching, as shown in Figure 6.1 highlighted by the red circle. During the *V-RO* switching, the reverse domain nucleated and grew with domain wall propagation. The longer switching process can be attributed to a wider distribution of switching fields among the individual layered nanoshells in the array.

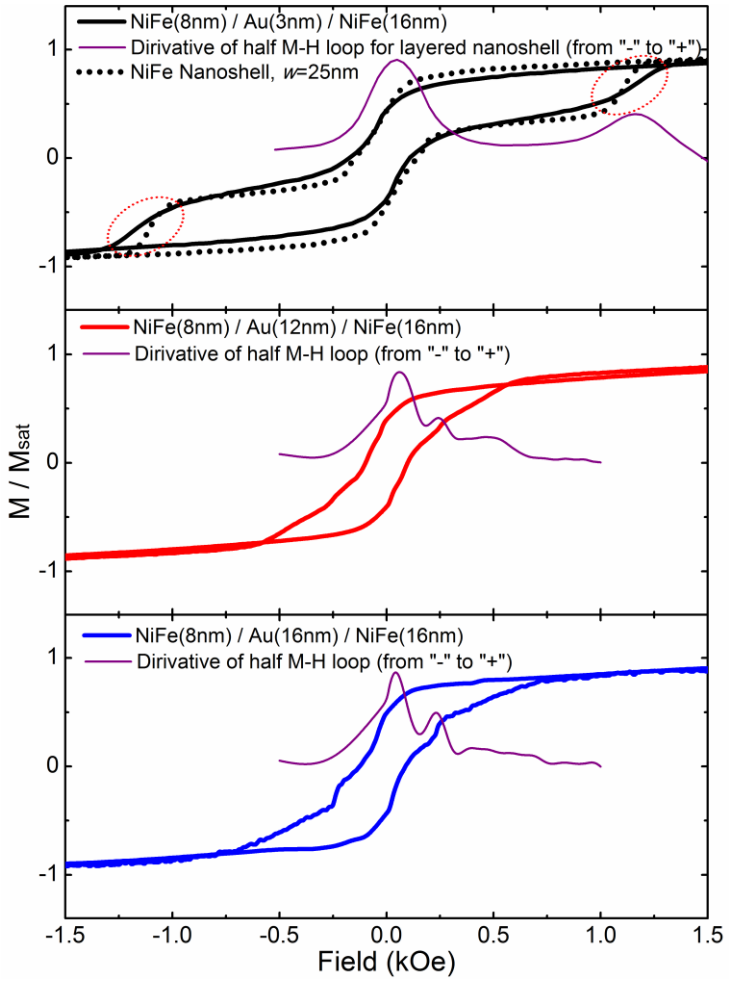

Figure 6.1 Experimental hysteresis loops of layered NiFe(8nm)/Au/NiFe(16nm) nanoshell arrays with Au spacer layers of 3, 12 and 16 nm, respectively.

MOKE signal for flat NiFe thin films with thickness of 8nm and 16nm and layered NiFe(8nm)/Au/NiFe(16nm) thin films with 8nm and 16nm Au spacer were measured as the control sample to examine the interlayer coupling in stacked blanket thin films. However, as shown in Figure 6.2, the 8nm and 16nm NiFe thin films had very close switching field. Hence, the coupling with an Au spacer was hard to deduce from these results.

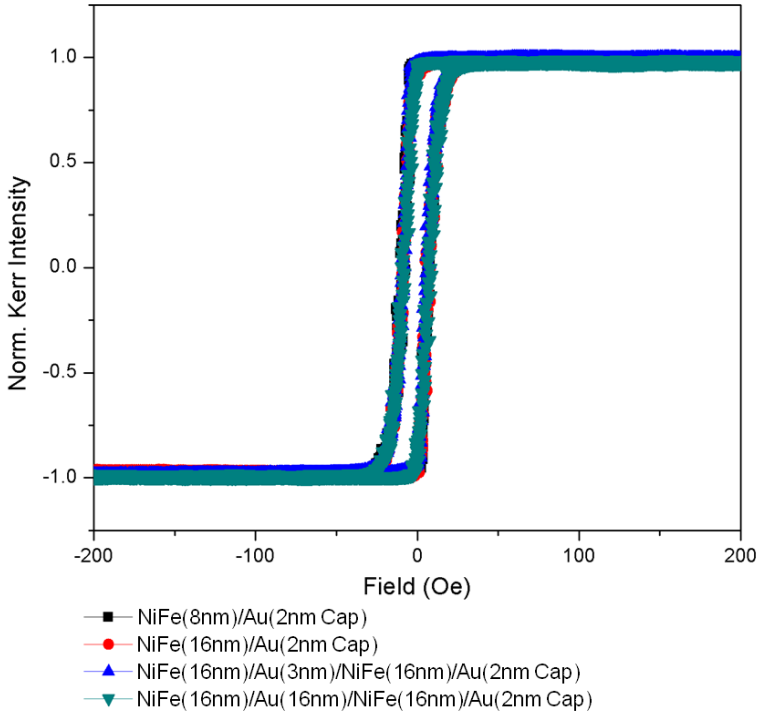

Figure 6.2 In-plane MOKE for flat NiFe films (8nm, 16nm) and layered NiFe(8nm)/Au/NiFe(16nm) flat films with 8nm and 16nm Au spacer.

6.3 Magnetostatic coupling at domain walls

With a thicker Au spacer of 12 and 16 nm, the hysteresis loops measured using VSM showed the layered nanoshells exhibited a three-step switching process, as shown in Figure 6.1. Figure 6.3(a) shows the simulated hysteresis loop of NiFe(8nm)/Au(16nm)/NiFe(16nm) layered nanoshell and single-layer NiFe nanoshells with identical dimension to the inner and outer nanoshells. Figure 6.3(b)-(d) depicts the exchange, demagnetization and Zeeman energies as the field was swept from negative to positive. With a three-step switching path, the simulated hysteresis loop of layered

NiFe(8nm)/Au(16nm)/NiFe(16nm) nanoshell agreed qualitatively with experimentally measured hysteresis.

The single layer NiFe nanoshell structures with dimensions identical to inner and outer nanoshell were also simulated, as shown in Figure 6.4 (b), (c) and Figure 6.4 (b), (c). *O-V-RO* two-step switching was observed for shell width of 16nm, while *O-RO* single-step switching was observed for shell width of 8nm. This agreed with the previous results presented in Chapter 5.

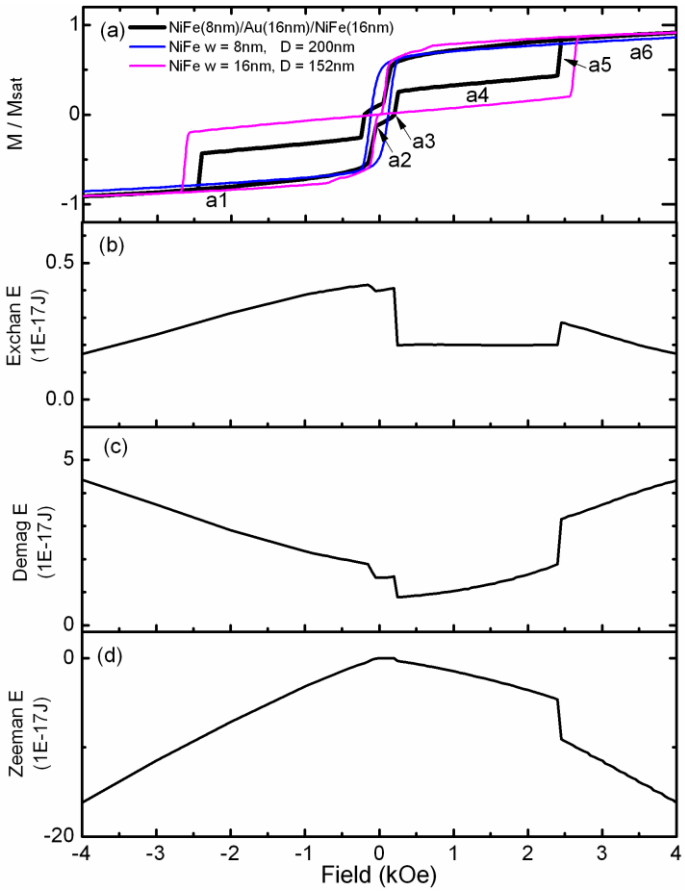

Figure 6.3 Simulated hysteresis loop (a), exchange energy (b), demagnetization energy (c) and Zeeman energy (d) of NiFe(8nm)/ Au(16nm)/NiFe(16nm) layered nanoshell. The blue and magenta lines are simulated hysteresis loops of single layer NiFe nanoshells with identical dimension to the outer and inner nanoshells.

The simulated spin states along the magnetization reversal process of NiFe(8nm)/Au(16nm)/NiFe(16nm) layered nanoshell and single layer nanoshell equivalent to inner and outer nanoshell are depicted in Figure 6.4. The detailed switching process is discussed below.

- State a1: Subjected to high field along the $-x$ direction, both outer and inner NiFe nanoshells were in Onion state with head-to-head and tail-to-tail domain walls.
- State a2: As the applied field was switched to be along the $+x$ direction, the outer NiFe nanoshell switched to Reverse Onion state. This was driven by a decrease in exchange energy and demagnetization energy as shown in Figure 6.3 (b) and (c). This switching behavior was similar to a single-layer NiFe nanoshell with 8nm shell in Figure 6.4(c). At the same time, the inner NiFe nanoshell retained its Onion state. However, due to the external applied field, the domain wall depinned and migrated along the shell to minimize Zeeman energy. The magnetization transformed to a rotated Onion state. The outer NiFe nanoshell in Reverse Onion state also rotated with the inner NiFe nanoshell. An alignment of domain walls between inner and outer nanoshells was observed. This was due to the effect of magnetostatic coupling at the domain walls which will be discussed later in this session.

- State a3: The inner Onion rotated further as field increased to minimize Zeeman energy; the magnetization of outer NiFe nanoshell in Reverse Onion closely followed the rotation due to magnetostatic coupling.
- State a4: The inner NiFe nanoshell switched to Vortex state favored by reduction in exchange and demagnetization energy as shown in Figure 6.3 (b) and (c). The outer NiFe nanoshell restored its magnetization to Reverse Onion state without rotation.
- State a5: As field increased to 2.4 kOe, a reverse domain nucleated in the inner NiFe nanoshell driven by reduction in Zeeman energy as shown in Figure 6.3 (d); the outer NiFe nanoshell remained in Reverse Onion state.
- State a6: To further reduce Zeeman energy, the reverse domain in inner NiFe nanoshell grew larger through domain wall propagation. Finally the magnetization was switched to Reverse Onion state.

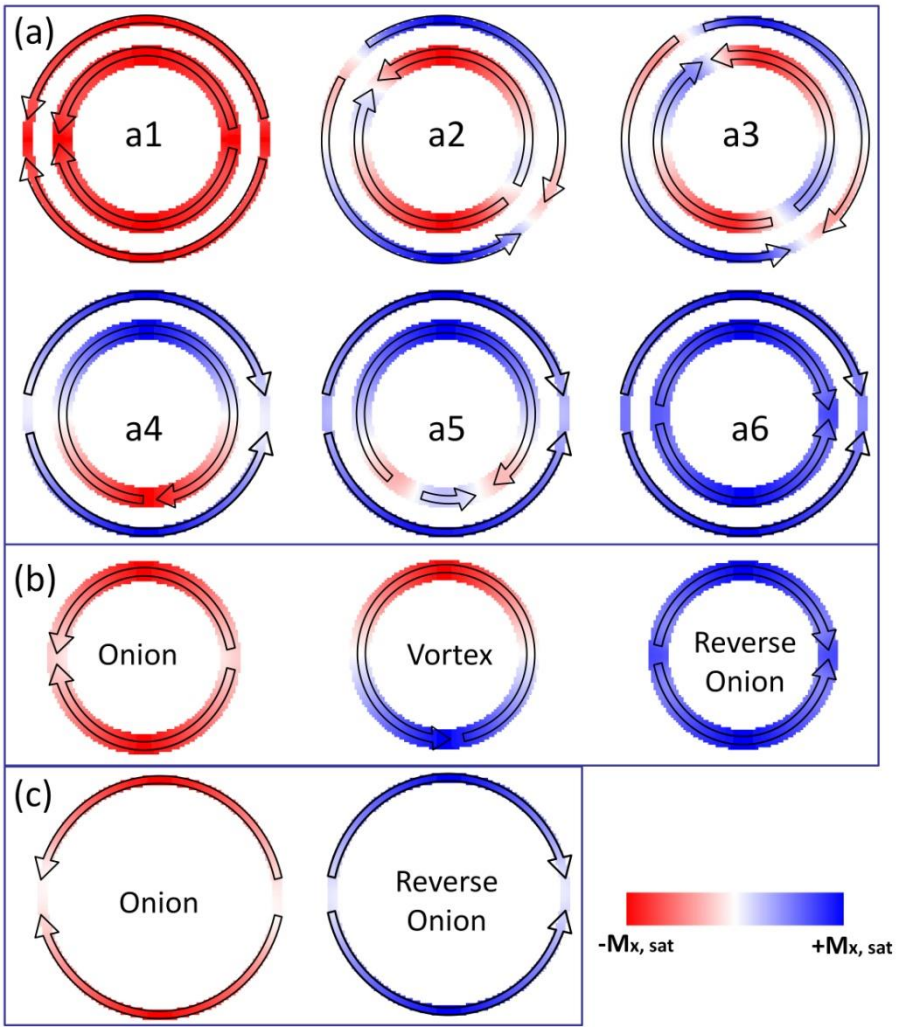

Figure 6.4 Simulated spin states of NiFe(8nm)/Au(16nm)/NiFe(16nm) layered nanoshell (a) at field indicated in Figure 6.3 and single layer NiFe nanoshell with dimension identical to inner (b) and outer (c) nanoshells.

The magnitude ($(H_x{}^2 + H_y{}^2)^{1/2}$) of in-plane demagnetization/stray field was extracted from OOMMF simulation. Figure 6.5 shows the demagnetization field color map around the NiFe(8nm)/Au(16nm)/NiFe(16nm) layered nanoshell at state a3 and state a4 at half height of shell. At state a3, strong in-plane stray field around 3 kOe was observed in the Au spacer at two regions near the domain walls. This field gave rise to magnetostatic coupling

between the domain walls in outer and inner NiFe nanoshells, hence coupling the magnetization of these two NiFe nanoshells at their bidomain (Onion/Reverse Onion state) states. As a result of this coupling effect, when the magnetization in inner NiFe nanoshell at Onion state rotated under external field, the magnetization in outer NiFe nanoshell in Reverse Onion state followed the rotation.

At state a4, the inner NiFe nanoshell switched to Vortex state. The domain walls annihilated and the magnetization formed a flux closure minimizing the stray field. The outer NiFe nanoshell restored its Reverse Onion state with the two domain walls aligned along the *x* axis. The in-plane stray field in the Au spacer decreased significantly, as shown in Figure 6.5(b). It can be concluded that the strong stray field in state a3 is originated from the domain walls in the inner NiFe nanoshell at Onion state, instead of from the outer nanoshell.

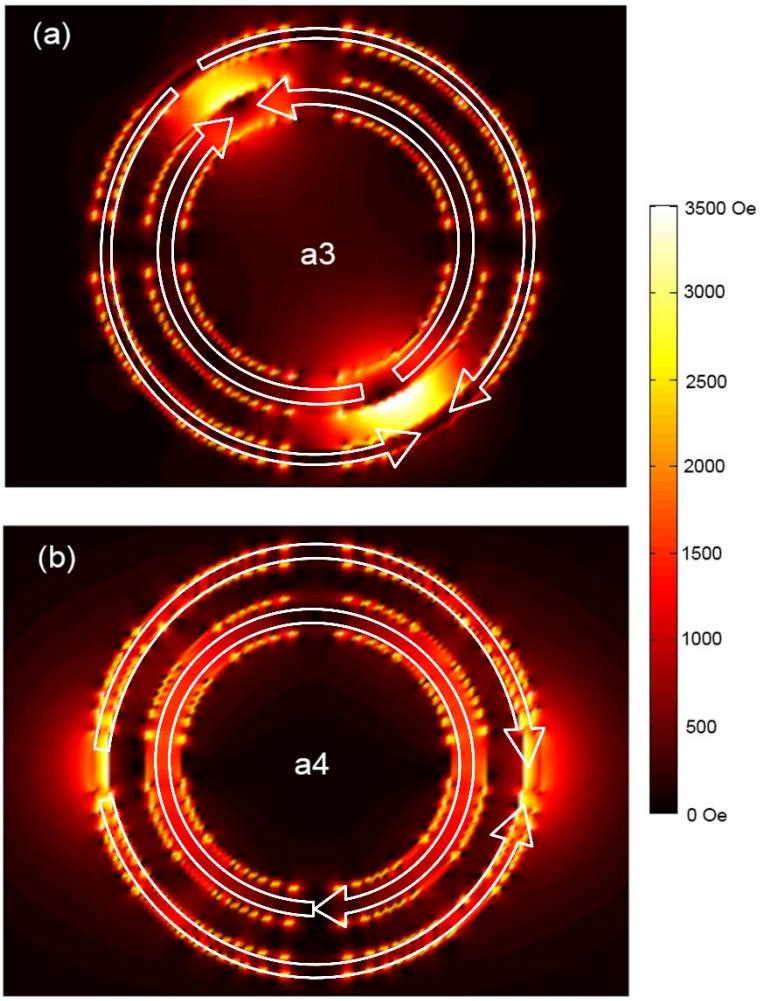

Figure 6.5 Color map of in-plane demagnetization and stray field ($(H_x{}^2 + H_y{}^2)^{1/2}$) of NiFe(8nm)/Au(16nm)/NiFe(16nm) layered nanoshell at state a3 (a) and state a4 (b).The white arrows depict the magnetization states.

Domain wall spin configuration is important in determining the stray field around ferromagnetic nanostructures. Figure 6.6 (a) and (b) show the *x*-*y* plane view of spin configuration at one of the two domain walls in the NiFe(8nm)/Au(16nm)/NiFe(16nm) layered nanoshell at state a3 and state a4, respectively. The inset shows the *y*-*z* cross-sectional view of spin

configurations along the dash line. The length of arrow is proportional to the component of moments in the respective plane.

At state a3, there was more in-plane moment at the domain wall in the inner NiFe nanoshell. This was the origin of large in-plane stray field in the Au spacer as shown in Figure 6.5 (a), which led to the magnetostatic coupling between outer and inner NiFe nanoshells.

In comparison, moment around the domain wall in outer NiFe nanoshell preferred to be aligned out of plane due to shape anisotropy. This was similar to the domain wall spin configuration of single-layer nanoshell with shell width of 8nm as discussed in Chapter 5. In addition, the total moment in the outer NiFe nanoshell was much smaller because of smaller volume of material. As a result, the in-plane stray field at state a4 was much smaller as shown in Figure 6.5. Hence, the inner NiFe nanoshell could stay in Vortex without being switched under the stray field from the outer NiFe nanoshell until the external field was high enough to initiate the nucleation of reverse domain as shown in Figure 6.4 (e).

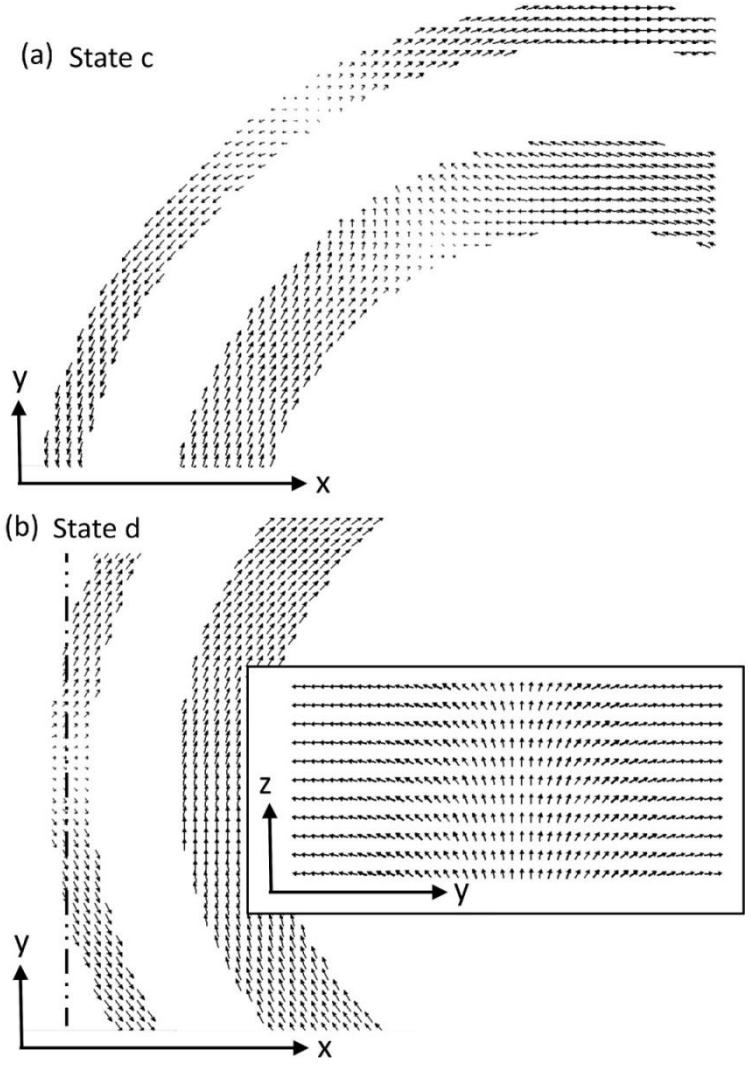

Figure 6.6 Spin configuration at domain walls of NiFe(8nm)/Au(16nm)/ NiFe(16nm) at state a3 (a) and state a4 (b) as indicated in Figure 6.3.

6.4 Magnetostatic coupling at edges

In the simulated hysteresis loop in Figure 6.3 (a), it was observed that the *V-RO* switching for the inner nanoshell of NiFe(8nm)/Au(16nm)/NiFe(16nm) had a reduced switching field as compared to switching field of a single layer nanoshell with equivalent geometry. However, the stray field in the Au layer

from the outer NiFe nanoshell was not significant when compared to this switching field, as observed in Figure 6.5(b). It raised a question on the source of promoted *V-RO* switching of the inner nanoshell.

In confined ferromagnetic nanostructures with submicron dimension, the edge plays a more important role in determining the overall magnetization configuration [19, 20]. Figure 6.7 depicts the color maps for the magnitude demagnetization and stray field in the *x-y* plane at top surface (a) and bottom surface (b) of NiFe(8nm)/Au(16nm)/NiFe(16nm) layered nanoshell just before the magnetization in the inner nanoshell was switched to Reverse Onion state. Near the opposite domain walls at top left and bottom right of the nanoshell, strong stray field of near 1000Oe in the Au spacer was present. Such field would promote the *V-RO* switching of inner NiFe nanoshell.

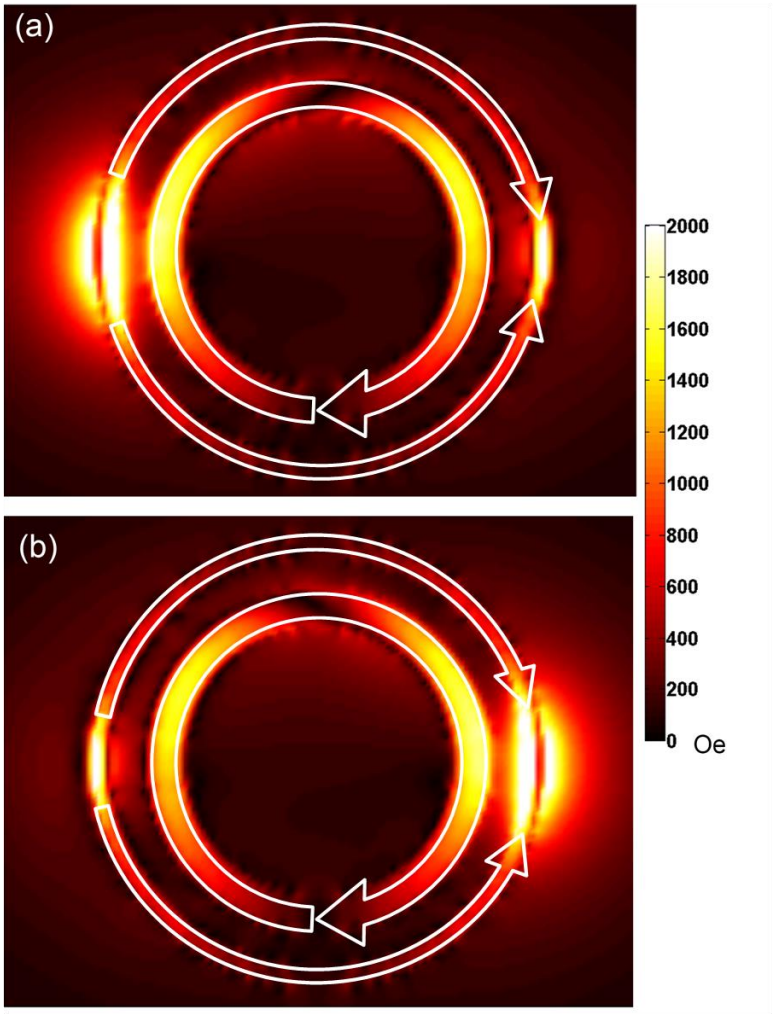

Figure 6.7 Color map of in-plane demagnetization/stray field ($(H_x{}^2 + H_y{}^2)^{1/2}$) at top surface (a) and bottom surface (b) of NiFe(8nm)/Au(16nm)/NiFe(16nm) layered nanoshell immediately before *V-RO* switching of inner Nanoshell. The white arrows depict the magnetization states.

The stray field originated from the domain walls of the outer NiFe nanoshell. Figure 6.8 depicts the magnetization vectors in the *x-y* plane view at the half of shell height and cross-sectional view in the *x-z* plane across the domain walls in the outer NiFe nanoshell corresponding to Figure 6.7. The length of the arrow is proportional to the component of magnetization in the

respective plane. It can be observed that the magnetization at domain wall cores in the outer nanoshell had a preference to be aligned along *z* axis. This explained that at half of the shell height, the stray field in Au spacer is not strong. However, at the top left and bottom right edges, the magnetization vectors had stronger in-plane component as shown in the two regions circled out in Figure 6.8 (b). This led to an increased stray field at the two spots as shown in Figure 6.7.

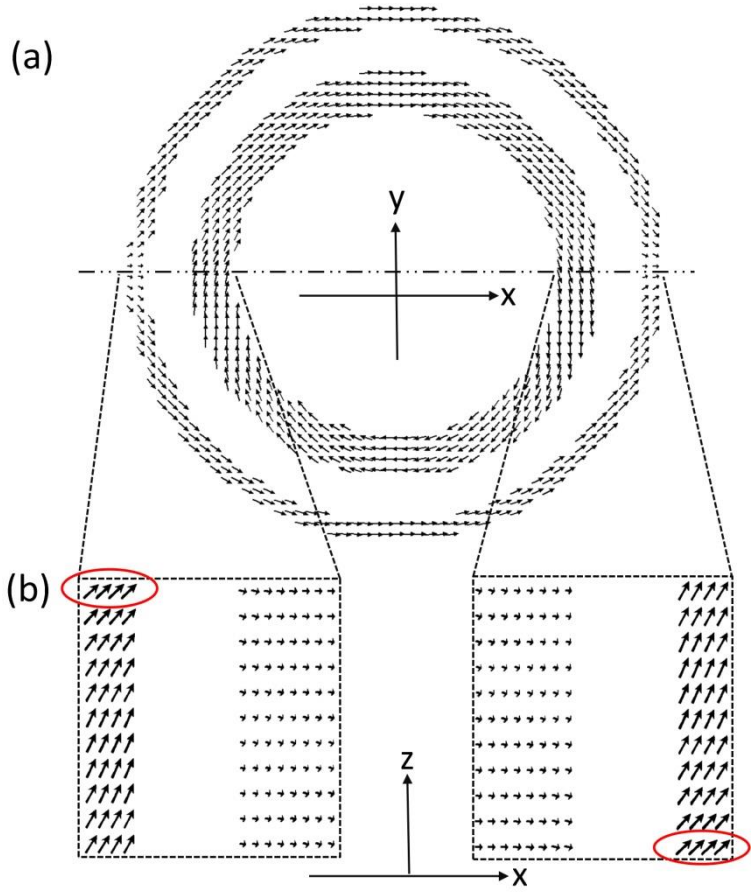

Figure 6.8 Spin configurations in NiFe(8nm)/Au(16nm)/NiFe(16nm) layered nanoshell immediately before state d-e switching. (a): x-y plane view at half of shell height; (b): magnified x-z plane view at cross-sections indicated in (a).

Such increased stray field at local edges can give rise to magnetostatic edge coupling. In reality, the layered structure may not be well defined at the edge. Defects such as reduced spacer thickness at local sites would amplify this coupling effect.

6.5 Néel coupling

As shown in the transmission electron micrograph in Chapter 3, the interfaces in the NiFe/Au/NiFe layers were subjected to roughness. Néel coupling may occur if the roughness profiles at the two interfaces were correlated [15].

OOMMF simulations with interfacial profile were carried out to investigate the Néel coupling effect. To simplify the calculation, sinusoidal interfacial roughness profile with amplitude of 2nm and an angular period of $\pi/10$ was used, as shown in Figure 6.9. Moreover, the two interfaces were assumed to have coherent roughness.

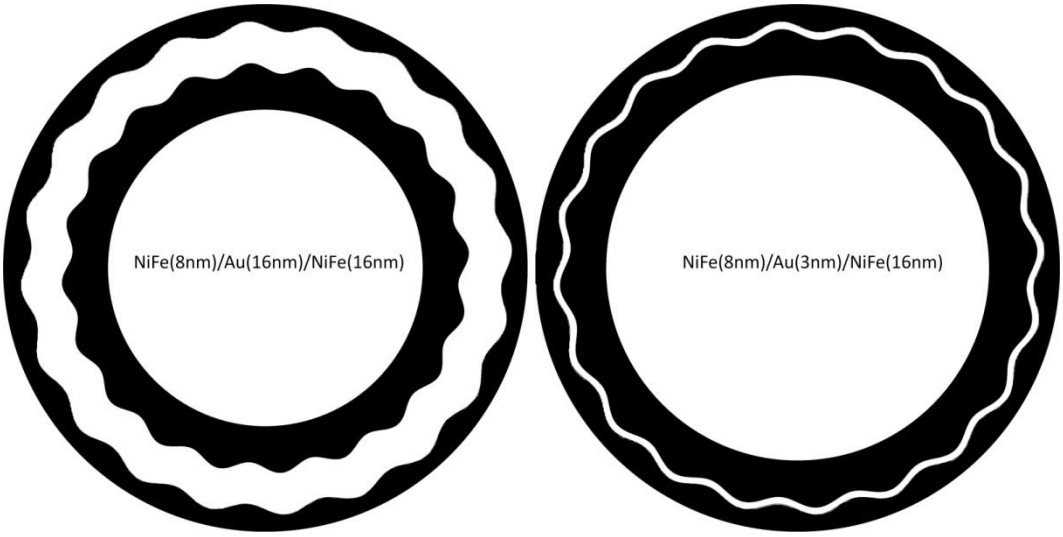

Figure 6.9 Interface profiles for simulation of Néel coupling in NiFe(8nm)/Au(16nm)/NiFe(16nm) and NiFe(8nm)/Au(3nm)/NiFe (16nm). The black color denotes NiFe; the white gap in between denotes Au spacer.

Figure 6.10 depicts the simulated hysteresis loops and magnetization reversal processes for NiFe(8nm)/Au(16nm)/NiFe(16nm) and NiFe(8nm) /Au(3nm)/NiFe(16nm) layered nanoshells with the above interfacial roughness profile. In both cases, presence of vortex state (a2 and b2) with the outer and inner NiFe nanoshells in the same chirality was observed. This parallel alignment tendency was in agreement with previous study on Néel coupling effect in thin film samples [21].

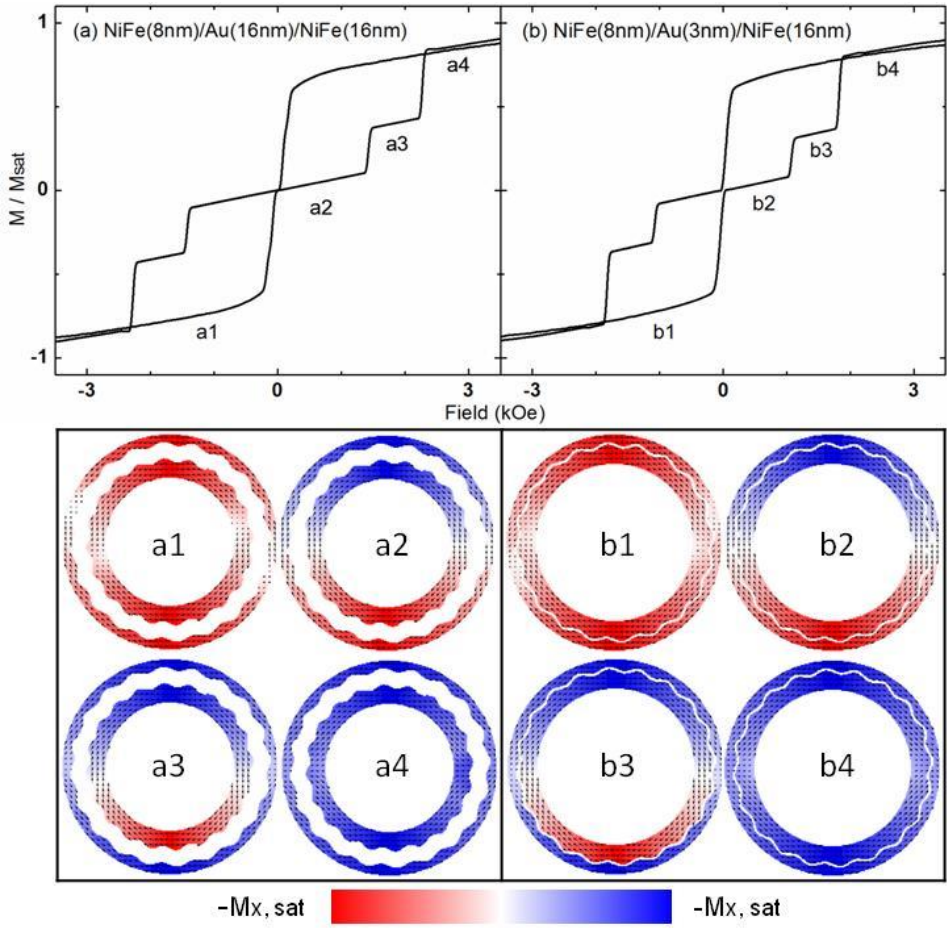

Figure 6.10 Simulated hysteresis loops and magnetization states of NiFe(8nm)/Au(16nm)/NiFe(16nm) and NiFe(8nm)/Au(3nm)/NiFe(16nm) with sinusoidal interface profiles.

Figure 6.11 depicts a magnified view of the magnetization states (a) and demagnetization/stray field (b) for layered NiFe(8nm)/Au(16nm)/ NiFe(16nm) nanoshell. Similar to layered thin film, correlated interfacial roughness led to surface poles and these poles gave rise to magnetostatic Néel coupling. With magnetization of two NiFe layers parallel with each other, there was less stray field and hence reduced demagnetization energy [19, 21].

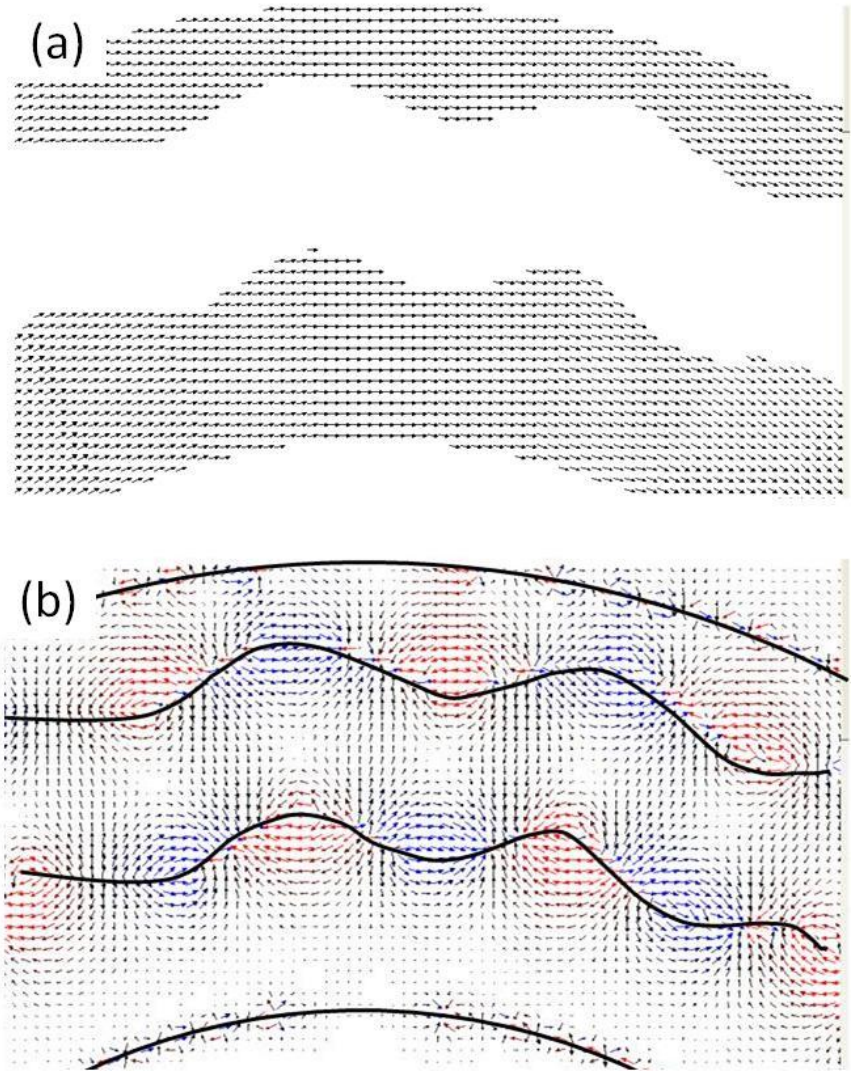

Figure 6.11 Simulated magnetization state (a) and demagnetization/stray field (b) for NiFe(8nm)/Au(16nm)/NiFe(16nm) at vortex state.

The strength of Néel coupling effect increases for a thinner spacer. This was manifested in the color maps of demagnetization field inside the NiFe layers. Figure 6.12 shows the magnitude of in-plane demagnetization and stray field when both shells were in Vortex state at remanence. With a 16nm Au spacer, there was substantial stray field in the magnitude of 1 kOe in the outer

and inner NiFe nanoshells near the interfaces with Au layer, as shown in Figure 6.12(a). However, with a 3nm Au spacer, the demagnetization field in the NiFe nanoshells decreased significantly, as shown in Figure 6.12(b).

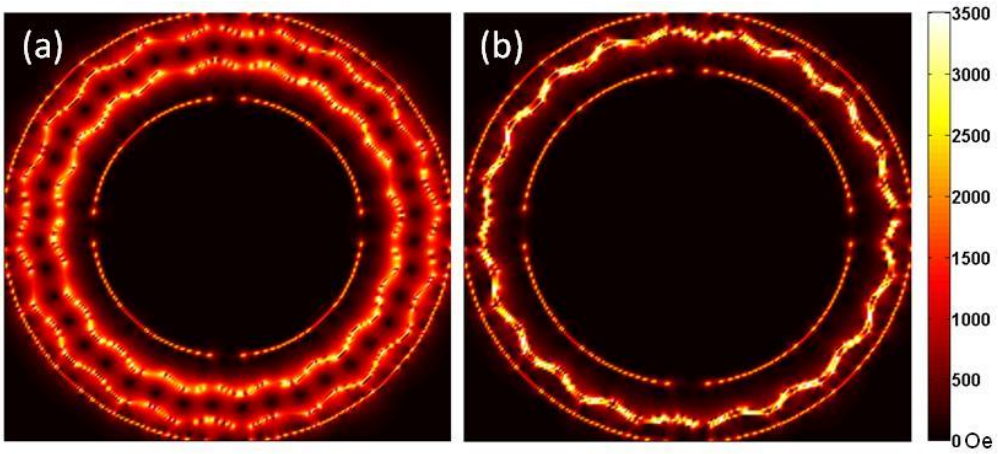

Figure 6.12 Color maps of in-plane demagnetization/stray field ($(H_x{}^2 + H_y{}^2)^{1/2}$) for layered nanoshell in remanence state at half height of the shells with an Au spacer of 16nm (a) and 3nm (b).

Figure 6.13 shows the volumetric demagnetization energy versus the applied field for NiFe(8nm)/Au(16nm)/NiFe(16nm) and NiFe(8nm)/Au(3nm)/ NiFe(16nm) layered nanoshells at remanence. When both NiFe nanoshells were in Vortex state, the contribution from domain wall to demagnetization energy was minimized. The demagnetization energy was primarily from the interfacial poles. With a 3nm Au spacer, lower volumetric demagnetization was observed. This suggested that the layered nanoshell with a 3nm Au spacer was subjected to more Néel coupling effect compared to that with a thicker Au spacer of 16nm.

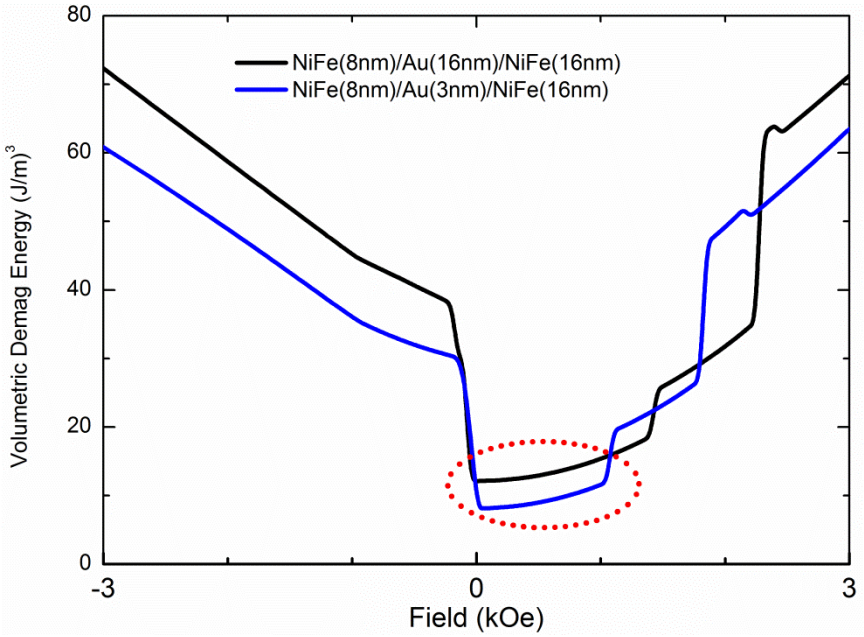

Figure 6.13 Volumetric exchange energy versus the applied field for layered nanoshell with 3nm and 16nm Au spacer.

To summarize the effect of Néel coupling, the OOMMF simulation results showed that a correlated interfacial roughness profile at the interfaces of concentric layered NiFe/Au/NiFe nanoshell had significant modification to the magnetization switching path. Dual Vortex state in the outer and inner nanoshell with the same chirality was observed for both spacer thicknesses due to the parallel alignment tendency with Néel coupling effect.

6.6 Effect of NiFe shell width

The switching field of ferromagnetic nanoshells depends greatly on the shell width, as discussed in Chapter 5. This session discusses how the shell widths of outer and inner NiFe nanoshells affect the magnetization switching of concentrically layered NiFe/Au/NiFe nanoshells.

Figure 6.14 shows the experimental and simulated hysteresis loops of NiFe(12nm)/Au(14nm)/NiFe(16nm) layered nanoshell. With an increased outer shell width of 12nm, the NiFe(12nm)/Au(14nm)/NiFe(16nm) layered nanoshell array exhibited a two-step switching process experimentally. In the simulated magnetization reversal path, the layered nanoshell starts with an overall Onion state (state a). At remanence, both shells switched to Vortex state (state b). As field increased further to 2100 Oe, the outer NiFe nanoshell switched to Reverse Onion state and the inner NiFe nanoshell remained in Vortex state (state c). This magnetization state only lasted in a field range of 150 Oe before the inner shell was switched Reverse Onion (state d).

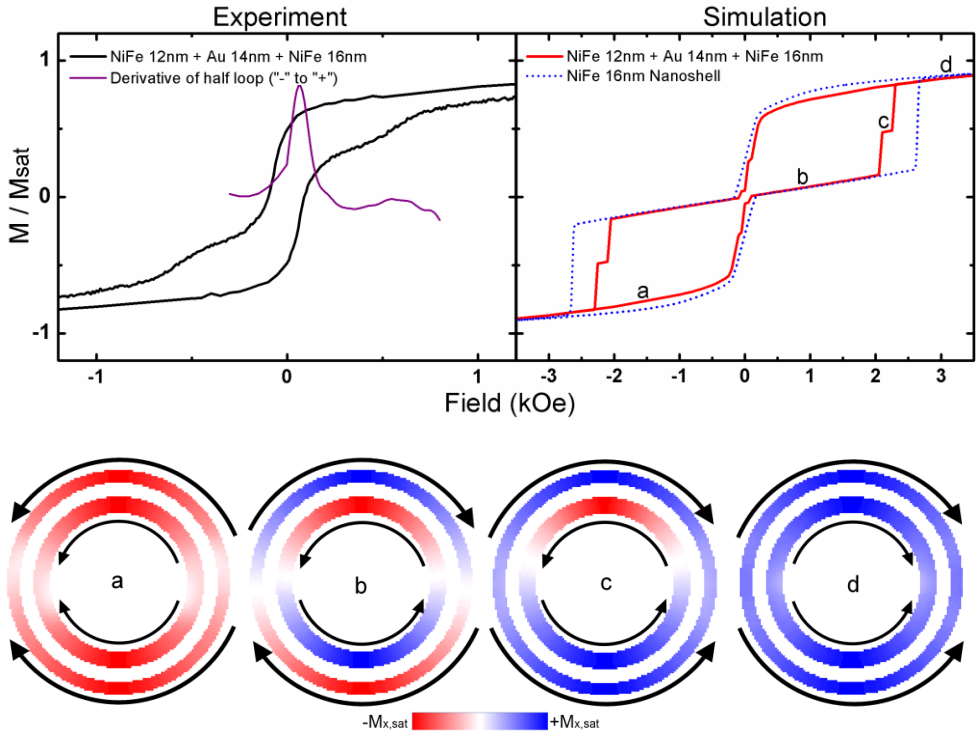

Figure 6.14 Experimental and simulated hysteresis loops and simulated spin states of NiFe(12nm)/Au(14nm)/NiFe(16nm) layered nanoshell.

The dotted blue line shows the simulated hysteresis loop of single layer NiFe nanoshell identical to the inner NiFe nanoshell. In comparison, the inner NiFe shell in layered nanoshell had a lower switching field from Vortex state to Reverse Onion state. This can be attributed to the stray field from outer NiFe nanoshell in Reverse Onion state. The stray field would assist reverse domain nucleation and growth in the inner nanoshell. Hence the inner NiFe nanoshell had lower *V-RO* switching field compared with a single nanoshell identical to its dimension.

The demagnetization and stray field along *x* axis at state c in Figure 6.14 was plotted in Figure 6.15. Within the Au spacer, stray field of around 1000 Oe along $+x$ direction was observed. This would give rise to magnetostatic coupling effect between the two NiFe nanoshells. When the outer NiFe nanoshell switched to Reverse Onion state, the magnetostatic coupling effect promoted the switching of inner NiFe nanoshell from Vortex to Reverse Onion state (Figure 6.14 c-d). Hence the overall layered nanoshell may not show a distinct three-step switching, as observed in the experiment.

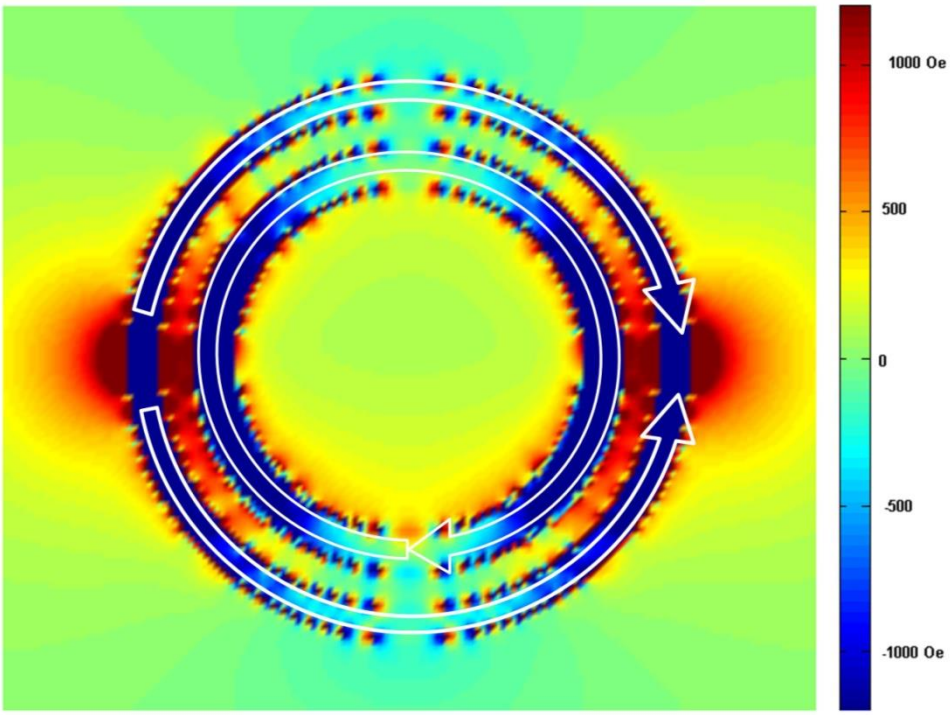

Figure 6.15 Color map of demagnetization/stray field *Hx* (component along the +*x* direction) at half of shell height around NiFe(12nm)/Au(14nm)/NiFe(16nm) layered nanoshell at state c.

Figure 6.16 shows the experimentally measured hysteresis loop of NiFe(4nm)/Au(12nm)/NiFe(18nm) layered nanoshell array. The purple line shows the first order derivative of half loop from –*x* to +*x*. The experimental hysteresis loop exhibited a two-step switching path instead of three-step switching.

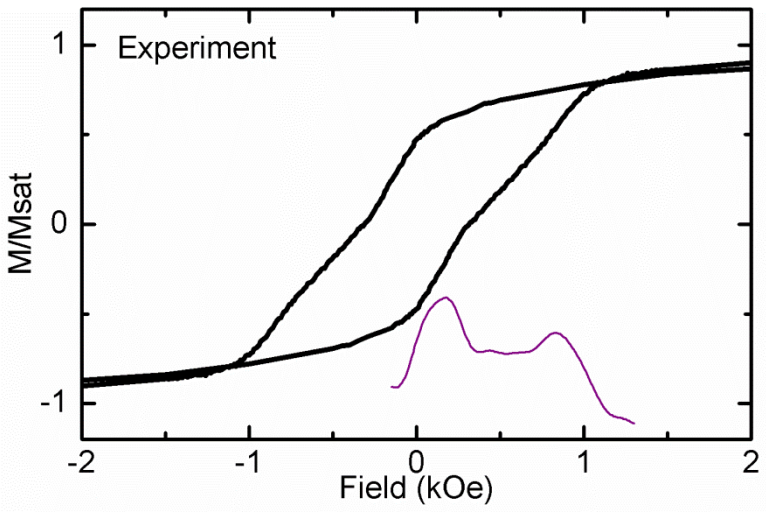

Figure 6.16 Experimental hysteresis loop of layered NiFe(4nm)/Au(12nm)/NiFe(18nm) nanoshell.

In simulated hysteresis loop as shown in Figure 6.16 a, there was an extra minor switching step. Figure 6.9(b) shows the simulated switching path. The layered nanoshell started with Onion state in both outer and inner shells (state a). When the field was switched to $+x$ direction, both outer and inner shells switched to Vortex state (state b). However, the Vortex state in 4nm outer NiFe shell was only stable over a small range of applied field. This step may not be reflected in the measured hysteresis loop. The outer shell switched to Reverse Onion state while the inner shell remained in Vortex state (state c). Finally, the inner shell was also switched to Reverse Onion state as the field increased further (state d).

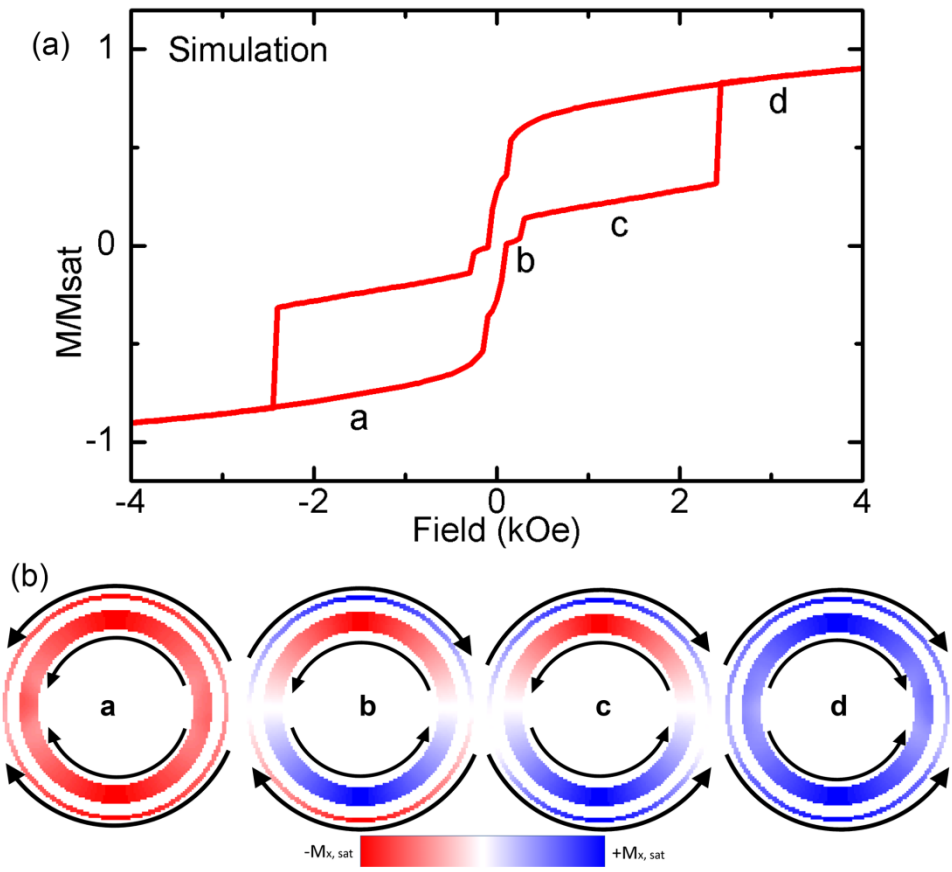

Figure 6.17 Simulated hysteresis loop (a) and magnetization reversal process (b) of NiFe(4nm)/Au(12nm)/NiFe(18nm).

In practice, the outer NiFe nanoshell with shell width of 4nm may suffer from extensive pinhole defects and may not be a continuous nanoshell due to shadowing effect in the angular deposition process. The 4nm nanoshell may be perceived as a group of nanoparticles. Hence, the NiFe(4nm)/Au(12nm)/NiFe(18nm) layered nanoshell behave magnetically as a 18nm NiFe nanoshell and a group of nanoparticles. The nanoshell gave rise to the two-step switching. The group of particles, lack of strong anisotropy, may have a linear M-H response between saturation states.

6.7 Conclusion

In summary, we demonstrated a novel NiFe/Au/NiFe concentrically layered nanoshell structure. Through experiments and micromagnetic simulations, we investigated the magnetization reversal processes of these layered nanoshell with different Au spacer thicknesses and outer/inner NiFe shell widths.

Interlayer magnetic coupling between the two NiFe nanoshells through the Au spacer played an important role in determining the overall magnetization reversal process of these layered nanoshells. With a 3nm Au spacer, pinhole induced direct exchange coupling was the dominating coupling mechanism. With a thicker Au spacer, the magnetization in inner and outer NiFe nanoshells can be exchange decoupled. However, there are other coupling mechanisms which affect the magnetization switching process. Stray field at the edge and near the domain walls can give rise to strong magnetostatic coupling effect. Néel coupling due to interfacial roughness favored parallel alignment of magnetization.

6.8 References

1. Ross, C. A., et al., *Magnetism in multilayer thin film rings.* J. Phys. D-Appl. Phys., 2008. **41**(11): p. 6.

2. Castaño, F. J., Morecroft, D., and Ross, C. A., *Low-field giant magnetoresistance in layered magnetic rings.* Phys. Rev. B, 2006. **74**(22): p. 9.

3. Huang, L., Schofield, M. A., and Zhu, Y., *Direct observation of the controlled magnetization reversal processes in Py/Al/Py asymmetric ring stacks.* Appl. Phys. Lett., 2009. **95**(4): p. 3.

4. Liu, X. M., Jain, S., and Adeyeye, A. O., *Magnetic Properties of Perpendicularly Magnetized [Co/Pd]/Au/[Co/Pd] Pseudo-Spin-Valve Nano-Ring Structures.* IEEE Trans. Magn., 2011. **47**: p. 2628.

5. Castaño, F. J., et al., *Spin-Dependent Scattering in Multilayered Magnetic Rings.* Phys. Rev. Lett., 2005. **95**(13): p. 137201.

6. Hayward, T. J., et al., *Switching behavior of individual pseudo-spin-valve ring structures.* Phys. Rev. B, 2006. **74**(13): p. 134405.

7. Mascaro, M. D., et al., *360 °domain wall mediated reversal in rhombic Co/Cu/NiFe magnetic rings.* Appl. Phys. Lett., 2011. **98**(25): p. 252506.

8. Lee, J. H., et al., *Influence of thermal excitation on magnetization states and switching routes of magnetic multilayer rings.* J. Appl. Phys., 2009. **105**(7): p. 3.

9. Jain, S. and Adeyeye, A. O., *Low temperature investigations of switching processes in multilayer rings.* J. Appl. Phys., 2009. **106**(2): p. 4.

10. Jain, S. and Adeyeye, A. O., *Aligned Alternating Head-to-Head and Tail-to-Tail Domain Walls in Ferromagnetic Concentric Rings.* IEEE Trans. Magn., 2010. **46**(6): p. 1595.

11. Parkin, S. S. P., More, N., and Roche, K. P., *Oscillations in exchange coupling and magnetoresistance in metallic superlattice structures: Co/Ru, Co/Cr, and Fe/Cr.* Phys. Rev. Lett., 1990. **64**(19): p. 2304.

12. Rijks, T. G. S. M., et al., *Interplay between exchange biasing and interlayer exchange coupling in Ni80Fe20/Cu/Ni80Fe20/Fe50Mn50 layered systems.* J. Appl. Phys., 1994. **76**(2): p. 1092.

13. Biragnet, F., et al., *Interactions between Domain Walls in Coupled Films.* Physica Status Solidi (B), 1966. **16**(2): p. 569-576.

14. Fuller, H. W. and Sullivan, D. L., *Magnetostatic Interactions between Thin Magnetic Films.* J. Appl. Phys., 1962. **33**(3): p. 1063.

15. Néel, L., Comptes. Rendus, 1962. **255**: p. 1676.

16. Miyawaki, T., et al., *Control of interlayer magnetostatic coupling in submicron-sized Fe/Au/Fe rings.* Appl. Phys. Lett., 2008. **92**(3): p. 032502.

17. Wang, Z., et al., *Synthesis and magnetic properties of large-area ferromagnetic cylindrical nanoshell and nanocup arrays.* J. Appl. Phys., 2013. **113**(21): p. 214301.

18. Leng, Q., et al., *Interlayer coupling across noble metal spacers.* J. Magn. Magn. Mater., 1993. **126**: p. 367.

19. Wang, D., et al., *Magnetostatic coupling in spin dependent tunnel junctions.* IEEE Trans. Magn., 2000. **36**(5): p. 2802.

20. Wang, S., et al., *Effect of Magnetic Tunneling Junction Sensor Size on Ferromagnetic Interlayer Coupling.* IEEE Trans. Magn., 2011. **47**(10): p. 3415.

21. Stiles, M. D., Bland, J. A. C., and Heinrich, B., *Interlayer Exchange Coupling*, in *Ultrathin Magnetic Structures III*. 2005, Springer Berlin Heidelberg. p. 99.

Chapter 7 Conclusion and Future Work

7.1 Conclusion

To conclude, we have demonstrated a large-area ordered ferromagnetic nanostructure array synthesis method based on mask-less interference lithography. This method was highly versatile on the final geometries achievable, with nanodisk, nanoparticle, and novel nanostructures including cylindrical nanoshell, perforated nanocup, nanocup and concentric layered nanoshell demonstrated. Ferromagnetic perforated nanocup, nanocup and concentric layered nanoshell have not been reported before in literature to the author's knowledge. The magnetization configurations and reversal processes related to their dimensions and geometries in these nanostructures were investigated through experiments and micromagnetic simulations.

In a ferromagnetic nanostructure array with reduced spacing comparable to its size, the stray field can be large enough to cause significant dipolar magnetostatic coupling between neighboring nanomagnets, such as in the nanodisk array structure in this thesis. Such magnetostatic coupling can lead to correlated switching of nanomagnets in the array.

The magnetization switching process of NiFe nanoshells strongly depended on their shell width. With thicker shell widths, the nanoshells exhibited Onion-Vortex-Reverse Onion magnetization reversal process similar to flat thin film rings, despite of their higher height/width ratio. With thinner

shell width of 8nm, the nanoshell exhibited direct Onion-Reverse Onion switching without going through the Vortex state. The magnetization at the core of domain walls in these nanoshells showed a preference for out-of-plane alignment with respect to the sample. This favors reduced mganetostatic cross-talk between neighbors in the array compared to the thin-film ring structure. With partially and fully covered base in perforated and imperforated nanocup structure, there were more intermediate states observed compared to the nanoshells due to their unique shape confinement.

Understanding of interlayer magnetic coupling through a non-magnetic spacer layer is important in the design of novel spintronic devices. A novel concentric layered NiFe/Au/NiFe nanostructure was investigated in this work. Various magnetization coupling mechanisms critical in determining the magnetization states and reversal processes were examined. With a spacer of 3nm, direct exchange coupling due to the presence of pinhole defects emerged as the critical coupling mechanism. With a thicker Au spacer, the inner and outer NiFe nanoshells can be exchange decoupled. Magnetostatic coupling due to stray field at domain walls and edges can be strong enough to couple the magnetizations through the Au spacer. Correlated interfacial roughness gave rise to Néel coupling effect. Parallel alignment of moments was favored. As a result, a dual Vortex state was observed during the moment reversal process in the simulation.

Despite the good versatility and dimension control demonstrated in this study, there are constraints in the synthesis method. Interference lithography is limited to patterning of period structures. This patterning method is not as

flexible as lithography and electron beam lithography, though the later methods are associated with higher cost of ownership and cost of setup. Also, the shadowing effect imposes a limitation on the angular deposition process. The shell width and height cannot be too large in order to keep a uniform sidewall width along the *z* axis. In the micromagnetic simulations, there are several assumptions made in this study, particularly in the simulation. The sidewall of nanoshell, nanocup and perforated nanocups was assumed to be straight in the simulation. Surface roughness and grain boundary effects were ignored. There were also inevitable discretization errors along the curved surfaces and interfaces. Discretization errors may lead to amplified stray field and hence demagnetization energy. In addition, to keep a smoother definition of interfaces, a 1nm cell size was used in *x-y* plane. This gave a possibility that drastic change of magnetization in confined space was allowed in the simulation.

7.2 Future work

These ferromagnetic nanostructures showed rich diversity of magnetization states with a combination of spin states in the outer and inner nanoshell including Onion, Reverse Onion, Vortex, 360 ° domain wall and Vortex chirality. Layered nanoshells of other ferromagnetic and spacer materials can also be explored. This laterally engineered layered structure can provide a new design for magnetic random access memory and spin-logic devices [1-3].

The synthesis method described here not only can be used for ferromagnetic nanostructures but also can be explored to fabricate nanoshell, nanocups and layered nanoshells of other materials for plasmonics, photonics and optoelectronics studies, and applications such as surface plasmon resonance based biosensors and nanoscale optical sensors [4, 5].

7.3 References

1. Zutic, I. and Fuhrer, M., *Spintronics: A path to spin logic.* Nat. Phys., 2005. **1**(2): p. 85.
2. Zhu, J. G., Zheng, Y., and Prinz, G. A., *Ultrahigh density vertical magnetoresistive random access memory (invited).* J. Appl. Phys., 2000. **87**(9): p. 6668.
3. Wei, H.-X., et al., *Effects of current on nanoscale ring-shaped magnetic tunnel junctions.* Phys. Rev. B, 2008. **77**(13): p. 134432.
4. Larsson, E. M., et al., *Sensing Characteristics of NIR Localized Surface Plasmon Resonances in Gold Nanorings for Application as Ultrasensitive Biosensors.* Nano Lett., 2007. **7**(5): p. 1256.
5. Zheng, Y. B., et al., *Fabrication of large area ordered metal nanoring arrays for nanoscale optical sensors.* J. Non-Cryst. Solids, 2006. **352**: p. 2532.